INVESTIGATION OF GRANULAR DYNAMICS AND PARTICLE MIXING IN GAS-SOLID TWO PHASE FLUIDIZED BEDS

By

Runjia Liu

A THESIS SUBMITTED FOR THE DEGREE

OF

DOCTOR OF PHILOSOPHY

IN THE LABORATORY FOR SIMULATION AND MODELLINGOF PARTICULATE SYSTEMS, DEPARTMENT OF CHEMICALENGINEERING, MONASH UNIVERSITY, CLAYTON, VIC 3800,AUSTRALIA

August 2019

This page is intentionally left blank

Contents

ABSTRACT

Fluidized beds are widely used in industries as they can offer high quality contacts between particles. Particle behavior such as particle mixing is very important for the understanding of fluidization and the design of fluidized beds. The aim of this project is to investigate the regularity of particle velocity distribution and particle mixing in fluidized beds by using both experimental and computational methods. To achieve the research aim, four key chapters have been proposed and the key findings are summarized below.

Bubbles play an important role in particle mixing in fluidized beds. However, fundamental understanding of particle velocity distribution around bubbles is still limited. Therefore, both particle image velocimetry (PIV) technique and discrete element modelling (DEM) are employed in Chapter 3 to investigate the particle velocity fields in fluidized beds. Results show that particle velocity distribution for a single bubble can be described by tri-peak model which is a linear superposition of three Maxwellian distributions. A tri-peak model based on the fluid and particle control mechanism is also theoretically derived, showing that the tri-peak model can profile particle velocity distribution more accurately than other models.

Mixing of granular materials in jetting fluidized beds is further investigated in Chapter 4. The mixing efficiency is affected significantly by the number of jets and their locations. In the study, discrete particle model is validated by physical experiments, and cases with different jet numbers (varying from one to five) but the same gas flow rates are compared. It is found that the mixing efficiency in the one-jet case (spouted-bed) is 1.5~3 times higher than other cases due to a higher jet velocity and umbrella-type flow pattern. For the multiple jets, bubbles and vortex can form and promote particle mixing but not as efficient as the case of one jet.

Further understanding the particle mixing and segregation dynamics is essential in successfully designing and reasonably operating multicomponent fluidized bed. In Chapter 5, a novel fluorescent tracer technique combining image processing method is used to investigate the mixing and segregation behavior in a binary fluidized bed with wide size distributions. The results show that the theoretical minimum fluidization velocity calculated from the bed pressure drop cannot represent the whole fluidization for a wide particle size distribution system. It is also found that there is a stagnant region in the bottom of the bed that consists of particles with large sizes and a low degree of sphericity. Particles in the stagnant region are difficult to fluidize and should be considered in the design of fluidized beds in industrial applications.

Particle rotation has been found important in affecting the heterogeneous structures of fluidized beds, for example, Magnus lift force might play a pivotal role when particles have fast rotation speed. In Chapter 6, a pseudo two-dimensional DEM is used to investigate the influence of Magnus lift force in fluidized bed, and the rotational Reynolds number (Re_r) bases on the angular velocity and the diameter of the spheres is used to characterize the rotational movement of particles. Results show that the influence of Magnus lift force is enhanced with a higher Re_r. Magnus lift force affects the movement of particles in both radial and axial directions when Re_r is high. However, in low Re_r case it can be neglected. This indicates that Magnus effect should be considered in gas-solid two phase systems when the particle rotational speed is high.

This page is intentionally left blank

ACKNOWLEDGEMENTS

My thesis was completed under the joint support of Monash University and Southeast University. Many people have offered me valuable help in my thesis writing, including my supervisor, my classmates and my parents.

First and foremost, I would like to show my deepest gratitude to my supervisor, Professor Aibing Yu, a respectable, responsible and resourceful scholar, who has provided me with valuable guidance for my PhD project. I still remember the day when I first came to his office and discussed about my PhD project. Before that day I had a bottleneck in my PhD project and did not know how to do it. “Well, Liu,” Prof. Yu said, “Your trouble is that you always build a very complicated theoretical or experimental system first, and then think about how to use them. You need to make your research aim clear first and then think about how to solve the problem. Theoretical and experimental system you use should be served for your research aim, but you are putting them in the wrong order.” His words are very important and valuable for me so I still remember the details. After that day, my first scientific paper for SCI Journals was published soon. I also would like to thank my co-supervisor Professor Rui Xiao, for the support and guidance to establish this research project. My PhD journey could not been successful without his help.

My special gratitude goes to Dr. Zongyan Zhou. I am very grateful for his patience in revising my work and continued support. His serious scientific attitude and rigorous scholarship enlightens me not only in this thesis but also in my future study. Sincere gratitude goes to Dr. Ruiping Zou for her continued support and encouragement for every step of my project.

I also acknowledge my colleagues in Monash University, Lingling Liu, Guanwen Zhou, Fei Xiao, Erlei Li, Lin Wang, Siyuan He, Vita, Mengmeng Zhou, Wenchan Gao, LuLu Jiao, Katie and Allen. They are more than colleagues but friends and thanks for their help in both academic research and life. I would also like to extend my gratitude to all staffs in the Department of Chemical Engineering who helped me for my safety training and enrollment. Without their help, I would not be able to finish my project on time.

Finally, I would like to thank my family for their considerations and encouragement all through these years. My parents have always been supporting me without a word of complaint, and I am forever grateful for what they have done for me.

COPYRIGHT NOTICE

This page is intentionally left blank

DECLARATION

This thesis contains no material which has been accepted for the award of any other degree or diploma at any university or equivalent institution and that, to the best of my knowledge and belief, this thesis contains no material previously published or written by another person, except where due reference is made in the text of the thesis.

Signature:

Print Name: Runjia Liu

Date: August 2019

This page is intentionally left blank

LIST OF FIGURES

LIST OF TABLES

This page is intentionally left blank

CHAPTER 1 INTRODUCTION

The development of gas-solid fluidized bed technology stems from the pursuit of enhancing the efficiency when processing solid particulate materials. This so-called "fluidization" is different from the traditional gas, solid and liquid states. It is a new state that is generated from the interaction of fluid and solid particles. The fluidized bed is a reactor in which particles are processed by the fluidization method. The gas-solid fluidized bed uses gas as a power source to fluidize the particles. Compared with a traditional fixed bed and moving bed, the gas-solid fluidized bed not only enhances the interaction between the gas and solid particles but also promotes the heat and mass transfer efficiencies. On one hand, the rates of the physical and chemical processes are greatly increased. On the other hand, the temperature and concentration distributions throughout the reactor are made uniform. Gas-solid fluidized beds have such characteristics as a high production efficiency, a good expansion performance, and a good scale-up performance. Because of these remarkable advantages, after nearly 70 years of fundamental theoretical research and technological development, the gas-solid fluidized bed is widely used in many industries, including the chemical, energy, food processing, environmental protection, and materials industries.

In the theoretical studies of a gas-solid fluidized bed, the research scope can be roughly grouped into three scales: the microscopic particle scale, the mesoscopic structure scale, and the macroscopic reactor scale.

A particle group is composed of single particles. The force and motion of microscopic single particles are the basis for studying the motion of mesoscopic particle groups and the mass/heat transfer phenomena of macroscopic reactors. In a typical gas-solid two-phase system, the force analysis is relatively complicated because the particles are subjected to the effects of both the fluid and other particles. Specifically, the particles are subjected to a drag force, buoyancy force, gravity, contact forces (collisions and friction) between particles and between the particles and the walls, and pressure gradient forces. In some special circumstances, additional force terms also apply. For example, the Saffman lift force is generated in a flow field with a velocity gradient, and the Magnus lift force is produced by the rotation of particles. An in-depth study of the forces on particles and the conditions for force generation is of great significance for investigating particle motion, developing numerical simulation methods, and optimizing the reactor’s structural parameters. However, some forces are often overlooked in numerical simulation calculations. The Magnus lift force is one such example. On one hand, it is difficult to experimentally observe the rotation of the particles, on the other hand, it is difficult to obtain a theoretical relationship that is applicable to actual gas-solid two-phase systems (Zhou and Fan 2015a). Therefore, systematic research is still lacking.

The so-called mesoscopic structure scale, i.e., the mesoscale (Li et al. 2005), refers to the scale between the microscopic particle scale and the macroscopic reactor scale.

The main research objects at this scale are mesoscale structures in the gas-solid fluidized beds, such as bubbles and particle clusters. Unlike a single uniform fluid, the fluidized particle flow has a certain degree of non-uniformity, which is represented by bubbles (a dense fluidized bed) and particle clusters (a dilute-phase fluidized bed). These structures have significant impacts on the segregation and mixing characteristics of the particles, the residence time distribution of the particles, and the reactor's structural design. The motions and formation mechanisms of the bubbles and particle clusters are complex. Although researchers have conducted numerous related studies, more experimental and theoretical support is needed for some specific research subjects, such as the velocity distribution curves of particles around a bubble.

At the macroscopic reactor scale, the transport phenomenon in a fluidized bed is a prominent research topic in the study of fluidized bed reactors. The research scope includes multiple aspects, such as particle mixing, particle elutriation, diffusion, gas mixing, mass transfer, and heat transfer. Particle mixing refers to mixing different particle components. In a gas-solid fluidized bed, the mixing quality greatly affects the production efficiency and product quality. On one hand, good mixing helps in achieving a relatively uniform temperature and concentration fields and avoids the formation of local "dead zones", on the other hand, good mixing promotes the contact of solid reactants in the bed and improves the reaction efficiency. Therefore, research on particle mixing in a gas-solid fluidized bed is of great significance for improving the safety and economics of the equipment. After years of theoretical development and experimental exploration, a relatively mature theoretical system has been formed for particle mixing in gas-solid fluidized beds. However, there is still a lack of experimental or simulation support for some specific practical problems, such as the effect of the nozzle arrangement on particle mixing under the same gas flow rate and the effect of particles with a wide size distribution on particle mixing.

The main aims of this study are as follows: (1) Simulate the particle rotation in the fluidized bed by adopting improved CFD-DEM calculation model, reveal the affect of Magnus effect on particle movement in gas-solid fluidized bed, and propose the application conditions of Magnus lift force. (2) Measure particle flow field in a two-dimensional fluidized bed to obtain particle velocity distribution function around a single bubble. Establish theoretical model of particle velocity distribution to describe the dynamic mechanism of particles around bubbles. (3) Put forward a novel fluorescent tracer technique combining image processing method for measuring the distribution of tracer particles in dense area of fluidized bed, and study the mixing of particles in the dense area at low gas velocity.

This page is intentionally left blank

CHAPTER 2 LITERATURE REVIEW

2.1 Current research status

During the nearly 70 years of development, researchers have conducted a series of studies on gas-solid fluidized bed technology and published many meaningful works. The research objects include microscopic particles, mesoscopic structures (bubbles, particle clusters), and macroscopic fluidized bed reactors. For topics related to this study (such as flow dynamics and particle mixing characteristics), the previous research can be mainly divided into three aspects: experimental research, numerical simulations, and theoretical research. In terms of the above three aspects, the research status of particle dynamic characteristics and mixing characteristics in a gas-solid fluidized bed are described in detail below.

2.1.1 Experimental research

2.1.1.1 Particle velocity measurement

To characterize the dynamics of the particle flow, it is often necessary to capture the motion and measure the velocity profile of the particles. Particles in a gas-solid system are characterized by their small size, large quantity, and vigorous motion. Therefore, measuring particle velocity has always been a difficulty in the research of gas-solid fluidized beds. The mainstream velocity measurement methods currently include the optical fibre method, the laser Doppler anemometry (LDA) velocity measurement method, the particle tracking velocimetry method, and the particle image velocimetry (PIV) method.

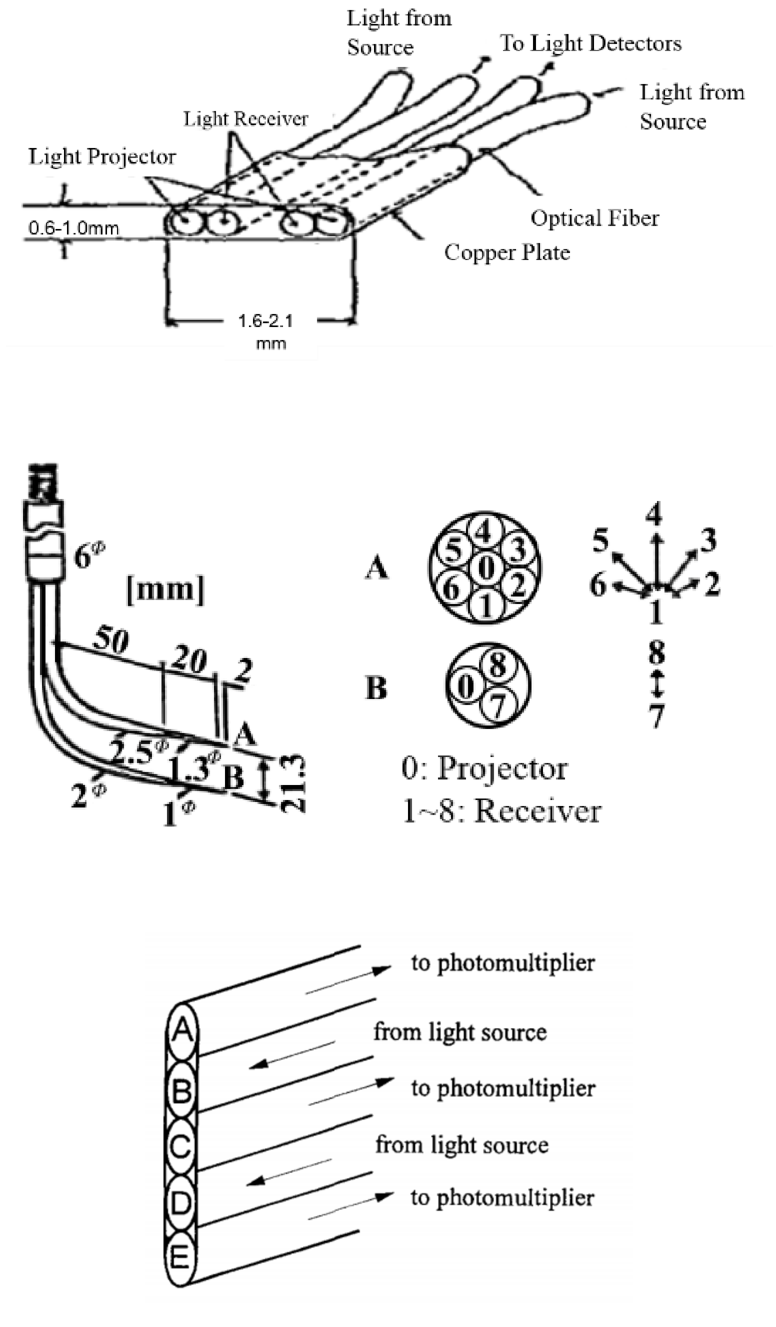

Figure 2.1. Fibre optical probes. (a)Oki et al.(1977) , (b) Ishida et al.(1980) , and (c) Zhou et al.(1995) .

Oki et al. (1977) were the first to use optical fibres as probes for particle velocity measurements. The reflected signal delay time of the particles passing through two sets of optical fibres was used as the measurement parameter. Ishida et al. (1980) improved the fibre optic probe and proposed a coaxial fibre optic probe structure. In addition to measuring the particle velocity, the probe was also able to detect the direction of particle motion based on the combination of signals from different fibres. Zhou et al. (1995) developed a five-fibre optical particle velocity probe. This probe can determine whether the light reflected to the transmitting fibres is from the same particle by obtaining two delay times. If the difference between the two measured velocities is less than 0.015, it can be determined that the two velocities were generated by the same particle in this direction. This method greatly improves the measurement accuracy. Moreover, this method can accurately measure the particle velocity in regions adjacent to the wall where the particle concentration is high and the particle movement direction is disordered. Some recent studies have shown that the optical fibre method is generally accurate for measuring solid concentration and voids, but there are many interference factors for measuring the velocity of particles. The accuracy and reliability of this method are thus still being questioned: first, the reflection-type optical fibre has the problem of light scattering, which leads to deviation in the velocity measurement, second, the instantaneous velocity of the particle group is obtained based on the cross-correlation algorithm, while the time-average velocity is obtained by a statistical average. The particle aggregation state, the particle position, and the flow field turbulence can all affect the characteristics of the optical signals. Different signal processing methods and algorithms can lead to significant differences in the results. There is currently no unified signal processing method.

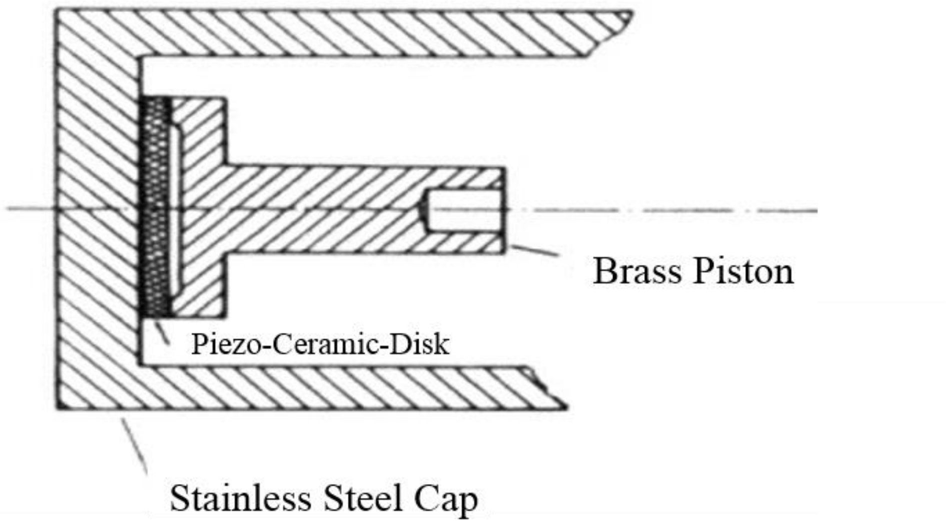

Figure 2.2. Detailed cross-section view of an ultrasound Doppler probe (Brӧring et al., 1991)

When a laser beam is irradiated onto a solid particle, the laser is scattered by the moving particle, and a frequency shift occurs between the incident light and the scattered light. This phenomenon is called the Doppler effect. The frequency shift is proportional to the velocity of the solid particle. Therefore, the Doppler shift can be used as a measure of the particle velocity. LDA velocity measurement technology can measure the instantaneous velocity of the local motion. It has the advantages of a high measurement accuracy, high temporal and spatial resolutions, a small measurement volume, a fast response frequency, non-contact measurement, and no interference on the fluid field (Boyer et al., 2003). The test principle is to use the laser Doppler effect for velocity measurement. The research mainly focuses on gas-solid two-phase systems with low solid content, liquid-solid two-phase systems, and gas-liquid two-phase systems with low liquid content (with liquid droplets dispersed in the gas phase). There have been many studies in recent years on the phase velocity measurement for gas-liquid bubble column systems, but few for three-phase flow systems (Ming et al., 2005). However, the laser (phase) Doppler velocimetry system is complicated, expensive, and has a high technical requirement. Although it has good application prospects in velocity tests for fluidized beds with fine particles and a low concentration, it has some issues, such as light blocking(Ming et al., 2005). Therefore, this technique is difficult to extensively apply in industrial production.

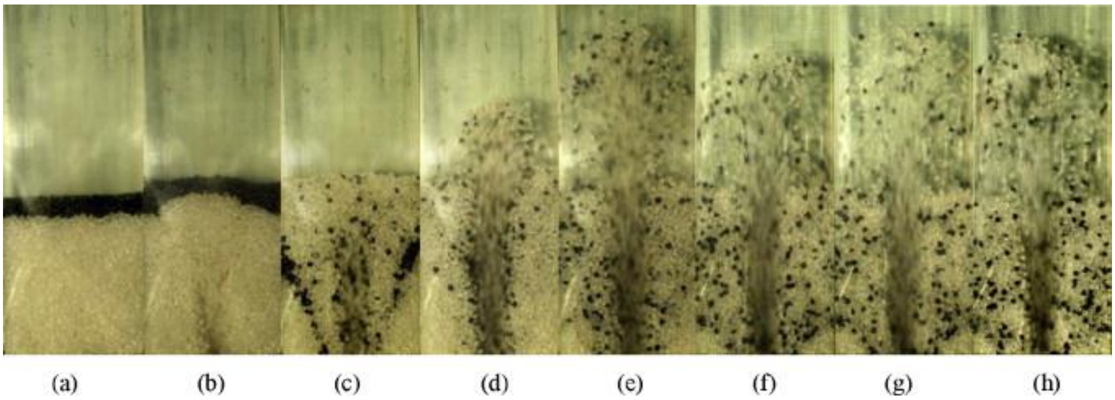

Figure 2.3. Instantaneous snapshots of particle mixing process with time by using tracer particle method (Zhang et al., 2009a).

The tracer particle method is often used to study the velocity and mixing properties of particles, the residence time distribution, and the trajectory of particle motion in a fluidized bed. The tracer particles must have hydrodynamic properties that are similar to those of other particles in the measured flow field. Currently, radioactive isotopes are mostly used as tracers. However, because of many concerns regarding radioactive isotopes in tracer preparation and safety protection, there are many difficulties and limitations in their application. Therefore, some researchers have studied the trajectory of particle motion in a fluidized bed by using the fluorescent particle tracking method. For example, Qu and Kwauk (1985) used optical fibre-excited fluorescent particles to study the trajectories of particles as they flew out of small holes in a two-dimensional bed. Kojima et al. (1989) produced tracer particles by immersing FCC in a fluorescent material. Ultraviolet light was then transmitted into the bed, and the fluorescence signal from the tracer particles was detected by fibre optic probes. Other tracer particle methods, such as hot particle tracking, phosphorescent particle tracking, salt particle tracking, and magnetic particle tracking are rarely used for particle velocity measurements. Studies on tracer particle methods can be found in the literature (for exmaple, Kwauk and Li, 2007).

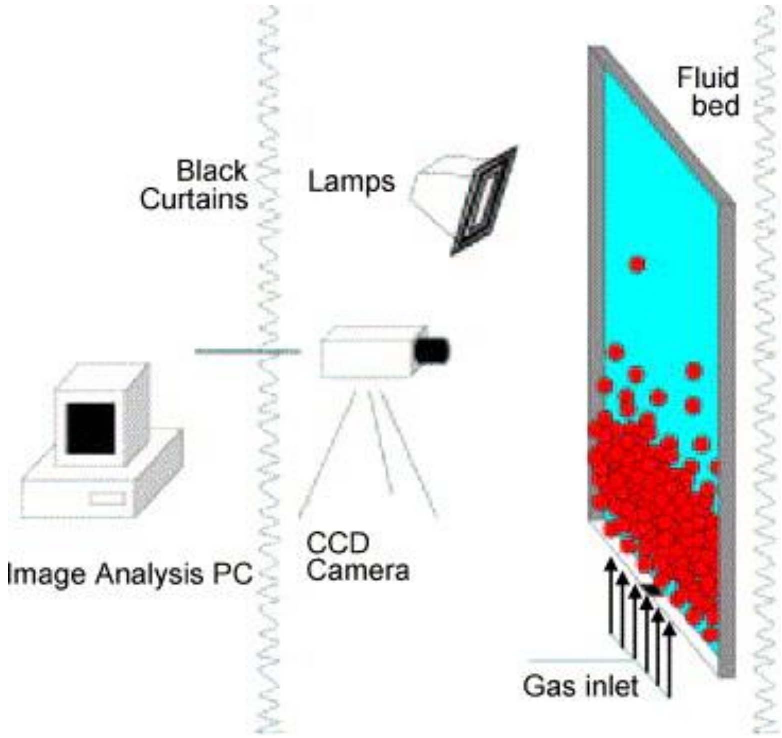

Figure 2.4. PIV experimental system (Bokkers et al., 2004)

PIV technology(Westerweel, 1997) is a two-dimensional measurement technique based on the cross-correlation analysis of particle flow field images. It uses a high-speed camera to capture two sequential frames and then performs the cross-correlation analysis using a fast Fourier transform (FFT) to obtain the particle velocity (Willert et al., 1991). The analysis process is shown in Figure 2.7. First, two sequential frames of the images are taken for analysis. Two sampled regions f(m, n) and g(m, n) of the same size are taken at the same location in each image. Then FFT is performed on the image information of f and g to obtain their expressions F(m,n) and G(m,n) in the spatial frequency domain. The cross-correlation function Φ is then calculated in the spatial frequency domain. Next, an inverse Fourier transform is performed on Φ to obtain the cross-correlation function φ. The peak value of the cross-correlation function is determined so that the particle displacements dx and dy can be determined. Finally, the particle velocity is obtained by dividing the particle displacement by the time interval between the two frames.

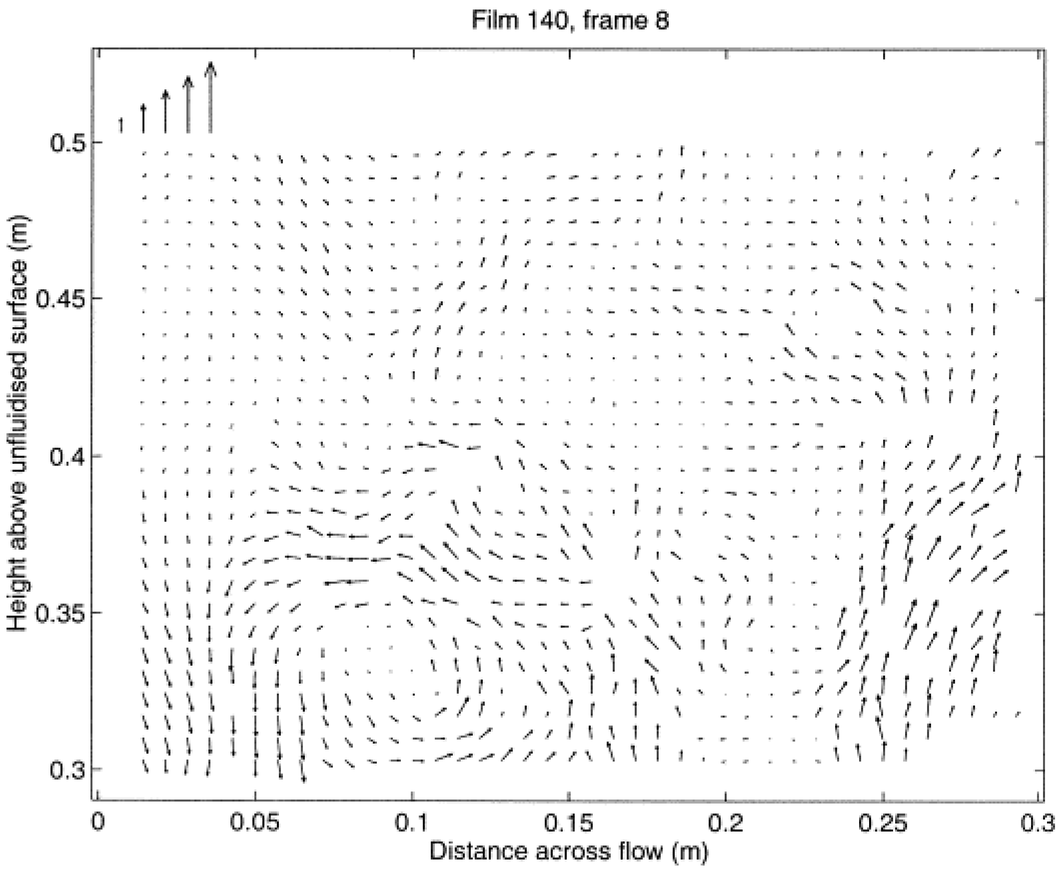

Figure 2.5. PIV vector map for flow about 0.4 m above unfluidised bed surface(Duursma et al., 2001)

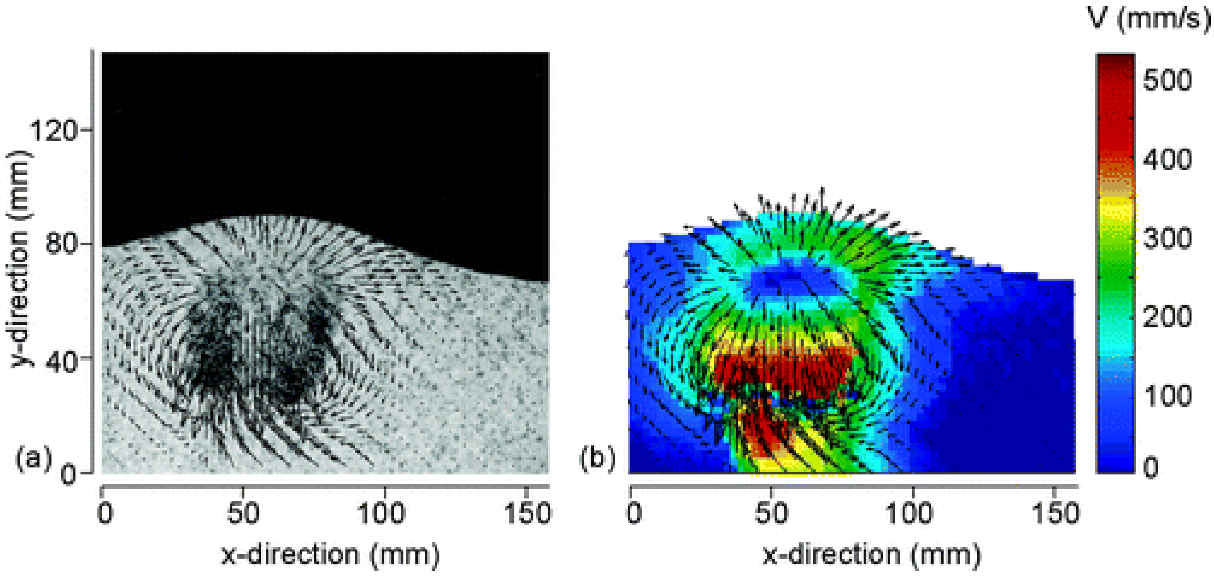

Figure 2.6. Bubble approaching the top of a 2D gas-fluidized bed by using PIV technology (Muller et al., 2007)

The development of PIV technology offers a wide range of possibilities for studying particle motion in a fluidized bed. Duursma et al. (2001) used PIV technology to explore the velocity field of particles in the freeboard region on different cross-sections of a fluidized bed. Bokkers et al. (2004) obtained the particle velocity field in the vicinity of bubbles in dense gas-solid fluidized systems using PIV. Link et al. (2010) used PIV to explore the motion characteristics of particles in spout-fluid beds. They compared the data measured by PIV with that obtained by the discrete particle model (DPM) simulation and successfully obtained the particle flow temperature in the fluidized bed. Dijkhuizen et al. (2010) extended the PIV cross-correlation algorithm and found that direct illumination was better than indirect illumination. Muller et al. (2007) analysed the motion of particles during a bubble eruption in a two-dimensional fluidized bed using PIV.

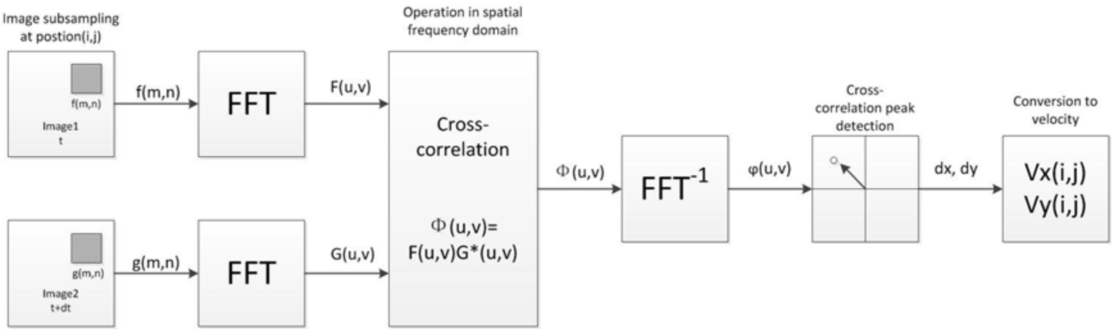

Figure 2.7. Cross-correlation calculation procedure for the analysis of PIV experiment data.

2.1.1.2 Particle mixing experiment

Figure 2.8. Photograph showing a layered packed bed of pharmaceutical granulate in the beaker on the left and, on the right, a sample from that bed collected with the core sampling probe (Wormsbecker et al., 2005)

The experimental method of particle mixing in gas-solid fluidized beds is mainly the tracer particle method. The processing method for tracer particles can be roughly divided into two categories: the sampling method and the image analysis method.

The tracer particle method is a relatively traditional method for particle mixing research: in a gas-solid two-phase fluidized bed system, some particles are marked in a certain way and can thereby be tracked by a certain method. The mixing state of particles can be visualized since the tracer particles (tracer) can well reflect the particle motion behaviour and the particle distribution in the fluidized bed. This method has been widely used in mixing studies of gas-solid fluidized beds because of its intuitiveness and convenience. Meanwhile, many tracer techniques have been developed, such as coloured particle tracking (Zhang et al., 2009a, Wormsbecker et al., 2005), salt particle tracking (Van Zoonen, 1962) , magnetic particle tracking (Avidan et al.,1985), radioactive particle tracking (Ambler et al., 1990, Helmrich et al., 1986), phosphorescent particle tracking (Fei et al., 1994), and hot particle tracking (Zhang et al., 2013).

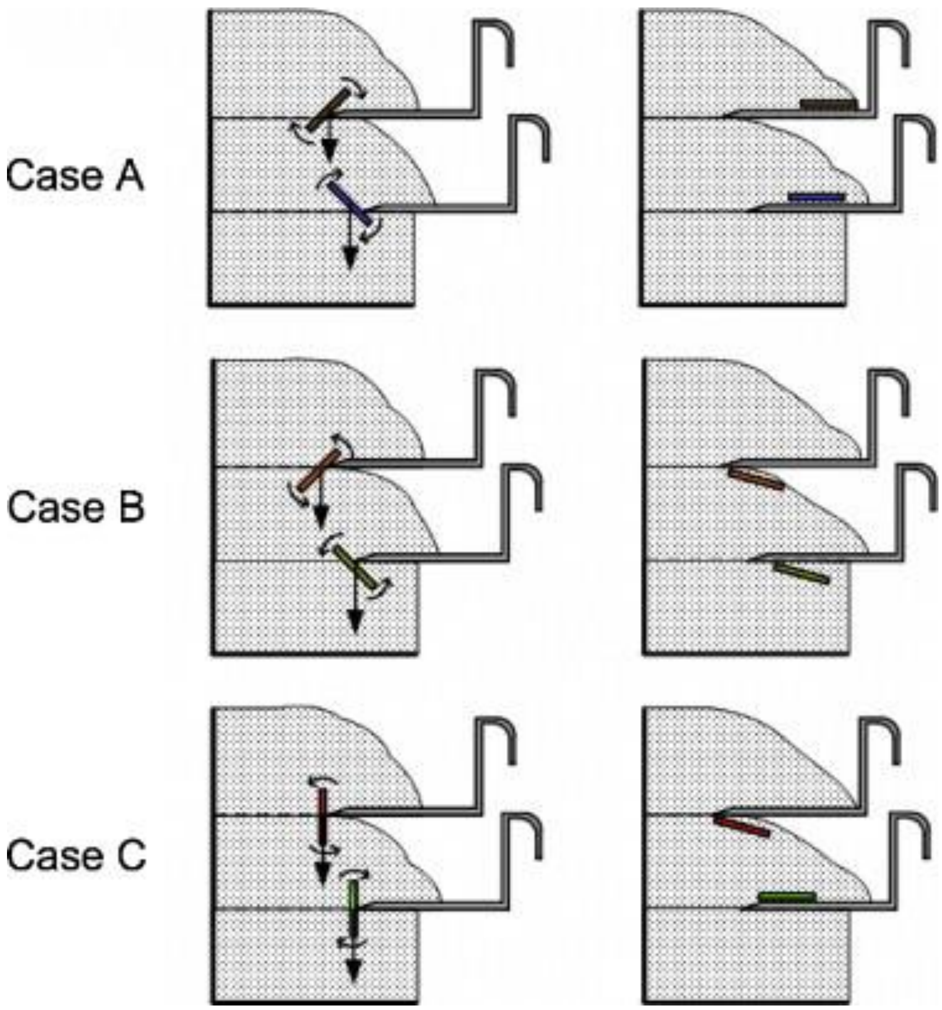

Figure 2.9. Schematic diagram of sampling. This figure shows how to determine the location of biomass particle which is located at the intersection between two layers.(Zhang et al., 2009b)

A sampling analysis is a relatively common method for particle tracking. Early studies mostly used the bed-frozen method. In this method, the fluidizing air supply is suddenly cut off to cause the bed to collapse naturally. Then the particles in the collapsed bed are sampled and analysed. Related research can be found in references (Olivieri et al., 2004). However, the particle cluster may reorganize during the free fall, which will impact the accuracy of the concentration measurement (Zhang, 2010).

Zhong et al. (2007) of Southeast University investigated the particle mixing behaviour of a large spout-fluid bed and developed the insert/separator sampling technique. A large number of studies have been conducted on particle mixing and the bed pressure drop in spout-fluid beds (Zhang et al. 2009, Zhang et al., 2009a, 2009b).

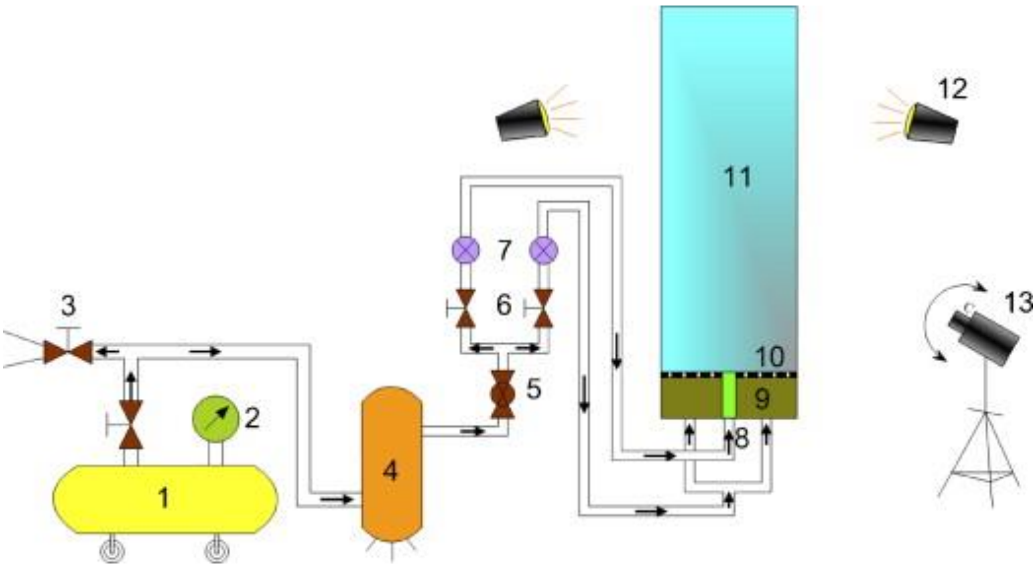

Figure 2.10. Schematic diagram of experimental system: (1) compressor, (2) pressure gauge, (3) bypass value, (4) desiccator, (5) ball value, (6) control value, (7) flow meter, (8) spout nozzle, (9) fluidizing gas chamber, (10) gas distributor, (11) spout–fluid bed, (12) halogen lamp, (13) digital CCD.(Zhang et al., 2009a)

The image analysis method uses an apparatus, such as a high-speed camera or infrared thermal imaging system, to take images/videos of particles and then analyses them. Amiri et al. (2016) of the Iran University of Science and Technology used a CMOS high-speed camera to study the particle mixing behaviour in a quasi-two-dimensional bubbling fluidized bed. The DPM simulation model was experimentally validated. Based on the principle that microwaves can heat up polar particles, Zhang et al. (2013)

of Southeast University developed a novel microwave heating-infrared thermal imaging technology. In this work, a number of polar particles were used as tracer particles and were heated to a certain temperature via microwaves. The segregation characteristics of the particles in a multi-component fluidized bed were studied by infrared thermal imaging technology.

2.1.2 Numerical simulation

With the rapid development of computer technology, the application of numerical simulations in the research of multiphase flow has attracted increasing attention. Based on the dynamic heterogeneous characteristics of a fluidized system, two mathematical models have been established, depending on how the particles phase is processed: the two-fluid model and the particle trajectory model. The two-fluid model considers the particle phase as a pseudo-fluid that interpenetrates with the real fluid. The particle phase is considered to be a fluid-like continuous phase. It is assumed in the calculation that each phase has its own velocity, temperature, and volume fraction, and each particle phase has continuous spatial distributions of velocity, temperature, and volume fraction. The particle trajectory model is also called the discrete particle model. It treats the particle phase as a discrete phase and establishes the equation of motion for single particles. The gas phase is solved by the Navier-Stokes equation. Between these two phases, one can use either one-way coupling or two-way coupling. The former only considers the effect of the fluid phase on the particles, while the latter also considers the effect of particles on the fluid. Both methods have advantages and disadvantages when solving practical problems. In addition, the two-fluid model considers the interaction between particles through the particle pressure and viscosity, and thus can solve the dense gas-solid flow with high concentration. The disadvantages of the two-fluid model are also obvious. For example, it is difficult to analyse the heterogeneous flow structure of the two-phase flow and determine the constitutive equation of a closed model, and it is impossible to obtain the trajectory of the particles. The most prominent advantage of the particle trajectory model is that the particle phase can be solved by the Lagrangian method. The motion of a single particle can be directly obtained and the empirical correlation function that is necessary for the closed solid phase stress term in the two-fluid model is not required. It is thus easy to simulate the processes with evaporation, volatilization, and reaction, and there is no numerical diffusion in the particle phase prediction. However, the biggest disadvantage of this model is that the calculation time increases exponentially with an increase in the particle number. For a gas-solid two-phase system, the improvement of the numerical simulation models and their applications in different fluidization conditions can be found in the literature(Zhou and Fan 2015b, Mikhailov and Freire 2013, Ye et al., 2004, 2005b, 2005a, Ye, 2005, Goldschmidt et al., 2004, Bokkers et al., 2004, Yuan et al., 2001, Lukerchenko, 2001, Huang et al., 2001, Hoomans, 2000, Tsuji et al., 1993, Kuipers et al., 1992, Cundall et al., 1979).

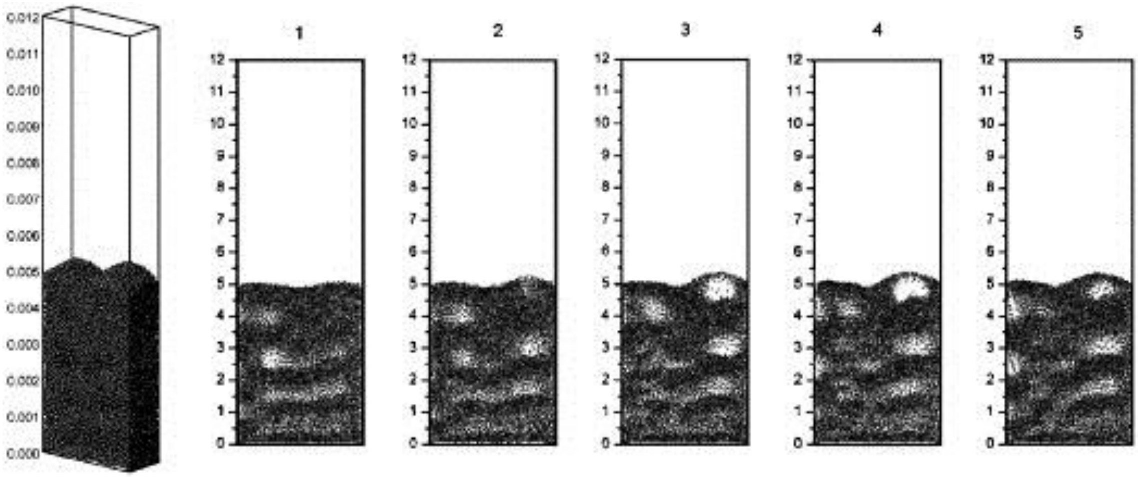

Figure 2.11. The snapshots of the simulation results of the homogeneous fluidization of Geldart A particles. The far left graph shows the fluidized bed in 3D. Graphs 1–5 show the cross sections of bubbling bed(Ye et al., 2005a)

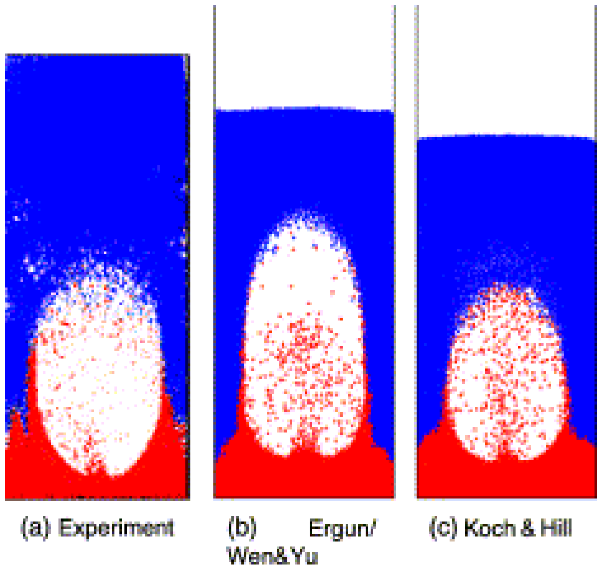

Figure 2.12. Single bubble injection in a monodisperse fluidised bed: comparison of experiment with DPM using different drag models.(Bokkers et al., 2004)

2.1.2.1 Governing equations for Discrete Element Method (DEM) used in this thesis

DEM tracks each particle using Newton's second law of motion, and the fluid phase is described using the averaged equations of motion. DEM has been used and documented somewhere (Huang et al., 2018, Clarke et al., 2018, Zhao et al., 2017, Ye et al., 2005b, Peng et al., 2016, Hoomans et al., 1996, Tsuji et al., 1993). For convenience, it is briefly given below.

The fluid flow is solved by the averaged continuity and momentum equations of the continuum which are given as

$$\frac{\partial(\varepsilon\rho_g)}{\partial t}+(\nabla\cdot\varepsilon\rho_g\mathbf{u})=0 \tag{2.1}$$

$$\frac{\partial(\varepsilon\rho_g\mathbf{u})}{\partial t}+(\nabla\cdot\varepsilon\rho_g\mathbf{uu})=-\varepsilon\nabla p-S_p-\nabla\cdot(\varepsilon\overline{\tau})+\varepsilon\rho_g g \tag{2.2}$$

where ε presents the porosity, g the gravity acceleration, ρ_g the gas density, **u** the gas velocity, $\overline{\tau}$ the viscous stress tensor, and *p* the pressure of the gas phase. The source term S_p is:

$$\mathbf{S_p}=\frac{1}{V}\int\sum_{i=0}^{N}\mathbf{F}_{\mathbf{d},i}\delta(\mathbf{r}-\mathbf{r}_i)dV \tag{2.3}$$

where *V* is the volume of fluid cell and *N* the number of particles in the fluid cell. $\mathbf{F}_{d,i}$ is the drag force acting on particle *i*. The δ-function ensures that the drag force acts as a point force at the particle centre (Zhang et al., 2015).

The Newtonian equation is used to track the motion of particles. The equations for the translational and rotational motion of particle are:

$$m\frac{d^2\mathbf{r}}{dt^2} = \mathbf{F_{cont}} + \mathbf{F_d} - V\nabla p + mg \tag{2.4}$$

$$I\frac{d^2\Theta}{dt^2} = \mathbf{T} \tag{2.5}$$

where m is the mass of particle, the first and second terms are the contact force and drag force, respectively. The third term represents the pressure drag induced by the pressure gradient around the particle. I is the moment of inertia, Θ the angular displacement, and $\mathbf{T}$ the torque of particle. The contact force $\mathbf{F}_{cont}$ includes both normal and tangential components which are given by

$$\mathbf{F}_{cont} = \sum_{contactlist} (\mathbf{F_{ab,n}} + \mathbf{F_{ab,t}}) \tag{2.6}$$

Soft-sphere model is used to calculate the contact force. The normal and tangential components are respectively given by:

$$\mathbf{F_{ab,n}} = -k_n \delta_n \mathbf{n_{ab}} - \eta_n \boldsymbol{\upsilon}_{\mathbf{ab,n}} \tag{2.7}$$

and

$$\mathbf{F_{ab,t}} = \begin{cases} -k_t\delta_t - \eta_t \boldsymbol{\upsilon}_{\mathbf{ab,t}},\ for|\mathbf{F_{ab,t}}| \le \mu_f |\mathbf{F_{ab,n}}| \\ -\mu_f |\mathbf{F_{ab,n}}| t_{ab},\ for|\mathbf{F_{ab,t}}| > \mu_f\ |\mathbf{F_{ab,n}}| \end{cases} \tag{2.8}$$

Here k is the spring stiffness, η the damping coefficient, n_{ab} the normal unit vector, δ_n the overlap, δ_t the tangential displacement, μ_f the friction coefficient and υ_{ab} the relative velocity between two particles.

The drag force $\mathbf{F}_d$ is a combination of Ergun equation (1949) for dense regime and Wen-Yu's drag model (1966) for dilute regime:

$$\mathbf{F}_d = 3\pi\mu_g \varepsilon^2 d_p (\mathbf{u}-\mathbf{v}) f(\varepsilon) \tag{2.9}$$

$$f(\varepsilon) = \begin{cases} \dfrac{150(1-\varepsilon)}{18\varepsilon^3} + \dfrac{1.75}{18}\dfrac{Re_p}{\varepsilon^3}, \varepsilon < 0.8 \\ \dfrac{C_d}{24} Re_p \varepsilon^{-4.65}, \varepsilon \geq 0.8 \end{cases} \tag{2.10}$$

2.1.3 Theoretical research

2.1.3.1 Research status of the dynamic characteristics of particles in gas-solid fluidized bed

The motion of particles in the flow field is caused by force. Particle dynamics is the pattern of motion and force of the particles. Understanding the force o n the particles is the basis for the particle motion description and is of great s ignificance when studying the motion mechanism of single particles and the m otion characteristics of particle groups. Particle dynamics are also often involve d in the systematic modelling of particle fluid systems. Therefore, in this study, the microscopic dynamic characteristics of the particles need to be studied bef ore exploring the macroscopic characteristics (mixing, segregation) of the gas-so lid fluidized bed.

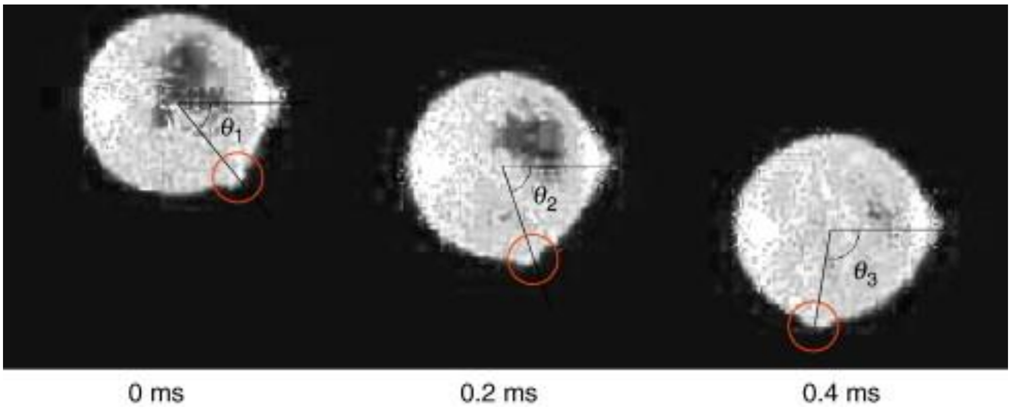

Figure 2.13. Example of rotation speed measurement by experimental method.(Wu et al. 2008a)

In a typical gas-solid two-phase system, the particles are subjected to a drag force, buoyancy force, gravity, contact forces (collisions and friction) between particles and between the particles and the walls, and pressure gradient forces. In some special circumstances, other force terms also apply, such as the Basset force, which is caused by the deviation from the steady-state motion in a viscous fluid, the Saffman lift force, which is generated in a flow field with a velocity gradient, and the Magnus lift force, which is produced by the rotation of particles. At present, most studies focus on the drag force on particles or particle groups. Little research has been conducted on the expression of other forces when particles move in fluids. In this study, these forces will be analysed and a DPM model will be established based on the force analysis.

In a gas-solid two-phase system typified by a fluidized bed, the motion of the particles includes not only translation but also rotation because the particles are not points with no radii but instead have spherical or spherical-like shapes. Rotation occurs when the particles collide non-centrally or when they are in a heterogeneous flow field. Studies by Torobin et al. (1960) have shown that rotational motion affects the linear motion of the particles and, to some extent, the transport and entrainment of the particles in the gas-solid fluidized system. Wu et al. (2008a, 2008b) experimentally investigated the effects of different influencing factors (such as the particle size, density, and particle collision rate) on the particle rotation. It was found that the rotation speed of particles with radii of 0.5 mm and densities of 2400-2600 kg/m3 could reach 300 to 2000 rev/s in a cold circulating fluidized bed riser. Kajishima et al. (2004) studied particle rotation via numerical simulation and found that irrotational particles were more likely to form particle clusters than rotational ones under a shear flow. Similar studies and conclusions were also reported in the work of Wang et al. (2008). Sun et al. (2006) found that the numerical simulation model with the incorporation of particle rotation could better capture the characteristics of bubble dynamics and bed behaviour.

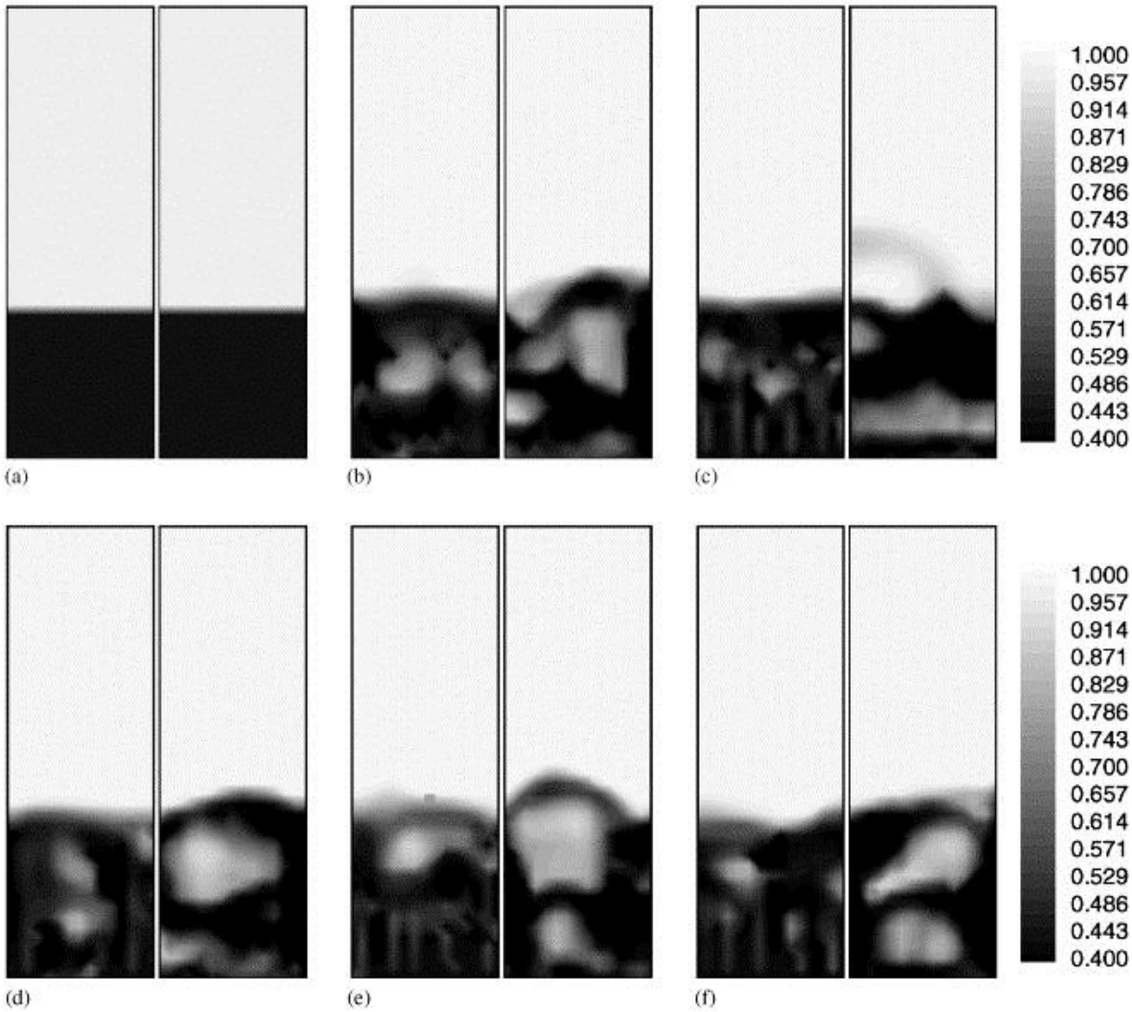

Figure 2.14. Instantaneous gas volume fraction for a bidispersed-fluidized bed at (a) 0 s, (b) 6 s, (c) 10 s, (d) 14 s, (e) 18 s and (f) 20 s. For each subframe, the left side are simulations without particle rotation and the right frame with particle rotation.(Sun et al., 2006)

It is well known that rotating particles in a fluid are subjected to the Magnus lift force. The direction of the Magnus lift force satisfies the left-hand rule, i.e., the direction of this force is perpendicular to the plane defined by the rotation direction and the direction of the relative velocity of the particle with respect to the fluid. The Magnus lift force and the corresponding Magnus effect can explain such phenomena as the arc ball in table tennis and the banana kick in football. In 1672, Newton correctly deduced the reason for the Magnus effect after watching a tennis game match at the Cambridge College (Barkla and Auchterlonie, 1971). In 1852, German physicist Heinrich Magnus described this effect mathematically. Since then, extensive research has been reported on the Magnus effect in particle-fluid systems. Oliver (1962) explained some motion behaviours of particles in a tube by the Magnus effect. White and Schulz (1977) studied the motion of glass beads (with a diameter of 350 μm and a density of 2500 kg/m^3) in an air duct and explained some of the observations with the Magnus effect. Dandy and Dwyer (1990) calculated the drag force and Magnus lift force of a single particle under different Reynolds numbers. They found that the magnitude of the Magnus lift force was much smaller than that of the drag force under the same Reynolds number. You et al. (2003) also found that for small particles (with a diameter of 100 um), the Magnus lift force was negligible compared to the drag force, even with a rotational speed of 10^6 rev/min. However, recent studies have shown that the Magnus lift cannot be ignored in some cases. Zhou et al. (2015a) simulated the particles using the lattice Boltzmann method and showed that the Magnus lift force could not be ignored in dilute fluids with high Reynolds numbers. Researchers have studied the Magnus effect under different working conditions (in terms of the Reynolds numbers). However, there are few reports on the Magnus effect in gas-solid fluidized bed systems.

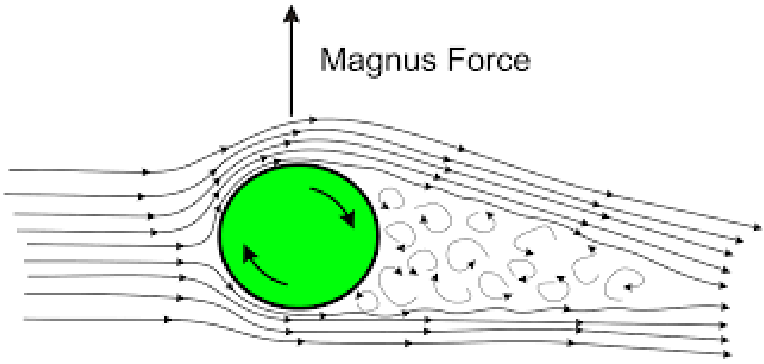

Figure 2.15. Magnus effect

2.1.3.2 Theoretical research status of the mesoscopic structure (bubble)

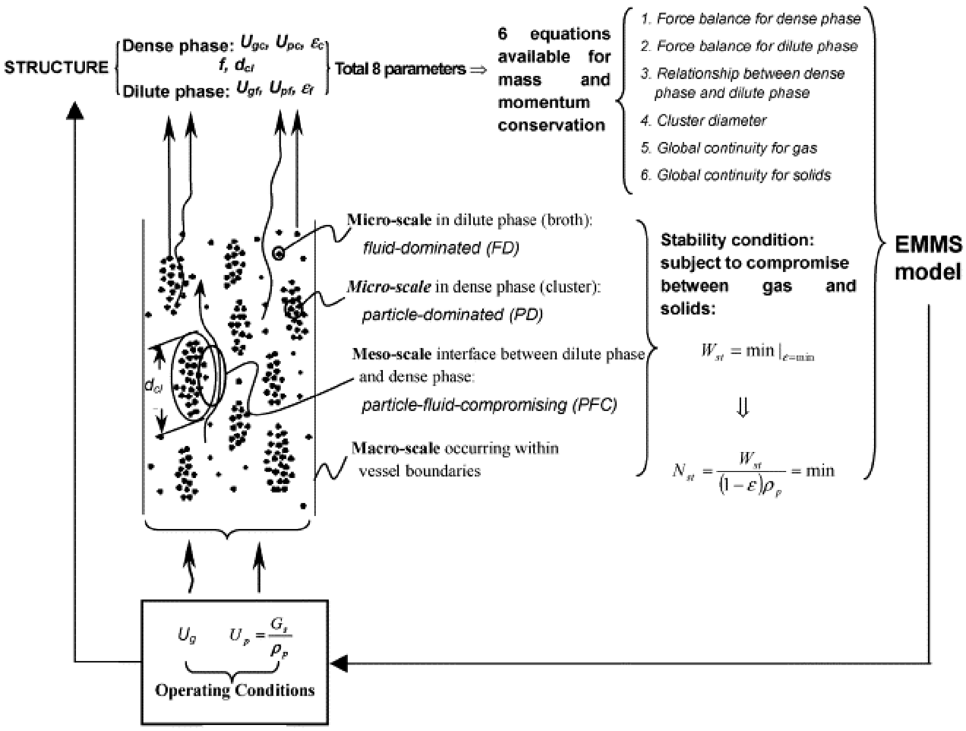

Figure 2.16. Physical basis of the EMMS model (Kwauk and Li 2007).

The force on microscopic particles is the driving force of single particle motion, while the mesoscopic bubble is the driving force of particle mixing in gas-solid fluidized beds (Kwauk and Li 2007). Therefore, studying the formation and evolution mechanism of bubbles is of great significance for exploring particle mixing in gas-solid fluidized beds. Some researchers have studied bubbles by dividing the gas-solid system into a dense phase and a dilute phase, which is called the two-phase model. Tommey and Johnstone (1952) were the first to propose the two-phase concept. They defined the dispersed phase as the dilute phase and the continuous phase as the dense phase. The bubbling fluidization system was studied by the two-phase theory in their work. Davidson (1963) established the Davidson bubble model to describe the motion behaviour of bubbles in a bubbling fluidized bed. Li and Kwauk (2003) established the energy minimization multi-scale (EMMS) theory. In this theory, the system was divided into a dense phase and a dilute phase using a multi-scale method. Eight variables were employed to describe the system and the model was solved based on the concept of energy minimization. The fluidization phenomena of different flow patterns were also analysed in their work. Experimental support or extensive simulations are still required to obtain some specific data, such as the velocity distribution curves of particles around a bubble.

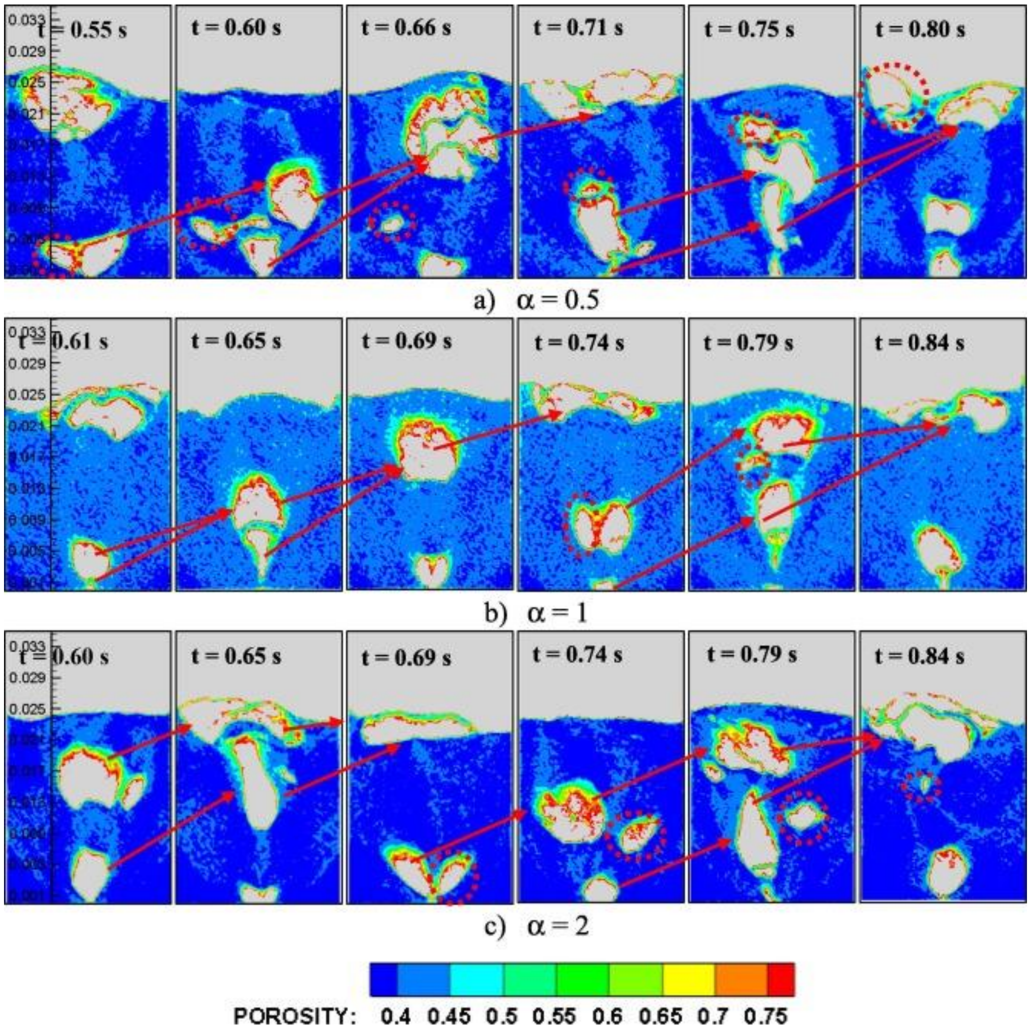

Figure 2.17. Study of bubble dynamics: Flow patterns for different particle shapes when jet velocity is 0.25 m/s (colored by porosity): (a) oblate particles, (b) spheres, and (c) prolate particles. (Shrestha et al., 2019)

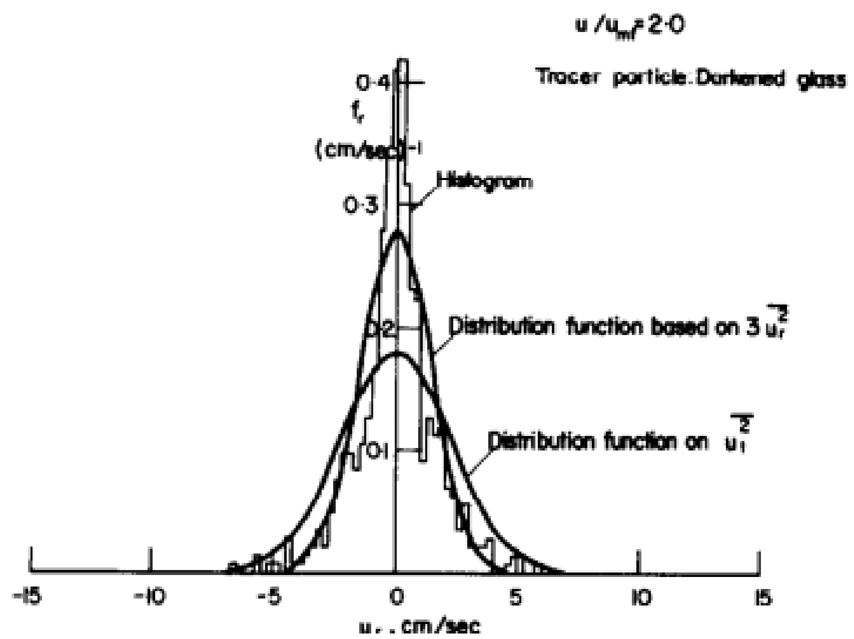

Figure 2.18. Histogram of radial velocities (Maxwell velocity distribution)(Carlos and Richardson 1968)

Currently, most studies believe that the particle velocity distribution in a two-phase system satisfies the Maxwell velocity distribution function. The Maxwell velocity distribution was first employed in molecular gas dynamics to describe the motion of gas molecules with random collisions. Some researchers adopted the concept of the Maxwell velocity distribution to describe the motion of particles in a particle-fluid two-phase system. The Maxwell velocity distribution function for the two-phase system was first experimentally confirmed by Carlos and Richardson (1967, 1968). They studied the velocity distribution of 570 particles in a liquid-solid fluidized bed and concluded that the results were consistent with the Maxwell velocity distribution function. Gidaspow et al. (1994) applied the conclusion of Carlos and Richardson to the deduction of the kinetic theory of granular flow (KTGF). Some researchers believe that the particle velocity distribution in the two-phase system does not fully satisfy the Maxwell velocity distribution. Goldschmidt et al. (2002) noted that in dense gas-solid fluidized beds, the elastic particles satisfy the isotropic Maxwell velocity distribution, whereas the inelastic and rough particles follow the anisotropic Maxwell velocity distribution. Lu et al. (2005) reached a similar conclusion using the method of a hard-sphere model simulation. It was confirmed that the greater the inelasticity is, the greater the tendency of anisotropy is. Kumaran (2009) simulated the collision behaviour of 500 particles in a cubic box. Their work also proved that the velocity distribution of elastic particles followed the Maxwell distribution and the velocity distribution of rough particles was close to the Maxwell distribution. However, the velocity distribution of the inelastic particles was a superposition of the Maxwell distribution and the exponential distribution. Leszczynski et al. (2002) analysed the particle velocity distribution function of different regions in a circulating fluidized bed and used a linear combination of double Maxwell distributions to describe the behaviour of the particle velocities. Wang et al. (2016) theoretically derived the bimodal distribution formed by two superimposed Maxwell distributions in a gas-solid two-phase system based on the EMMS principle and heterogeneity. Liu et al. (2016) applied a large-scale direct numerical simulation (DNS) to analyse the particle velocity fluctuations. Their results showed that the distribution of the particle fluctuation velocity (PFV) satisfied the typical double-discrete mode.

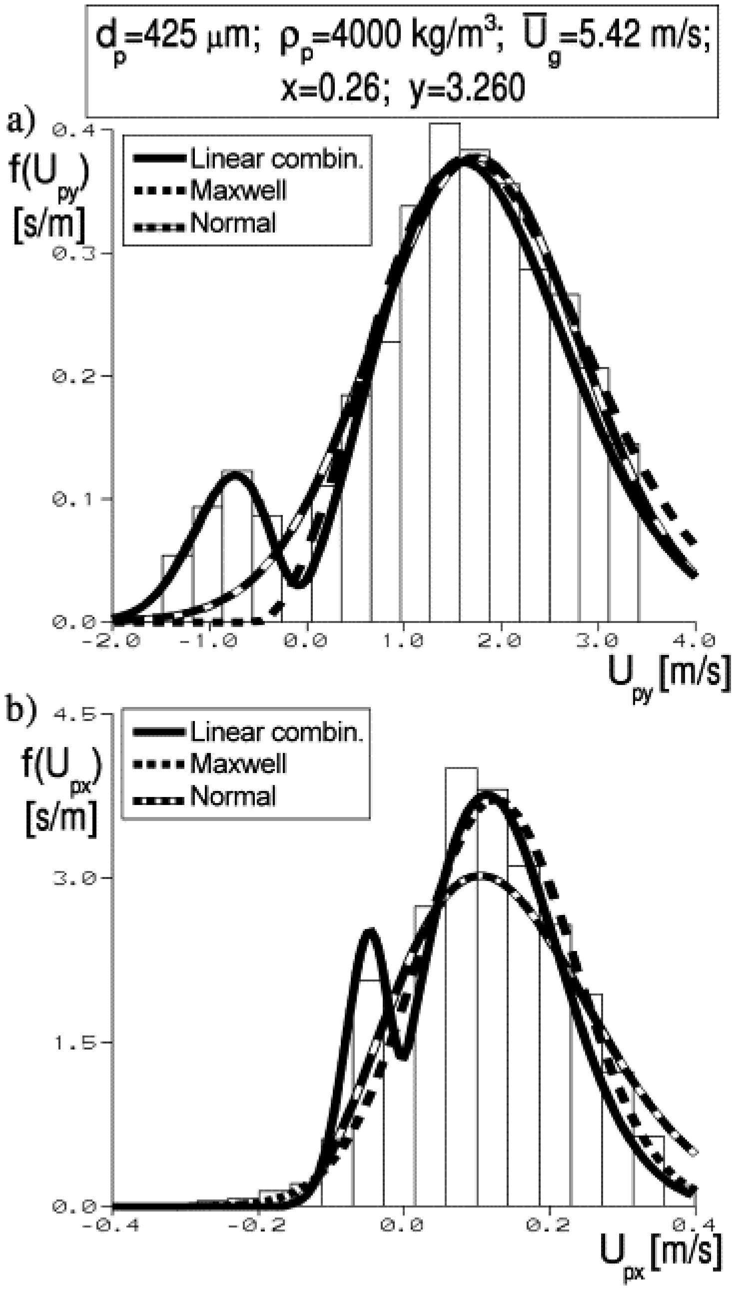

Figure 2.19. Behaviour of different types of distributions in the histogram background: (a) for vertical component of particle velocity, (b) for horizontal component of particle velocity. (Leszczynski et al., 2002)

2.1.3.3 Research status of particle mixing characteristics

The distribution of particles in a multi-component fluidized bed is the result of the dynamic equilibrium of two competing mechanisms: the mixing and segregation of particles. The segregation of particles, also known as classification, is the opposite process of mixing. One may promote the segregation or mixing of particles by adjusting certain conditions, such as the ratio of different particles and the operating parameters. The ideal material system in a fluidized bed is a system with a uniform density and uniform particle size, so that the influence of the material characteristics on the mixing and segregation behaviours can be neglected. Therefore, previous studies are mostly based on one-component systems. However, the actual production operation is often a process that involves mixing multi-component particles. The biomass fluidized bed is such a example. Since biomass is difficult to fluidize, bed materials such as quartz sand are often added to promote the fluidization and heat transfer. This is a typical two-component bubbling fluidized bed. It is of great significance to study the mixing and segregation of particles for the design and operation of bubbling fluidized beds.

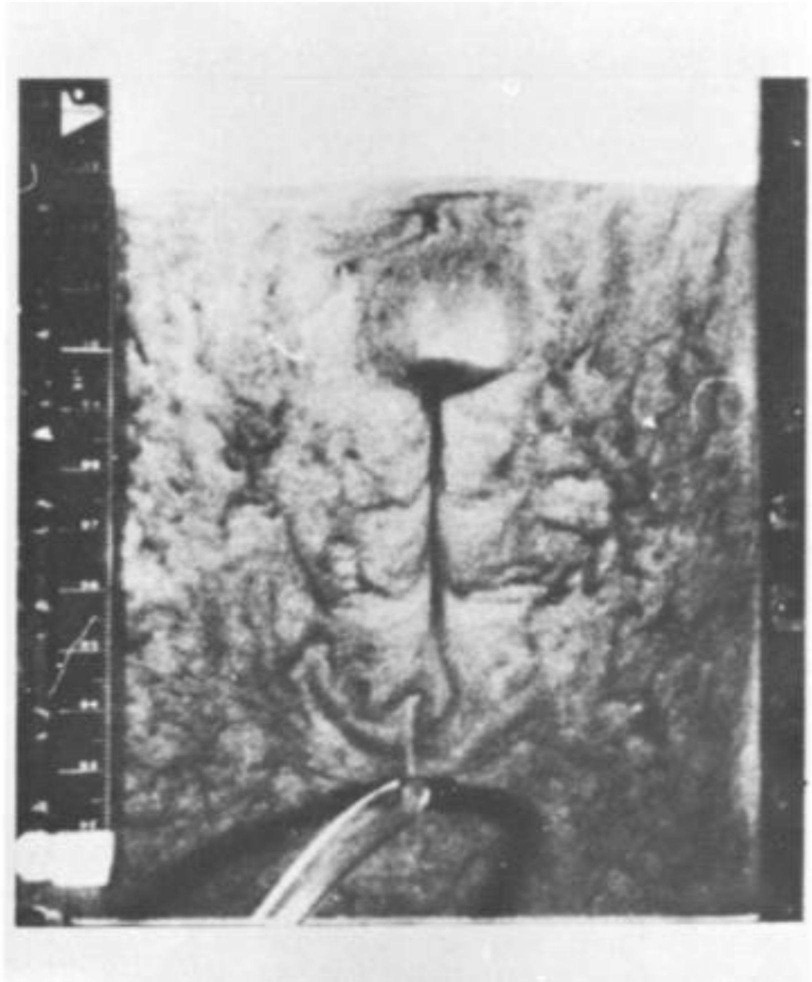

Figure 2.20. A jetsam layer punctured by successive bubbles that have caused segregation and mixing. (Rowe and Nienow 1976)

The particle segregation and mixing mechanisms have been described in earlier studies (Marsheck and Albert, 1965, Gibilaro and Rowe, 1974, Chen and Keairns, 1975, Rowe and Nienow, 1976, Nguyen et al., 1977, Masson, 1978, Nienow et al., 1978, Fan and Chang, 1979, Nienow and Naimer, 1980, Chen, 1981, Tanimoto et al., 1983, Hoffmann et al., 1993). Rowe et al. (Rowe and Nienow, 1976) were the first to classify the two-component particle system into "Jetsam" (component tends to settle to the bottom) and "Flotsam" (component tends to float). Their research suggests that large or heavy particles will deposit in the lower part of the bed during fluidization, which is called the Jetsam, and small or light particles will float to the top of the bed, which is called the Flotsam. The fundamental reason for particle segregation is that different bed densities are formed by particles with different physical properties during fluidization:

$$\begin{cases} \rho_{B1} & = (\rho_{p1} - \rho_f)(1 - \varepsilon_1) \\ \rho_{B2} & = (\rho_{p2} - \rho_f)(1 - \varepsilon_2) \end{cases} \tag{2.10}$$

when $\rho_{B1} > \rho_{B2}$, component 1 is the Jetsam and component 2 is the Flotsam.

In a bubbling fluidized bed, the rise of the bubbles is a major factor in particle segregation and mixing (Yang, 1986). When the bubble rises, the bubble wake carries the particles up. The empty space created after the bubble leaves is replenished by the particles around the bubble, causing the particles to flow upward in the region where the bubble passes through. To balance the rise of the bed material, particles in the adjacent bubble-free regions flow downward. The Jetsam and Flotsam are segregated or mixed by this process.

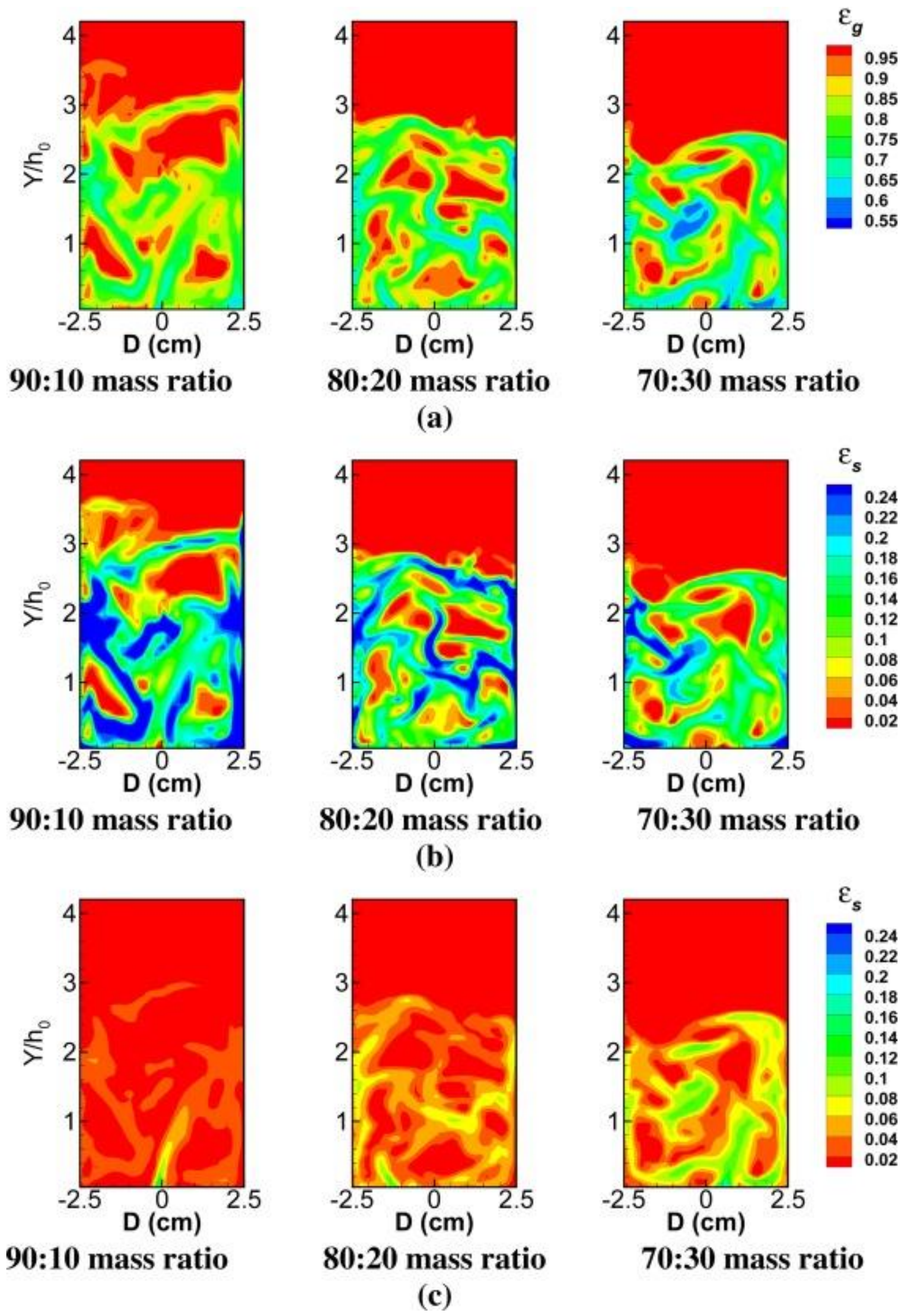

Figure 2.21. Instantaneous volume fraction contours for all mass ratios of coal–poplar wood at Ug = 9.87 cm/s for (a) gas, (b) coal and (c) poplar-wood.(Estejab et al., 2017)

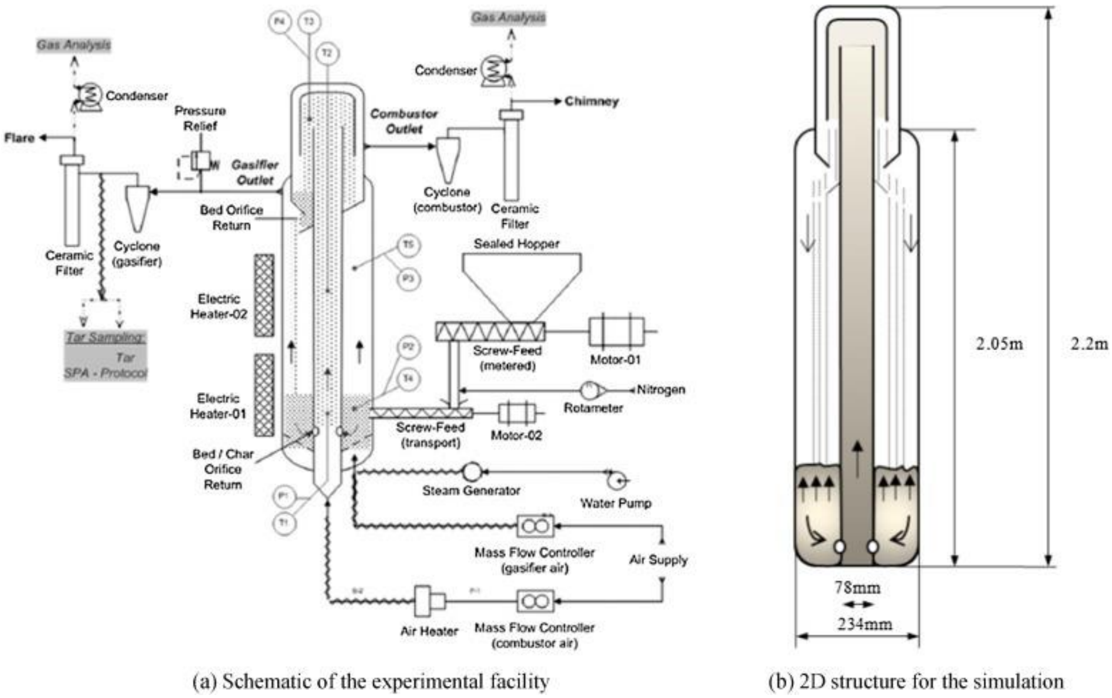

Figure 2.22. Structure scheme of fluidized bed by Chen et al(Chen et al., 2017): (a) Schematic of the experimental facility, (b) 2D structure for the simulation model.

Recent studies on particle mixing and segregation in fluidized beds can be found in the literature (Ali et al., 2018, EI-Sayed et al., 2019, Kong et al., 2018, Ke et al., 2017, Estejab et al., 2017, Chen et al., 2017, Brachi et al., 2017, Wang et al., 2015, Fotovat et al., 2015, Zhang et al., 2013, Zhang et al., 2009b). Researchers have investigated the mixing and segregation characteristics of particles in fluidized beds based on different research backgrounds, different fluidized bed structures, and different research methods. Estejab et al. (2017) explored the mixing characteristics of Geldart A particles in a bubbling fluidized bed. Chen et al. (2017) developed a mixing model for particles in a biomass gasification circulating fluidized bed. Wang et al. (2015) investigated the nonlinear characteristics of particles in a multi-component two-dimensional fluidized bed using Hilbert-Huang transformation theory. Zhang et al. (2013) studied binary mixtures with different shapes, different weights, and different sizes in a fluidized bed using microwave heating-infrared thermal imaging technology and improved insert sampling technology. The effects of the mixing time, gas velocity, and material ratio on the particle mixing behaviour were studied in detail.

The above studies are mostly concerned with two-component particle systems. Multi-component systems can be considered to be several two-component particle systems if complete segregation can be achieved. Nienow et al. (1997) compared the results of individual experiments on two-component systems with the experimental results of a three-component system. It was found that for a three-component system that consisted of different distinct types of particles, the presence of the third component had almost no effect on the segregation mode of the other two components. However, not all multi-component systems can be broken down into a combination of several two-component particle systems for the actual segregation processes. There have been few studies on the segregation and mixing of multi-component particles and the corresponding segregation mode requires further investigated.

2.2 Summary and research gap

(1) At the mesoscopic structure (bubble) scale, previous studies have shown that, unlike the Maxwell velocity distribution for uniform systems based on the kinetic theory of gases, the velocity distribution of particles in gas-solid two-phase systems has certain heterogeneity. Different researchers have described the velocity distribution functions differently because of different research scales and perspectives. There is no detailed experimental or theoretical study on the velocity distribution of particles around bubbles.

(2) In the exploration of particle mixing characteristics at the macroscopic scale, first, previous studies have mostly focused on the effects of different operations or different material parameters (e.g., gas velocity, particle size, density) on the fluidization and mixing characteristics based on the same type of fluidized bed, such as a single nozzle spout-fluid bed or a uniform air distribution type bubbling fluidized bed. However, there are few studies comparing the mixing characteristics of different fluidized beds. Second, in regard to mixing theory, researchers have developed particle mixing models for bubbling fluidized beds, spout-fluid beds, and circulating fluidized beds. These mixing models can predict the degree of mixing to some extent. However, for actual production processes represented by biomass fluidized beds, the particle systems are usually multi-component with a wide particle size distribution. Since the theoretical models often fail to reflect the actual mixing situation, it is therefore

necessary to experimentally study the mixing of particles with a wide particle size distribution.

(3) On the subject of experimental methods, first, most particle velocity measurement methods such as PIV can accurately measure the velocity distribution of dilute phase particles. However, it is difficult to measure the particle velocity distribution for dense-phase fluidized beds, such as the bubbling fluidized bed. To accurately measure the particle velocity distribution in a dense-phase fluidized bed, certain improvements in the fluidized bed or measurement method are required. Second, for the particle mixing experiment method, the sampling method is often unable to reflect the mixing characteristics of the particles in real time, and the image analysis method has the disadvantage of requiring expensive equipment. Therefore, the experimental method of particle mixing also needs to be improved.

(4) In terms of microscopic particle dynamics, previous studies have focused on the drag force on particles in fluids. There have been few studies involving particle rotation and the Magnus lift force. Many researchers have studied the Magnus effect based on different operating conditions (Reynolds number) and reached different conclusions. Therefore, before studying the macroscopic mixing characteristics, it is necessary to establish a calculation model for the gas-solid fluidized bed, understand the influence of the Magnus effect on the gas-solid fluidized bed, and explore the

application scope of the Magnus effect. Then, the computational fluid dynamics CFD-DEM model is adjusted accordingly for the following research.

2.3 Research aims and thesis structure

The aim of this project is to investigate the regularity of particle velocity distribution and particle mixing in fluidized bed by using experimental and computational method. For achieving research aim, based on four research gaps above, four Chapters will be shown and discussed in this project.

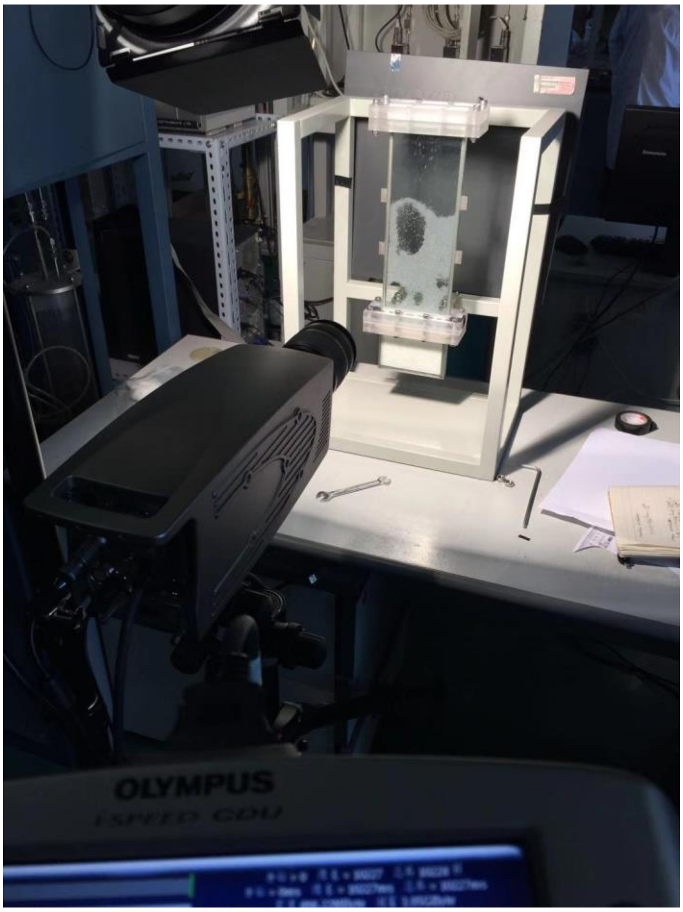

Figure 2.23. Schematic of the PIV experiment device in Chapter 3

In Chapter 3, a particle image velocimetry (PIV) system is employed to measure the particle velocity fields of different forms of two-dimensional local bubbles to obtain the particle speed distribution function in the area. Discrete particle modelling is also used to simulate bubbles in fluidized bed. A tri-peak model based on the fluid and particle control mechanism is theoretically derived. Three kinds of models: a tri-peak model, a bi-peak model and a single-peak model are proposed to fit the experimental data.

In Chapter 4, discrete particle model is used to simulate fluidized beds with different jet numbers, and the results are validated by physical experiments. Cases with different jet numbers (varying from one to five) but the same gas flow rates are compared in terms of the maximum bed pressure drop, bed height, mixing index, particle velocities and contact number.

Figure 2.24. Schematic of the fluorescent tracer experiment device in Chapter 5

In Chapter 5, a fluorescent tracer technique combining image processing method has been used to investigate the mixing and segregation behavior in a binary fluidized bed with wide size distributions. The particle number percentage in each layer for different gas velocities is obtained by an image processing method. Fluidization, mixing and segregation behaviour have been discussed in terms of bed pressure drop, gas velocity and mixing index. Different types of binary particle systems, including the jetsam and the flotsam-rich system, are analyzed and compared. The mixing indexes at different minimal fluidization velocities are also analyzed and compared with other work.

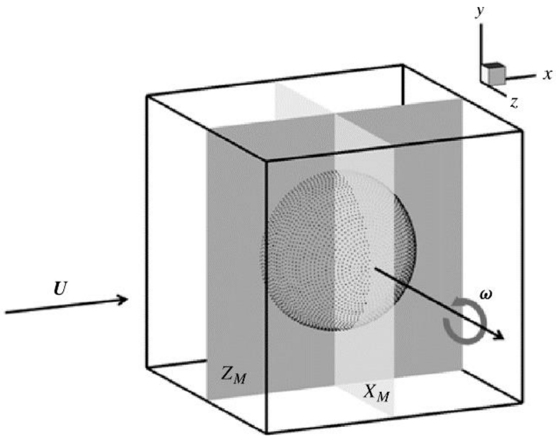

Figure 2.25. Magnus effect for particles in fluidized bed will be discussed in Chapter 6

In Chapter 6, a pseudo two-dimensional discrete particle model (DPM) was used to investigate the influence of Magnus lift force in fluidized bed. The rotational Reynolds number (Re_r) bases on the angular velocity and the diameter of the spheres is used to characterize the rotational movement of particles. We studied the influence of Magnus lift force for particles with rotational Reynolds number in the range of 1~100.

CHAPTER 3 PARTICLE VELOCITY DISTRIBUTION FUNCTION AROUND A SINGLE BUBBLE IN GAS-SOLID FLUIDIZED BEDS

3.1 Introduction

In this work, based on a typical mesoscopic-scale heterogeneous structure surrounding a bubble, the velocity distribution function of particles is investigated. Furthermore, a tri-peak expression of the velocity distribution function is proposed based on the fluid and particle control mechanism. Three kinds of models of tri-peak, bi-peak and single-peak models are compared and discussed in detail.

3.2 Method description

3.2.1 Experimental setup

The technique of particle image velocimetry (PIV) provides the possibility for the study of particle behaviour. For example, Duursma et al. (2001) used PIV to produce vector maps of the gas-phase flow in the freeboard region of fluidized beds. Bokkers et al. (2004) used PIV to obtain the particle velocity profile in the vicinity of a bubble in a dense fluidized bed. Link et al. (2010) investigated particle movement in a spout-fluid bed by the PIV technique and hard-sphere based DPM simulation, and showed a similar influence of the background fluidization velocity on the spout behaviour. Dijkhuizen et al. (2010) extended the PIV method to simultaneously measure the local instantaneous granular temperature, and found that direct lighting gives better results than indirect lighting in the experimental setup. Muller et al. (2007)

analysed the motion and eruption of a bubble at the surface of a two-dimensional (2D) fluidized bed using PIV.

In this study, the experiments were performed in a pseudo-2D fluidized bed, as shown in Fig. 3.1. The fluidized gas is air, and particles are 1 mm glass balls in diameter with a narrow grain size distribution. The bed layer thickness is 1.5 mm. This ensures that only one layer of observable particles exists along the thickness direction, which ensures the accuracy of images captured and velocity field processing and analysis. The minimum fluidization velocity U_{mf} is 0.887 m/s which was calculated by the relationship of pressure drop with gas superficial velocity.

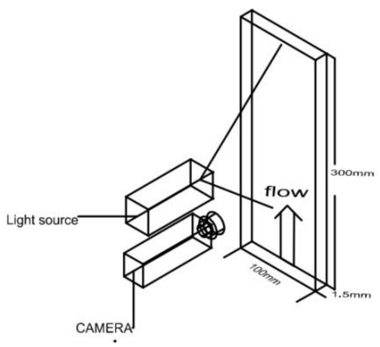

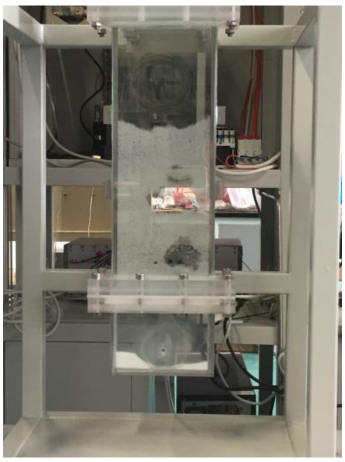

(a) (b)

Figure 3.1. (a) Schematic of the PIV experiment device, and (b) Pseudo-2D cold fluidized bed.

Image capture was performed using Olympus i-VELOCITY automatic high-velocity camera, and the recording rate was 1000 fps. The captured images were processed to identify particles via grey scale differences and calculate the particle spatial distribution. As particles were present in large quantities and at high density, the particles in two consecutive frames were matched via cross-correlation theory, and the cross-correlation of particle images was calculated to obtain the velocity field and velocity distribution.

In this work, cross-correlation analysis was performed via fast Fourier transform (FFT) to obtain the particle velocity (Willert and Gharib, 1991). The analytical process is shown in Fig. 3.2. Briefly, in the same position, two sampled regions, f(m,n) and g(m,n), with identical dimensions were selected. Images of f and g were subjected to FFT to obtain expressions F(m,n) and G(m,n) in the frequency domain. Then, the spatial frequency domain operation was performed to calculate the cross-correlation function Φ in the frequency domain. Φ was subjected to reverse Fourier transform to obtain the cross-correlation function ϕ. The cross-correlation peak was identified to determine the particle displacements dx and dy. These displacements were then divided by the time interval between the two images to obtain the particle velocity.

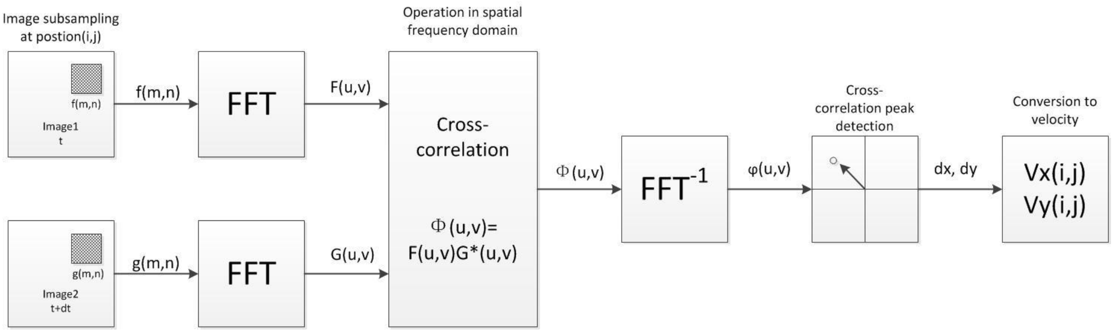

Figure 3.2. Cross-correlation calculation procedure for the analysis of PIV experiment data.

3.2.2 Discrete element method (DEM)

DEM tracks each particle using Newton's second law of motion, and the fluid phase is described using the averaged equations of motion. DEM has been used and documented somewhere (Ye et al., 2005b, Peng et al., 2016, Hoomans et al., 1996, Tsuji et al., 1993). The equations are listed in section 2.1.2.1.

3.2.2.2 Simulation conditions

The simulation parameters are listed in Table 3.1. A pseudo-2D fluidized bed model with 100 mm in width, 7 mm in depth and 1000 mm in height is used to simulate experimental fluidized bed. The parameters such as gas temperature, gas viscosity and molar mass, particle size and density, are determined based on air properties used in the experiment. For restitution coefficient and friction coefficient, the values were chosen from our previous works (Liu et al. 2018). The sensitivity of model prediction based on particle spring stiffness *k* was examined. The results showed that the overlap

δ_n would less than 5% of particle diameter and the gas-solid flow characteristics were almost independent of the value of spring stiffness after the value exceeds 10^4 N/m. This is consistent with the work by Peng et al. (2016). Therefore, the values of 7×10^4 N/m and 2×10^4 N/m for the normal and tangential spring stiffness were chosen in this work.

Table 3.1. Simulation parameters

Parameter	Value	Unit
Gas temperature, T	293	(K)
Shear viscosity of gas, μ_g	1.8×10^{-5}	(Pas)
Molar mass of gas, M	2.9×10^{-2}	(kg/mol)
Number of particles, N_{part}	80000	(-)
Diameter of particle, D	1.0×10^{-3}	(m)
Density of particle, ρ_s	2400	(kg/m^3)
Bed width, w	1.0×10^{-1}	(m)
Bed depth, d	7.0×10^{-3}	(m)
Bed height, h	1.0	(m)
Normal restitution coefficient, e_n	0.97	(-)
Normal restitution coefficient wall, $e_{n,w}$	0.97	(-)
Tangential restitution coefficient, e_t	0.33	(-)
Tangential restitution coefficient, $e_{t,w}$	0.33	(-)
Friction coefficient, μ	0.1	(-)
Time step, Δt	1.0×10^{-5}	(s)
Time step for data save, Δt_s	1.0×10^{-3}	(s)

3.3 Results and analysis

3.3.1 Comparison of experimental and simulation results

Fig. 3.3 shows the bubble snapshots and flow patterns obtained from experiment (top row) and simulation (bottom row), demonstrating consistent results. Also, the shape of bubbles agree with typical characteristic as described by Kunii et al. (1991). Bubbles are not spherical but flattish and even concave at the bottom. This is because the rising bubble drags a wake of particles up the bed behind it and those particles change the bubble shape. Fig. 3.4 presents the corresponding particle velocity vector field around the bubble from experiment (left) and simulation (right). Note that in experiment, limited particles velocity vector are detected by PIV technology because only one layer of observable particles exists along the thickness direction. More detailed information for particle velocity can be obtained in the simulation results. The colours represented different value of particle velocity. As shown in Fig. 3.4, particles below the bubble have large velocity because they are stirred up by the bubble trailing vortex. Particles around bubble have negative velocity. Some studies (Collins, 1982, Rowe et al., 1964) use "cloud pattern" to describe the region of those particles. Particles far from bubble have low velocity. This is because that according to Eqs. (3.9) and (3.10), lower porosity ε results in lower drag force and decreases particle velocity. On the other hand, the results from both experiment and simulation show that particles at the top drop along both sides of bubble and particles at the bottom constitute the bulk of trailing wake, and rise along the bubble. The similar trend can also be found in the early theoretical studies (Rowe et al., 1964).

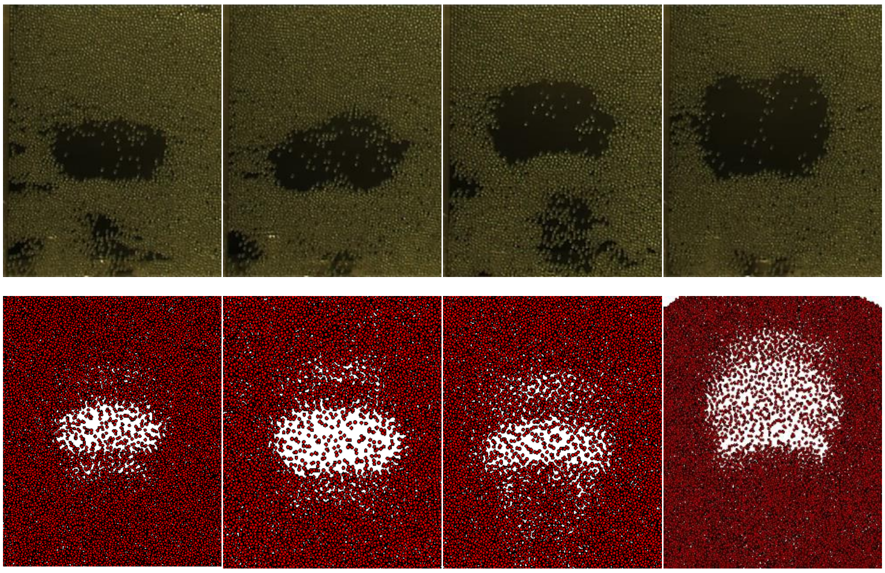

(a) (b) (c) (d)

Figure 3.3. Snapshots of flow patterns (top - experiments, bottom – DEM simulation) under various gas velocities: (a) U_g = 1.22 m/s, (b) U_g= 1.33 m/s, (c) U_g = 1.44 m/s, (d) U_g = 1.66 m/s

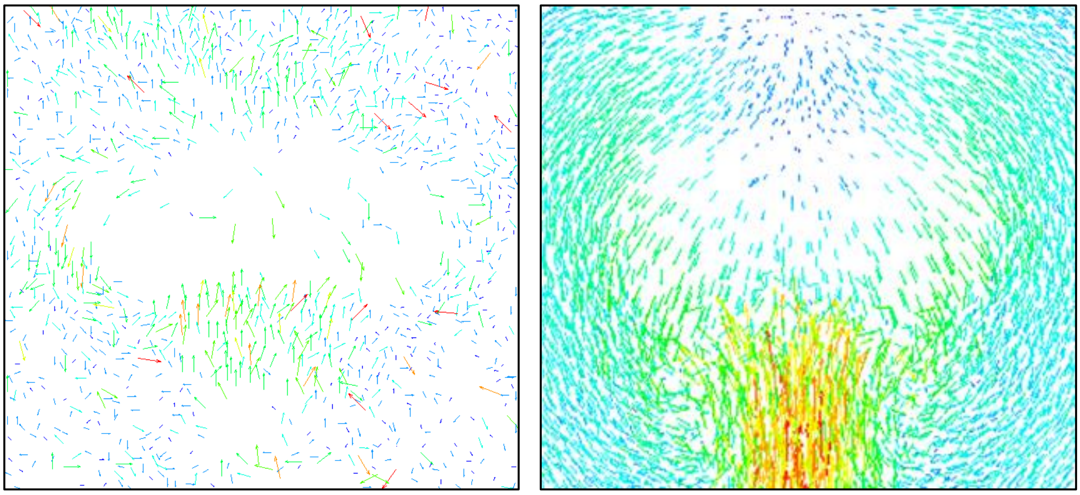

Figure 3.4. Comparison of particle velocity vector field: experiment (the left figure) vs DEM simulation (the right figure).

Fig. 3.5 shows particle velocity distribution determined via experiment and simulation under various gas velocities. The velocity distribution is the average of 30 snapshots for each gas velocity. Note that the particle number in each snapshot is different. Therefore, we define $F(c)$ as $F(c)dc = \frac{f(c)dc}{n}$, where $F(c)dc$ indicates the particle number ratio in the velocity range [c, $c + dc$]. Compared with the experiment, particle velocity distribution curves from simulation is smoother because of more data points obtained from simulation. Although the bubbles have different shapes, the velocity distribution curves are basically consistent and follow similar patterns. For example, all the figures show the feature of "multi-peaks" for velocity distribution. This means that the Maxwellian single-peak velocity distribution curve may not accurately reflect the particle velocity distribution surrounding a bubble. When the gas velocity changes, the peak also changes. The first peak on the left decreases with the increase of gas velocity. The second peak shifts to the right and other peaks become more obvious compared with the low gas velocity cases. This may be because bubble size will increase with increasing gas velocity.

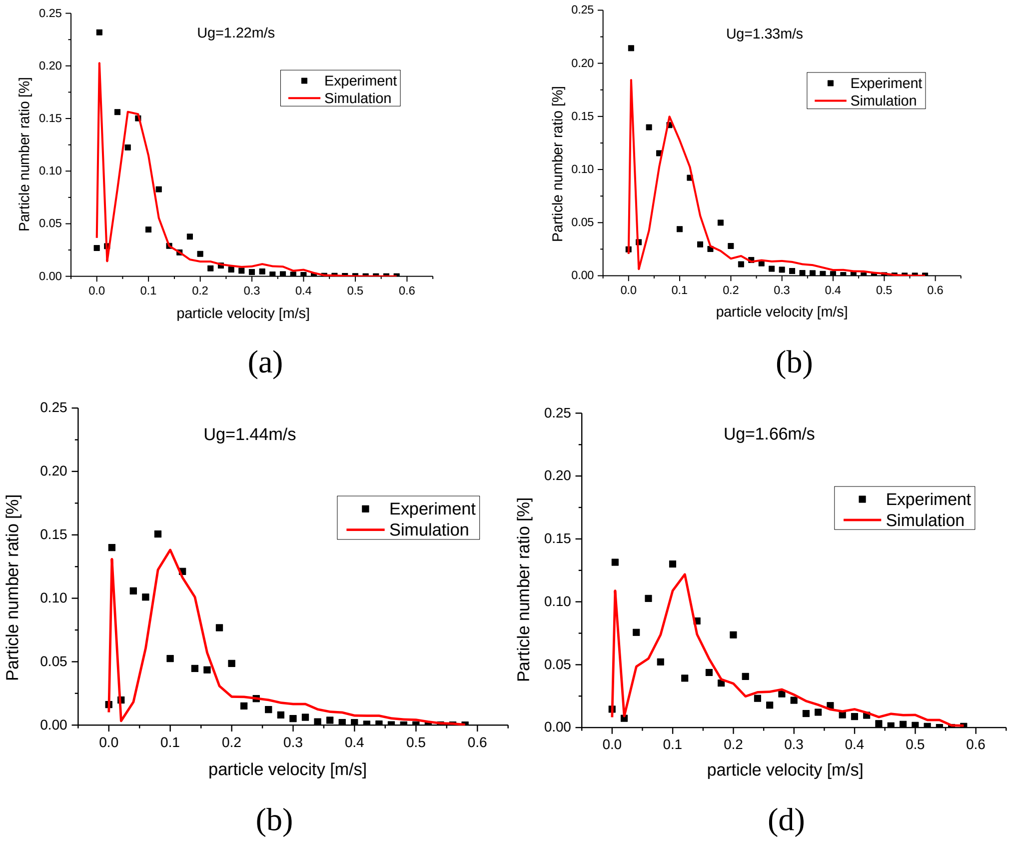

Figure 3.5. Particle velocity distribution determined via experiment under various gas velocities: (a) Ug =1.22m/s, (b) Ug =1.33m/s, (c) Ug =1.44m/s and (d) Ug =1.66m/s.

3.3.2 Particle velocity distribution in different domain

The selected domain size may impact the characteristics of particle velocity distribution. Therefore, the effect of domain size on particle velocity distribution is examined. Fig. 3.6 shows a particle velocity vector field for a typical bubble. Three different sized domains are chosen for analysis, and the corresponding particle velocity distribution curves are shown in Fig. 3.7. Based on the method of Li et al. (2003), the particles are divided into three categories according to particle-fluid interaction mechanism. The particles inside the bubble correspond to the rightmost peak of the distribution curve in domain 1. The particles in this region are in dilute phase and are stirred up by the bubble trailing vortex. They have a small quantity but high velocity, belonging to the fluid dominating (FD) category. The particles around the bubble correspond to the second peak in domain 1 or the peak in domain 2 shown in Fig. 3.7. The particles in this region are in relatively dense phase and fall into the particle-fluid compromising (PFC) category. The remaining particles are less susceptible to the gas velocity. Therefore, the velocity is close to zero, and they belong to the particle dominating (PD) category. This corresponds to the first peak near the zero point in domain 3. Domain 2 could be better to describe the velocity feature in Fig. 3.6 (U_g = 1.22 m/s), because particles far from bubble is not the interest of study. However, for large gas velocity cases, bubbles may be large and the information near the bubble may be missing. Therefore, in this study, to fully and comprehensively describe the characteristics of particle movement around a single bubble, particle velocity distribution for domain 3 (80 × 80 mm) will be used and discussed in the following analysis.

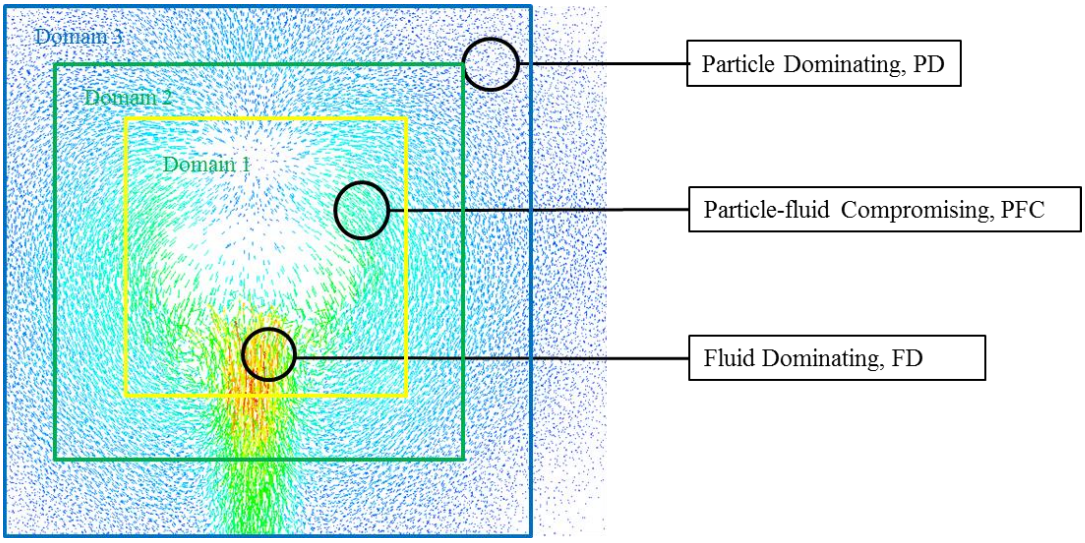

Figure 3.6. Particle velocity field for a typical bubble ($U_g = 1.22$ m/s): (a) domain 1: 40×40 mm, (b) domain 2: 60×60 mm, and (c) domain 3: 80×80 mm)

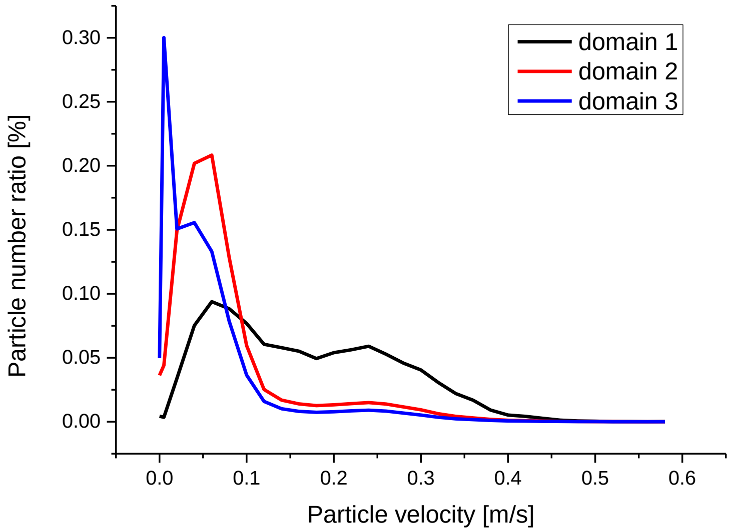

Figure 3.7. Particle velocity distribution at different selected domains.

3.3.3 Tri-peak model

3.3.3.1 Velocity distribution function

The velocity distribution function is the foundation of particle dynamics theory. Normally, the particle velocity distribution follows a Maxwellian single peak distribution:

$$f_M(\mathbf{c}/u,n,\theta)dxd\mathbf{c} = n(\frac{1}{2\pi\theta})^{\frac{3}{2}}exp(-\frac{(\mathbf{c}-\mathbf{u})^2}{2\theta})dxd\mathbf{c} \tag{3.11}$$

where θ is the granular temperature, **u** is the particle average velocity, **c** is the particle velocity and *n* is the particle quantity density.

Wang et al. (Wang, Zhao, and Li 2016) suggested that the single-peak distribution based on gas molecular dynamics theory was not an accurate representation of the heterogeneity in a fluidized bed. Therefore, a dual-peak distribution based on EMMS theory was proposed:

$$f(\mathbf{c}/u,n,\theta) = (1-f)n_f(\frac{1}{2\pi\theta_f})^{\frac{3}{2}}exp(-\frac{(\mathbf{c}-\mathbf{u}_f)^2}{2\theta_f}) + fn_c(\frac{1}{2\pi\theta_c})^{\frac{3}{2}}exp(-\frac{(\mathbf{c}-\mathbf{u}_c)^2}{2\theta_c}) \tag{3.12}$$

where *f* represents the proportion of dense phase, the first term represents the velocity distribution of dilute-phase particles, the second term represents the velocity distribution of dense-phase particles, and the overall velocity distribution is a superposition of the two.

It is worth noting that particle velocity **c** in Eqs. (3.11) and (3.12) is a vector with three components. As this work only involves the value of the particle velocity, scalar functions and velocity distribution functions are investigated. Eqs. (3.11) and (3.12) cannot be used directly. On the other hand, because the velocity determined via the experiment only has components in two directions, the velocity distribution functions should be two-dimensional.

In this work, the Maxwellian distribution is used as an example to derive the two-dimensional velocity distribution function. For more details about the derivation process, see Appendix. The Maxwellian velocity distributions for two-dimensional particle motion are as follows:

$$f_M(c/u,n,\theta)=n(\frac{1}{\theta})exp(-\frac{(c-u)^2}{2\theta})c \tag{3.13}$$

Based on the above, the dual-peak distribution curve was modified to match the particle velocity distribution of particles around single bubble. Using a derivation method similar to Wang et al. (Wang, Zhao, and Li 2016), the dense phase of the second term in the dual-peak distribution in Eq. (3.12) is expanded:

$$n_c(\frac{1}{2\pi\theta_c})^{\frac{3}{2}}exp(-\frac{(\mathbf{c}-\mathbf{u}_c)^2}{2\theta_c})=f'n_{pfc}(\frac{1}{2\pi\theta_{pfc}})^{\frac{3}{2}}exp(-\frac{(\mathbf{c}-\mathbf{u}_{pfc})^2}{2\theta_{pfc}})+(1-f')n_{pd}(\frac{1}{2\pi\theta_{pd}})^{\frac{3}{2}}exp(-\frac{(\mathbf{c}-\mathbf{u}_{pd})^2}{2\theta_{pd}}) \tag{3.14}$$

where f' represents the proportion of PFC particles in the total volume. The first term which represents the dilute phase can be regarded as particles by fluid dominating (FD) category:

$$n_f(\frac{1}{2\pi\theta_f})^{\frac{3}{2}}exp(-\frac{(\mathbf{c}-\mathbf{u}_f)^2}{2\theta_f}) = n_{fd}(\frac{1}{2\pi\theta_{fd}})^{\frac{3}{2}}exp(-\frac{(\mathbf{c}-\mathbf{u}_{fd})^2}{2\theta_{fd}}) \tag{3.15}$$

Then, the final tri-peak distribution curve is as follows:

$$\begin{aligned} f(\mathbf{c}) =&(1-f)n_{fd}(\frac{1}{2\pi\theta_{fd}})^{\frac{3}{2}}exp(-\frac{(\mathbf{c}-\mathbf{u}_{fd})^2}{2\theta_{fd}}) + f'fn_{pfc}(\frac{1}{2\pi\theta_{pfc}})^{\frac{3}{2}}exp(-\frac{(\mathbf{c}-\mathbf{u}_{pfc})^2}{2\theta_{pfc}}) \\ &+ (1-f')fn_{pd}(\frac{1}{2\pi\theta_{pd}})^{\frac{3}{2}}exp(-\frac{(\mathbf{c}-\mathbf{u}_{pd})^2}{2\theta_{pd}}) \end{aligned} \tag{3.16}$$

For the particle velocity distribution in a 2D experiment, Eq. (3.16) can be rewritten as:

$$\begin{aligned} f(c) =&(1-f)n_{fd}(\frac{1}{\theta_{fd}})exp(-\frac{(c-u_{fd})^2}{2\theta_{fd}})c + f'fn_{pfc}(\frac{1}{\theta_{pfc}})exp(-\frac{(c-u_{pfc})^2}{2\theta_{pfc}})c \\ &+ (1-f')fn_{pd}(\frac{1}{\theta_{pd}})exp(-\frac{(c-u_{pd})^2}{2\theta_{pd}})c \end{aligned} \tag{3.17}$$

Eq. (3.17) describes the motion of particles around a bubble. The first term represents the Maxwellian velocity distribution of dilute-phase particles, the second term represents the Maxwellian velocity distribution of dense-phase particles, which are significantly affected by the fluid, and the third term represents the Maxwellian velocity distribution of dense-phase particles that are less susceptible to the fluid. These three terms correspond to the three peaks in the analysis described above.

The parameters in Eq. (3.17) (such as u_{fd}, θ_{fd}) are difficult to obtain in the experiment. For convenience, Eq. (3.17) may be presented as follows:

$$f(c) = Af_{M1}(c) + Bf_{M2}(c) + Cf_{M3}(c) \tag{3.18}$$

where *A*,*B* and *C* represent the proportion of each peak, respectively. $f_{M1}(c)$, $f_{M2}(c)$ and $f_{M3}(c)$ are the correction of the overall Maxwellian distribution which represent FD, PFC and PD particles, respectively.

$$\begin{cases} f_{M1}(c) = & n(\frac{1}{a_1\theta})exp(-\frac{(c-a_2u)^2}{2a_1\theta})c \\ f_{M2}(c) = & n(\frac{1}{b_1\theta})exp(-\frac{(c-b_2u)^2}{2b_1\theta})c \\ f_{M3}(c) = & n(\frac{1}{c_1\theta})exp(-\frac{(c-c_2u)^2}{2c_1\theta})c \end{cases} \tag{3.19}$$

Here n, u and θ are particle number, the value of average particle velocity and granular temperature for all particles in the selected domain. The correction factors are empirical which may be related to gas flow rate, bubble diameter, etc.

3.3.4 Fitting curves with different model

In this section, three kinds of Maxwellian models are proposed and compared. The single-peak model distribution is used first to fit the average experimental data:

$$f(c) = Bf_{M2}(c) \tag{3.20}$$

Fig. 3.8 shows single-peak distribution curves compared with experimental data. It is difficult to profile the real particle velocity distribution. This is because a Maxwellian distribution is to describe the motion of random gas molecule collisions or fine particles in a fluidized bed. However, for a small regional single bubble, especially for Geldart D particles, the heterogeneity become obvious and the effect of gas on particles becomes complex and diversified. Therefore, Maxwellian single-peak distribution cannot reflect particle movement accurately.

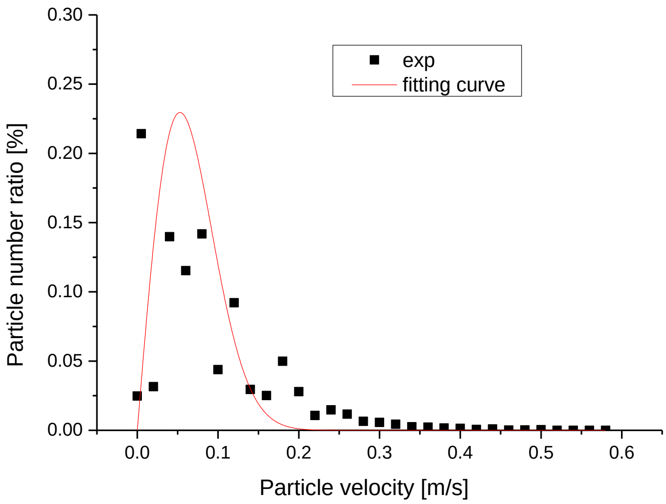

Figure 3.8. Single-peak distribution curves compared with experimental data (U_g= 1.33 m/s)

For the bi-peak model, particle velocity distribution is a linear combination of two Maxwellian forms:

$$f(c) = Bf_{M2}(c) + Cf_{M3}(c) \tag{3.21}$$

Fig. 3.9 shows the bi-peak distribution curves compared with experimental data. The curve using Eq. (12) basically matches the particle velocity distribution curve obtained via measurement. This is because compared with single-peak model, bi-peak model can reflect two kinds of particles which are influenced by two kinds of particle-fluid interaction mechanisms, respectively. In some studies of single bubbles, particles in the bubble phase were neglected (Davidson and Harrison 1963). This is because n_{fd} in Eq. (3.17) is very small compared with n_{pfc} and n_{pd} in the case of a single bubble. In other words, there are two primary particle-fluid interaction mechanisms occurring: PFC and PD. However, it cannot reflect particles which belongs to the fluid dominating (FD) category.

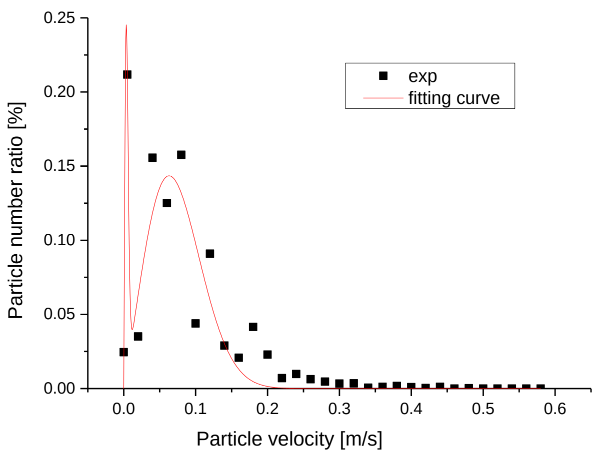

Figure 3.9. Bi-peak distribution curves compared with experimental data (U_g = 1.33 m/s)

According to the experimental data and analysis in Section 3.3, the particle velocity distribution is a linear combination of three Maxwellian forms. The particle velocity distribution bases on the tri-peak model is used to fit the experimental data:

$$f(c) = Af_{M1}(c) + Bf_{M2}(c) + Cf_{M3}(c) \tag{3.22}$$

To highlight the advantage of Eq. (3.14), the estimated distributions for the tri-peak model are presented against the experimental data in Fig 3.10. For the bubbles in different gas velocity, the tri-peak model distribution reflects the real changes in the experimental data correctly.

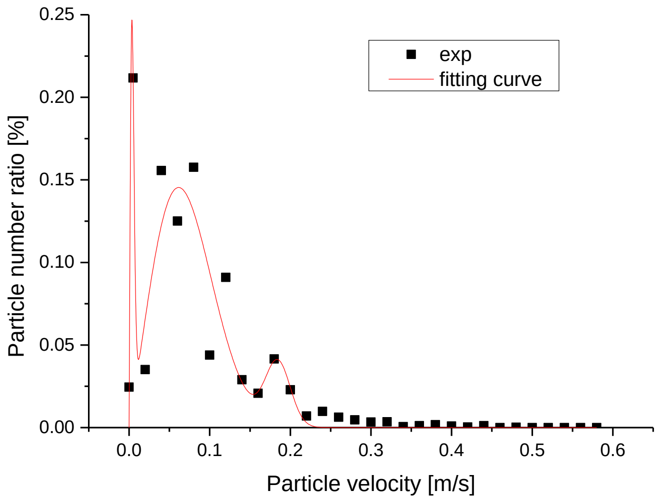

Figure 3.10. Tri-peak distribution curves compared with experimental data (U_g = 1.33 m/s)

To evaluate the strength of the tri-peak model, a statistics method is introduced. The correlation coefficient (R) between the experimental data and fitting curve of all three model was calculated. The correlation coefficient should be located in the range of 0 ~ 1, and R =1 indicates the perfect fit. By this method, the particle velocity distributions and correlation coefficients for the single-peak, bi-peak and tri-peak models are given in Fig3.11, Fig3.12 and Fig3.13, respectively.

Fig. 3.11 shows that the correlation coefficient is low for the single-peak model. Gas velocity will affect the accuracy of single-peak model significantly. The effect of gas velocity on accuracy shows a trend that R increases from U_g=1.22 m/s and reach a highest value at U_g=1.44 m/s, then it decreases at U_g=1.88 m/s. The reason can be found in Fig. 3.5. For the cases of low U_g (1.22 m/s and 1.33 m/s) and high U_g (1.66 m/s and 1.88 m/s), there are at least two peaks which represent PD and PFC particles or PD, PFC and FD particles, respectively. Therefore, although the parameter B in Eq. (3.18) can be adjusted to fit the experimental data, single-peak model is poor at profiling the characterization of real particle velocity distribution. At U_g=1.44 m/s, for the same region, the proportion of PFC particles (the second peak in Fig. 3.7) increases and becomes the dominant factor. Therefore, this case has the highest R in single-peak model.

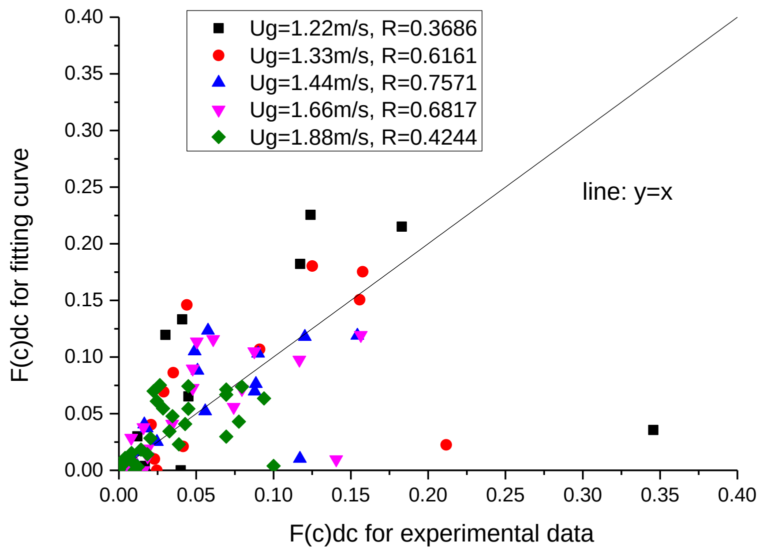

Figure 3.11. Correlation coefficient and F(c)dc for the experimental data and single-peak model

Fig. 3.12 shows the accuracy of the bi-peak model. The correlation coefficients are more than 0.9 at U_g=1.22 m/s, 1.33 m/s and 1.44 m/s which means that compared with the single-peak model, the bi-peak model can profile the particle velocity distribution accurately when particles fall into PD and PFC category. However, the accuracy decreases at high U_g.

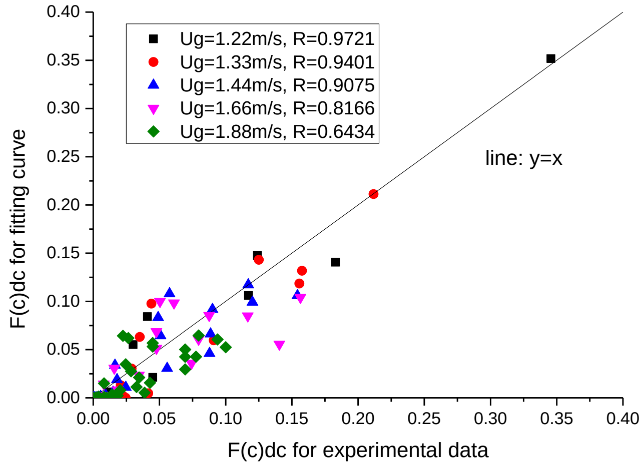

Figure 3.12. Correlation coefficient and F(c)dc for the experimental data and bi-peak model

Fig. 3.13 shows the accuracy of the tri-peak model. The difference between the tri-peak model and bi-peak model is small for the low U_g case. For high U_g case, the trailing vortex effect becomes evident. For the same analysis region, the proportion of FD particles increases. Therefore, the tri-peak model has a better match with the particle velocity distribution curve obtained via experiment.

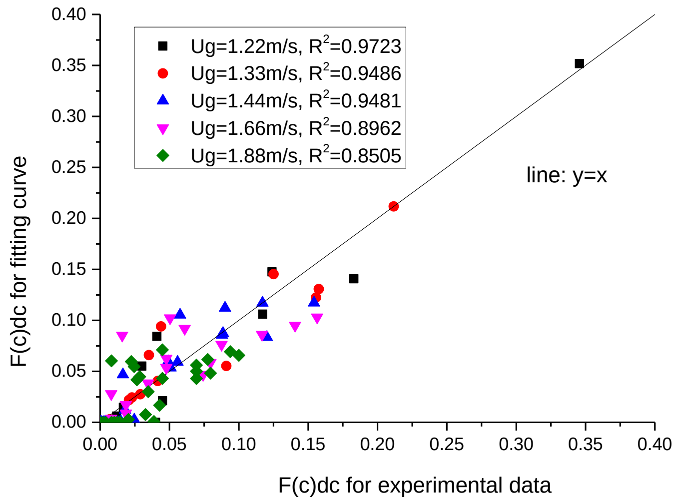

Figure 3.13. Correlation coefficient and F(c)dc for the experimental data and tri-peak model

To sum up, the single-peak model can only reflect one kind of particle motions. It is difficult to profile particle movement in a fluidized bed because there is at least two kinds of particle-fluid interaction mechanisms acting on particles. The bi-peak model can reflect two kinds of particle motions, so it can fit the case when the proportion of FD particles can be neglected. For some complex cases, when there are three kinds of mechanisms acting on particles, the tri-peak model can be used to profile the particle velocity distribution more accurately.

3.4 Further discussion of tri-peak model

In this study, for tri-peak model, Eq. (3.18) is used to fit the experimental distribution curves and the correction factors are showed in Table 3.2.

Table 3.2 Value of correction factors

Factors	a_1	b_1	c_1	a_2	b_2	c_2
Value	0.035-0.047	0.40-0.67	0.0013-0.0086	1.57-3.44	0.12-0.42	0.0001

The results shows that for particles around a single bubble, the relationship of granular temperature and average particle velocity for each peak will be $\theta_{pfc} > \theta_{fd} > \theta_{pd}$ and $u_{fd} > u_{pfc} > u_{pd}$. For PD particles, the granular temperature and average particle velocity are far lower than other two kinds of particles. This is because the movement of PD particles are affected by particle-particle collision and the impact of drag force is limited which results in particles in this domain have low velocity. For PFC particles, the largest value of granular temperature shows the violent velocity fluctuation. This is because the movement of PFC particles are affected by both fluid and particles, and the complex mechanism such as the wake makes particle velocity diversified. For FD particles, the granular temperature is between the PFC and PD particles. Obviously the average particle velocity is larger than other two kinds of particles because of the effect of drag force.

In gas-solid two-phase systems, heterogeneous structures due to the existence of bubbles are difficult to describe accurately and quantitatively. The conventional method describes heterogeneous structure indirectly via porosity, bubble equivalent diameter and other dynamics parameters. In this work, the velocity distribution function is used to describe the heterogeneous structure in terms of single-, bi- and tri-peak models. The results show that the more peaks there are in the distribution function, the more detailed characterization of particle velocity distribution can be obtained. Analysing the velocity distribution function may be a new method to describe heterogeneous structures in gas-solid two-phase systems.

3.5 Conclusions

In this work, the particle velocity distribution for particles around a single bubble was measured, and the data were collected via experimentation and simulation. Three kinds of Maxwellian distribution models are proposed and discussed. The following conclusion can be drawn.

(1) The simulation results by DEM compare relatively well with the experiment. Both results show that particle velocity distribution function does not follow the Maxwellian distribution but is instead a linear superposition of multiple Maxwellian velocity distributions.

(2) Based on various particle-fluid interaction methods, a tri-peak distribution function of bubble-forming particles is derived. Three kinds of models such as tri-peak model, bi-peak model and single-peak model are proposed to fit the

experimental data. The error analysis shows that compared with other models, the tri-peak model can profile particle velocity distribution more accurately.

(3) The value of granular temperature and average particle velocity for each peak was calculated. Based on those value and their physics meaning, the characteristics of particles for each peak were analysed.

This page is intentionally left blank

CHAPTER 4 CFD-DEM MODELLING OF MIXING OF GRANULAR MATERIALS IN MULTIPLE JETS FLUIDIZED BEDS

4.1 Introduction

Jetting fluidized beds are widely used in industries as they can offer high quality contacts between particles. Fluidized beds with different jet numbers are designed to satisfy industrial needs. For example, fluidized beds with one jet, also called spout-fluidized beds, are popular and utilized in a variety of industrial applications, including drying and coating equipment, catalytic reactors and gasification of coal and biomass (Zhang et al., 2009a). Multiple jetting fluidized beds are also employed in industries for good mixing and improved chemical reaction properties (Deb and Tafti, 2014). In the past, extensive studies have been done in jetting fluidized beds experimentally or mathematically, aiming for better understanding of the system and its design and control.

The designing of jets or distributors will significant impact the characteristics and quality of fluidization (Geldart and Baeyens, 1985). Many studies have been performed to investigate distributor design in the past. For example, Walker et al.(1975) measured the difference between porous plate and sieve plate distributors in a bubbling fluidized bed, and the results suggest that distributor type impacts initial bubble size. Saxena et al.(1979) studied two bubble cap distributors of different geometries and four Johnson screen distributors, and found that the bed expansion ratio increases with increasing excess fluidization velocity and distributor pressure drop but decreases with bed height. By using two types of multi-orifice distributors, Sathiyamoorthy et al.(2003) analyzed the bed pressure drop ratio and the operating velocity for achieving uniform fluidization. An equation is suggested by Qureshi et al.(1979) which relating the minimum value of the ratio of the distributor pressure drop for stable operation and the bed pressure drop to the aspect ratio of the bed. This equation could be used for design purposes. Most of distributor studies focus on the size and velocity of bubbles (Walker, 1975, Maurer et al., 2016), bed dynamics (Sanchez-Delgado et al., 2019) and the operating parameters (Qureshi and Creasy, 1979, Sathiyamoorthy and Horio, 2003). The studies on the mixing behavior for different distributor are still limited.

The early attempts for mixing behavior can be traced back to the introduction of Lacey mixing index by Lacey (1954) to investigate particle mixing in 1954. The earlier studies for mixing and segregation in binary systems were summarized by Rowe and Nienow (1976). They introduced the terms of flotsam and jetsam to describe segregated solids in fluidized beds (Rowe et al., 1972). Experimentally, Yang et al. (2007) used high speed motion and force probe to investigate the bubble characteristics. Ettehadieh et al. (2016) found that the solid circulation rate increases linearly with increasing jet velocities in a large jetting fluidized bed. Zhang et al.(Jin et al., 2009, Zhang et al., 2009b, 2009a) used a flashboard-box to take samples from the dense-phase area of a spout-fluid bed. Particle image velocimetry (PIV)(Willert and Gharib, 1991) was also used in particle tracking in fluidized beds. Bokkers et al

(2004) applied PIV to a dense gas-solid fluidized bed to measure the particle velocities in the vicinity of a single bubble injected in a fluidized bed. Note that experimental measurements such as PIV can characterize the jet fluidized beds and provide reliable data for analysis, but it is generally difficult to obtain detailed microscopic and macroscopic properties (Deb and Tafti 2014). This can be easily overcome by numerical approaches.

Generally, there are two methods to describe a gas-solid two phase system: the two-fluid model (TFM) and the combined CFD and discrete element model (DEM). For TFM, the gas and particles are considered as interpenetrating continua and the computational fluid dynamics techniques are used to solve conservation equations (Rangarajan et al. 2013). For CFD-DEM, particles are treated as discrete entities. CFD-DEM simulations can provide dynamic information, for example, the trajectories and velocity of individual particles which is difficult to obtain by experimental method (Zhu et al., 2007). Recent advances and applications of this approach were summarized by Zhong et al. (2016), but most of studies focused on a single jet spouted bed. For example, Zhang et al. (2002) used CFD-DEM to simulate a 2D spouted bed with a single central jet. They found that the jet penetration height increases with jet gas flow rate and nozzle diameter. Boemer et al. (1997) used TFM to simulate bubble formation of one jet in a 2D fluidized bed. Two- and three-dimensional CFD-DEM modeling of fluidized beds were compared by Deb and

Tafti (2014). A 9-jet fluidized beds were studied and the complex jet interaction and solid circulation patterns were discussed. Their results show that 2D simulation can be used to capture essential jetting trends near the distributor plate regions. But for freeboard region, 3D simulation needs to be used to capture bubbles.

The basic mechanism of solids mixing in bubbling fluidized bed is known to be related to bubbles. Rowe et al. (1965) believed that there are three dominant physical processes that cause mixing include vortices, drift and return flow. Although their study was demonstrated fifty years ago, the conclusion are still referred in some recent studies (Sanchez-Prieto et al., 2017, Eames et al., 2005). Except for bubbles, mixing is also affected by some other variables such as jets velocity, particle properties and bed parameters. Wu et al. (1998) presents a detailed study of the effect of gas velocity on the mixing behavior. They found that segregation is most significant at gas flow rate between the minimum fluidization velocities of flotsam and jetsam particles. Jin et al.(2009) Investigated the effect of jet velocity and particle density in a spout-fluidized bed. Their results show that the rate of mixing are significantly affected by particle density and heavier particles achieve a higher mixing rate but a poorer mixing quality. Therefore, to reach the same mixing index, the gas velocity needs to increase with the increase of particle density. The effect of bed aspect ratio (bed height/diameter) was discussed by Formisani et al.(2001). They found that the segregation is more pronounced for a bed with low aspect ratio. In addition, some other studies focused on the jet penetration height (Hong et al., 2003, Vaccaro et al.,1997b, Wang et al., 2017).

Clearly, most studies on particle mixing and segregation are based on single jet fluidized bed. Comparative study of beds with different jet numbers still has not been investigated extensively. In this study, CFD-DEM approach is used to simulate a fluidized bed with different jet numbers. Based on the same gas flow rate, cases with different jet numbers are compared in terms of the maximum bed pressure drop, bed height, and mixing index. The computational results are also compared with the experimental results.

4.2 Model description

4.2.1 Experimental setup

A schematic diagram of the experimental setup is given in Fig.4.1. The system consists of a supply gas system, the main body (fluidized bed) and a data acquisition system. Fluidized gas is supplied by a compressor and controlled by a mass flow valve. The gas distributor is made of a 5-mm-thick sintered plate. The sintered plate is made by a special manufacturing process and has a 20-μm aperture, which can ensure that gas that enters the fluidized bed is relatively evenly distributed. The fluidized bed has a cross-section of 110×40 mm and a height of 1000 mm. The measuring system includes a gas flow gauge, pressure sensor and computer. The bed pressure drop is measured by two pressure taps located at the bottom and top of the bed. The signals are sent to the pressure sensor and then displayed on the computer.

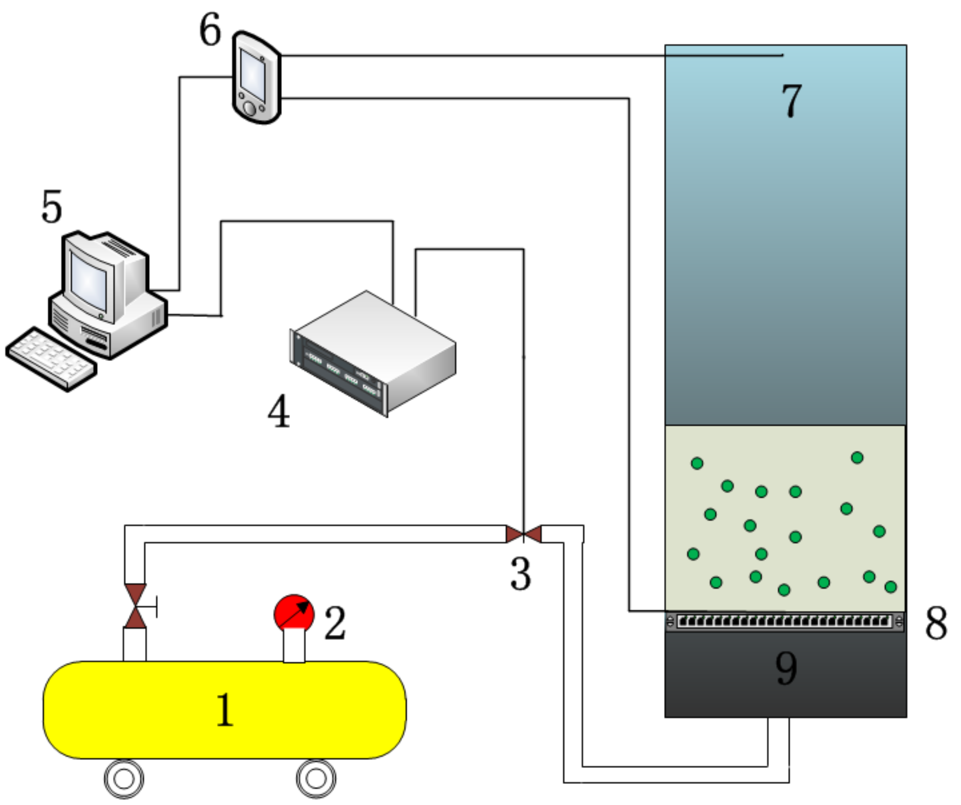

Figure 4.1 Schematic diagram of the experimental setup: (1) compressor, (2) pressure gauge, (3) control valve, (4) gas flow gauge, (5) computer, (6) pressure sensor, (7) fluidized bed body, (8) gas distributor, (9) fluidized gas chamber.

4.2.2. CFD-DEM model

Table 4.1. Summary of the main equations for the discrete phase modeling

Gas phase

$$\frac{\partial(\varepsilon\rho_g)}{\partial t} + (\nabla \cdot \varepsilon\rho_g u) = 0$$

$$\frac{\partial(\varepsilon\rho_g u)}{\partial t} + (\nabla \cdot \varepsilon\rho_g uu) = -\varepsilon\nabla p - S_p - \nabla \cdot (\varepsilon\bar{\tau}) + \varepsilon\rho_g g$$

Source term

$$S_p = \frac{1}{V}\int\sum_{a=0}^{N_p} F_{dra,a}\delta(r-r_a)dV$$

Particle phase

$$m_a \frac{d^2 r_a}{dt^2} = F_{cont,a} + F_{dra,a} - V_a\nabla p + m_a g$$

Particle torque

$$I_a \frac{d^2\Theta_a}{dt^2} = T_a$$

Contact force

$$F_{cont,a} = \sum_{contactlist}(F_{ab,n} + F_{ab,t})$$

$$F_{ab,n} = -k_n\delta_n n_{ab} - \eta_n v_{ab,n}$$

$$F_{ab,t} = \begin{cases} -k_t\delta_t - \eta_t\upsilon_{ab,t},\ for|F_{ab,t}| \le \mu_f |F_{ab,n}| \\ -\mu_f |F_{ab,n}| t_{ab},\ for|F_{ab,t}| > \mu_f\ |F_{ab,n}| \end{cases}$$

Gas-Solid interaction

Drag force model

$$F_{dra,a} = 3\pi\mu_g\varepsilon^2 d_p(\vec{u} - \vec{\upsilon}_a) f(\varepsilon)$$

$$f(\varepsilon) = \begin{cases} \frac{150(1-\varepsilon)}{18\varepsilon^3} + \frac{1.75}{18}\frac{Re_p}{\varepsilon^3}, \varepsilon < 0.8 \\ \frac{C_d}{24} Re_p \varepsilon^{-4.65}, \varepsilon \ge 0.8 \end{cases}$$

$$C_d = \frac{24}{\mathrm{Re}_p}(1 + \frac{3}{16}\mathrm{Re}_p)$$

The governing equations for the CFD-DEM are listed in Table 4.1. For the ga s phase, the gas flow is described by the volume-averaged Navier-Stokes equati on. For the particle phase, Newton's second law is used to calculate the accele ration and then the velocity and position of each particle. The contact force $\mathbf{F}_{cont,a}$ includes both the normal $\mathbf{F}_{ab,n}$ and tangential $\mathbf{F}_{ab,t}$ component. In this r esearch, the linear-spring/dashpot soft-sphere model (Cundall and Strack 1979) i s used to calculate the contact force. The traditional drag model, which is a c ombination of the Ergun equation for the dense regime and the Wen-Yu correl ation for the dilute regime, is used in this work (Ergun and Orning 1949, We n and Yu 1966). Here, the particle Reynolds number is defined as $Re_p = \frac{\varepsilon d_p(u-v)\rho_g}{\mu_g}$, where ε is the void fraction, d_p is the diameter of the particle, and μ_g is the dynamic viscosity. The drag coefficient $C_d = \frac{24}{Re_p}(1+\frac{3}{16}Re_p)$ follow s Oseen (Oseen 1911). No slip boundary condition is imposed on the fluid at the sidewalls (Ye, Hoef, and Kuipers 2005a), the fluid phase influx cell (gas i nlet boundary) is set at the bottom of the bed, and the prescribed cell (pressur e outlet boundary) is set at the top of the bed. Fig. 4.2 shows the jet configur ation for different cases. The size of each jets are 100 mm ×100 mm and the gap between two adjacent jets is 100 mm. Gas is injected through jets in the presence of a background fluidization gas flow at a minimum fluidization vel ocity.

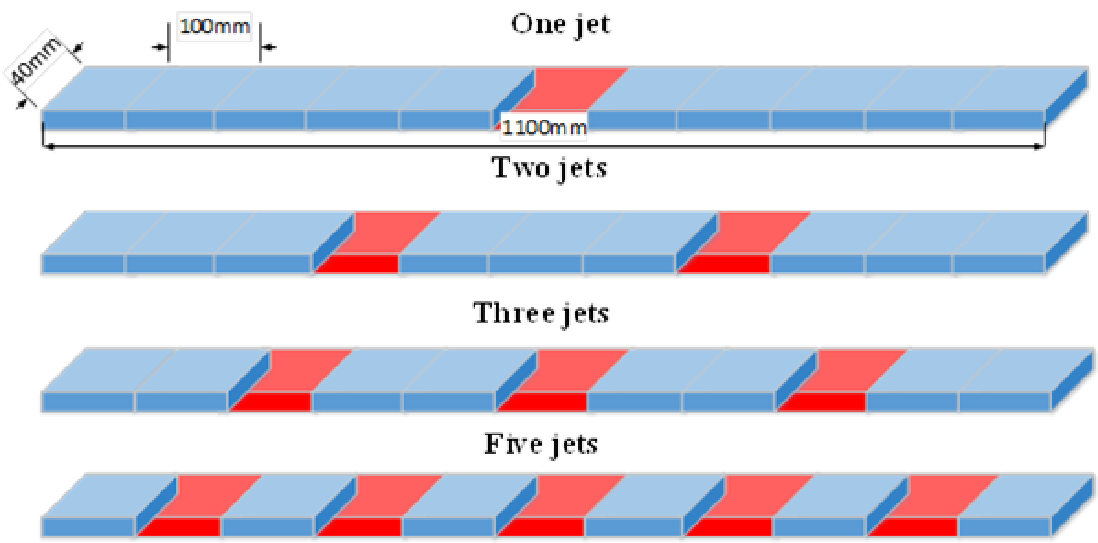

Figure 4.2 Jet configurations at the bottom gas distributor for the simulation cases

Table 4.2. Simulation parameters

Parameter	Value	Unit
Gas temperature, T	293	(K)
Shear viscosity of gas, μ_g	1.8×10^{-5}	(Pas)
Molar mass of gas, M	2.9×10^{-2}	(kg/mol)
Number of particles, N_p	30000	(-)
Diameter of particle, d	2.5×10^{-3}	(m)
Density of particle, ρ_s	130	(kg/m3)
Bed width, W	1.1×10^{-1}	(m)
Bed depth, D	4.0×10^{-2}	(m)
Bed height, H	1.0	(m)
Minimum fluidization velocity, U_{mf}	0.44	(m/s)
Normal restitution coefficient, e_n	0.97	(-)
Normal restitution coefficient wall, $e_{n,w}$	0.97	(-)
Tangential restitution coefficient, e_t	0.33	(-)
Tangential restitution coefficient, $e_{t,w}$	0.33	(-)
Friction coefficient, μ	0.1	(-)
Time step, Δt	1.0×10^{-5}	(s)
Time step for data save, Δt_s	1.0×10^{-3}	(s)

The simulation parameters are listed in Table 4.2. The bed size, gas and particles characteristics follow the experiments. Vitrified hollow small particles with a diameter of 2.5 mm and a density of 130 kg/m^3 are used in both experiments and simulations. The minimum fluidization velocity of this particle is 0.44 m/s according to our experiment. The initial bed height was 100 mm, which is also in compliance with the experiment. The grid size for gas flow is $10 \times 10 \times 10$mm.

Table 4.3. Case parameters

Case	Gas superfical velocity for each jet (m/s)				
	One	Two	Three	Five	Uniform
C1(1.703×10^{-3} kg/s)	3	1.5	1	0.6	0.2727
C2(2.554×10^{-3} kg/s)	4.5	2.25	1.5	0.9	0.4091
C3(3.406×10^{-3} kg/s)	6	3	2	1.2	0.5455
C4(5.108×10^{-3} kg/s)	9	4.5	3	1.8	0.8182

Table 4.3 lists the cases used. In this study, four jet gas flow rates (C1 to C4) were set: 1.703×10^{-3} kg/s, 2.554×10^{-3} kg/s, 3.406×10^{-3} kg/s and 5.108×10^{-3} kg/s. For each case, the gas flow rate is constant, but jet numbers varies. Correspondingly, the gas superficial velocities change with the jet number. Beds with one jet has the highest gas superficial velocity, and lowest under the uniform gas conditions.

4.2.3. Particle mixing index

To analyze the mixing, particles were marked with two different colors at the beginning of the simulation. The concentration of one component in the sampling grid is calculated by $C_i=n_i/n_t$ where n_i and n_t are the number of the tracer particles i in each sample grid and the total number of particles contained in the sample grid, respectively.

The mixing index was used to discuss the particle mixing behavior in the fluidized bed (Fan, Chen, and Watson 1970). In this study, the well-known Lacey mixing index (Lacey 2010) was used to evaluate the mixing degree:

$$M_l = \frac{\sigma_0^2 - \sigma^2}{\sigma_0^2 - \sigma_m^2} \tag{4.1}$$

where σ^2 is the variance and calculated by $\sigma^2 = \sum_{i=1}^{n} \frac{(C_i - \overline{C})^2}{n-1}$. σ_0^2 = q(1-q) and σ_m^2 = q(1-q)/p are the variances of the fully segregated and fully mixed states, respectively. q is the total proportion of either type of particles in the mixture. p is the average number of particles in a simple grid. Lacey mixing index can be used to define two extreme mixing states: fully segregated (*M* = 0) and fully mixed (*M* = 1) (Halidan et al. 2016). The actual mixing index varies from 0 to 1. In this study, particles are marked as totally segregated at the beginning of the simulation.

4.3 Results and discussion

4.3.1 Model validation

The results simulated can be affected by many factors such as the particle-wall contact (Hu et al. 2017), grid size (Wang, van der Hoef, and Kuipers 2010), drag model (Mikhailov and Freire 2013), boundary conditions (Zhong et al. 2016) and DEM parameters (Zhou and Fan 2015a). In this work, an experimental system as shown in Fig. 4.1 was built to validate the CFD-DEM model. Details for setup of experiment and simulation was shown in section 2. Uniform gas inlet condition was used in both experiment and simulation. The range of gas velocity is 0-1m/s which cover all value of gas flow rate this work will use. The grid size is 10mm(width) × 10mm (height) × 10mm (depth). The comparison was made via the relation of pressure drop vs gas superficial velocity (Fig. 4.3), general flow patterns (Fig. 4.4) and particle velocity distribution(Fig. 4.5).

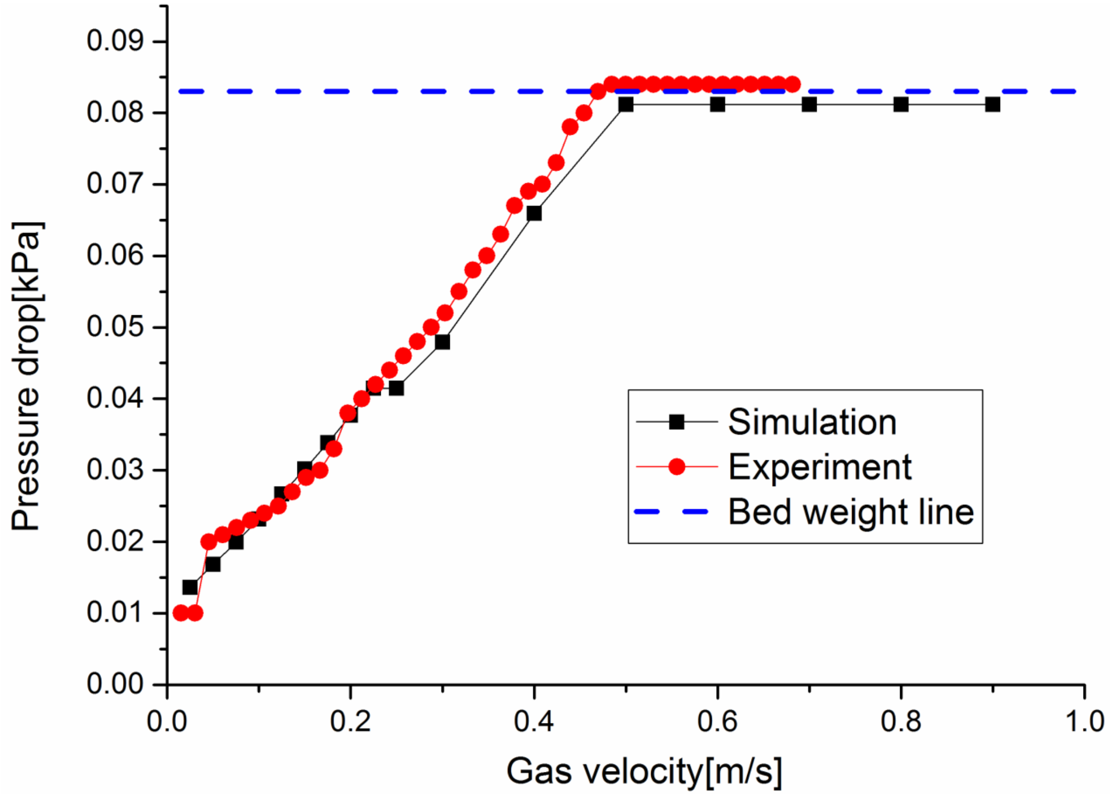

Figure 4.3. Pressure drop curve – the relationship between pressure drop and gas superficial velocity for the case with uniform gas flow.

Fig. 4.3 shows the pressure drop curve for both experiment and simulation. The same experiment perform was conducted by 3 times and the error range is less than 1%. The pressure drop is increased with the increasing of gas superficial velocity when particles are not fluidized at the beginning. Then the pressure drop reaches a steady state after the minimum fluidized velocities. The results simulated are in agreement with the experimental results. Furthermore, the minimum fluidization velocity V_{mf} = 0.44 m/s was obtained by experiment and used in subsequent simulations. Fig. 4.4 shows snapshots of the instantaneous bed profile from the experiment and simulation. The bed expansion can be found in both experiment and simulation. The particle behaviors are visible in both the experiment and simulation when bubbles rise through the fluidized bed. The experimental snapshot shows that particles around bubbles move faster than other area, the same trend can also be found in the discussion of simulated results. Particle image velocimetry (PIV) system is also employed to measure the particle velocity distribution for the particles around bubbles and support simulation model.

(a)

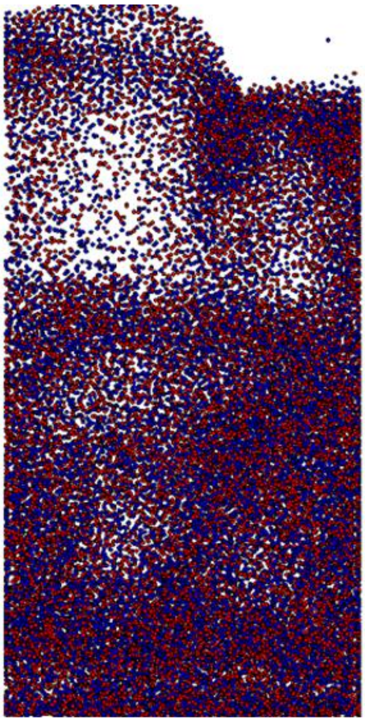

(b)

Figure 4.4. Instantaneous bed characteristics for uniform gas inlet conditions (a) experimental result, (b) simulation result

4.3.2 Macroscopic analysis

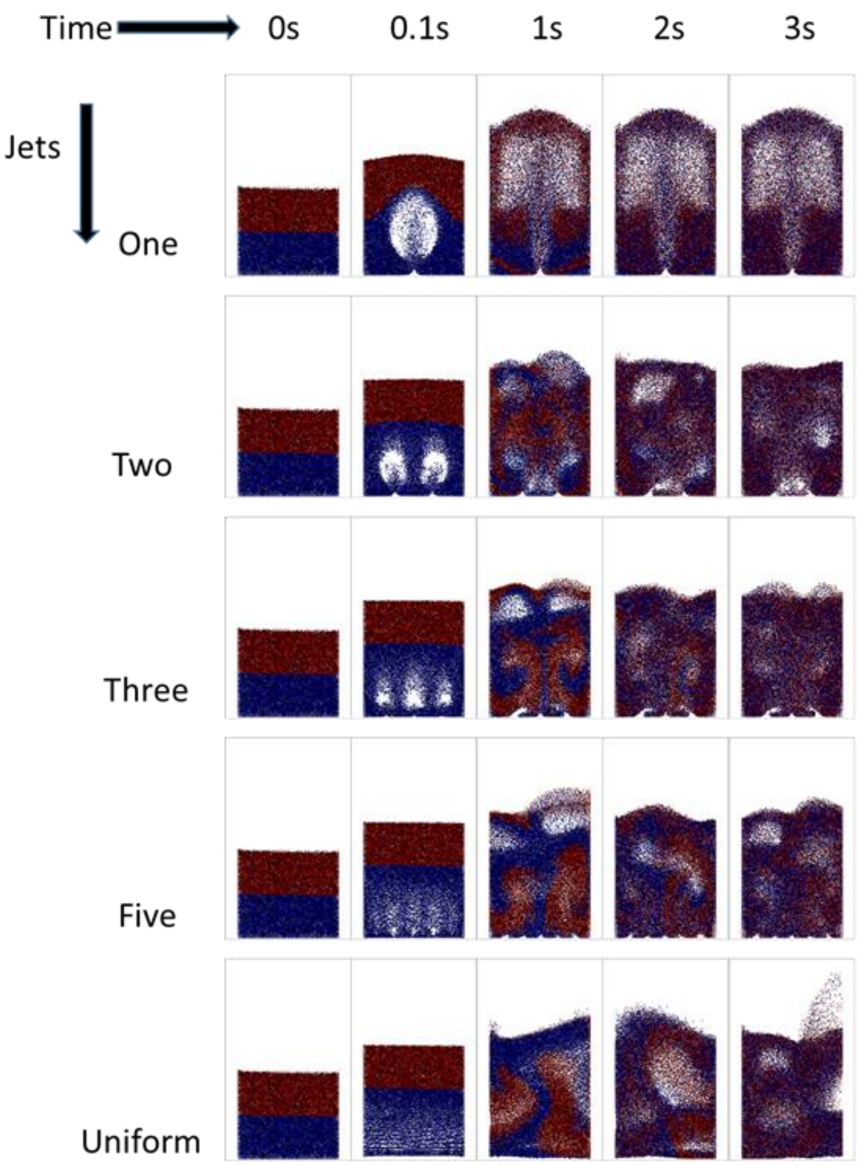

Figure 4.5. Instantaneous bed characteristics for simulation C3 with gas flow rate of 3.406×10^{-3}kg/s. (a) One-jet case, (b) Two-jets case, (c) Three-jets case, (d) Five-jets case, (e) Uniform gas inlet case.

Fig. 4.5 shows the evolution of the fluidization process for simulation C3 with different jet numbers. Particles in the bottom and top layer are marked with different colors at the beginning of the simulation, which provides a visualization of particle mixing behaviors. With a high jet velocity in the one-jet case, a single bubble is formed at 0.1 s and is replaced by a jet flow at 1 s. Particles are lifted from the bottom to the top by a jet flow and form an “umbrella” region. This typical spouted bed features can be found in many studies (for example, Jin et al. (Jin et al. 2009)). Their study shows that bed expansion is observed as soon as the spouting gas is injected and particles begins to circulate.

When the number of jets is increased, the jet velocities are decreased, as shown in Table 4.3. For the two-jets case, two bubbles are formed at the beginning and the shape of bubbles is impacted by the particles falling from the center and both sides of the bed at 1s. In the end, the gas from two jets combines together and the flow pattern gradually reaches a stable state. For three and five jets cases, particles on the top layer fall from both sides of the bed and rise along with the gas injected from each jets. The trailing vortex contributes to the large extent of mixing (Le Lee and Lim 2017). For uniform gas inlet case, the flow pattern is hard to reach a quasi-steady state all the time.

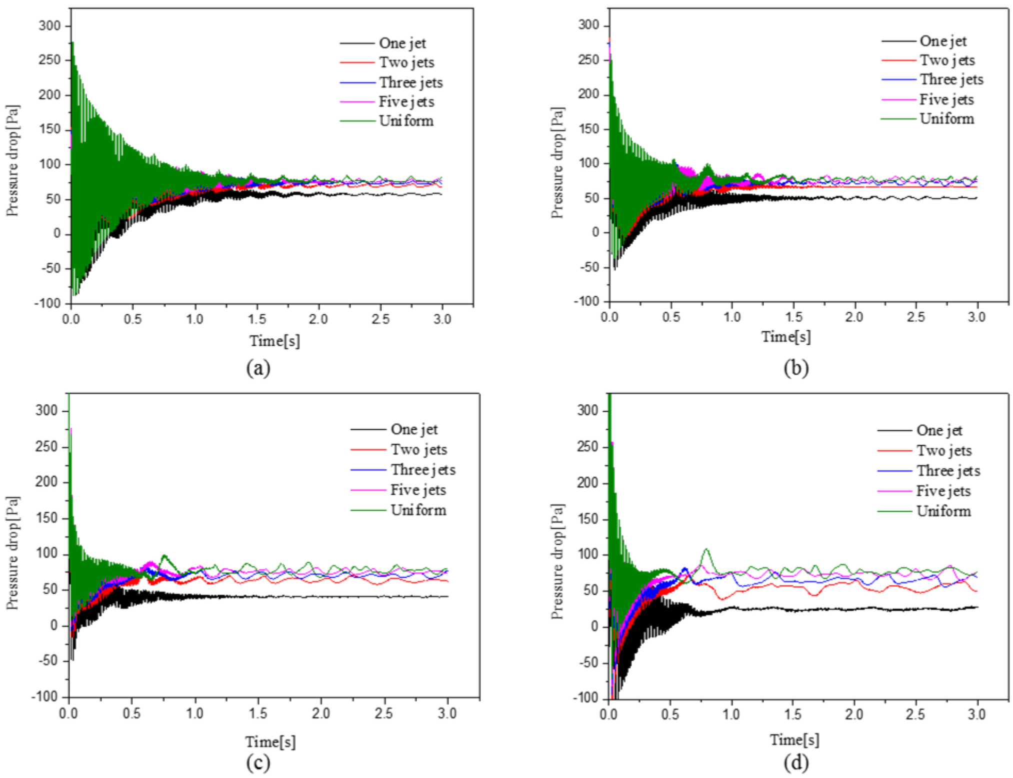

Figure 4.6. Pressure drop as a function of time for different simulation: (a) Case 1, (b) Case 2, (c) Case 3 and (d) Case 4.

Macroscopic parameters such as the maximum bed pressure drop, bed height and mixing index can be used to characterize fluidized beds. These parameters can reflect the mixing characteristics in fluidization, and provide important information for designing and operating a fluidized bed. Fig. 4.6 shows the bed pressure drop as a function of time for each case. The pressure drop fluctuates wildly at the beginning and the amplitude decreases with time. For C1 with gas flow rate of 1.703×10^{-3}kg/s, the bed spends 2.1s to reach a steady state and the time decreases with the increasing of gas flow rate in other cases.

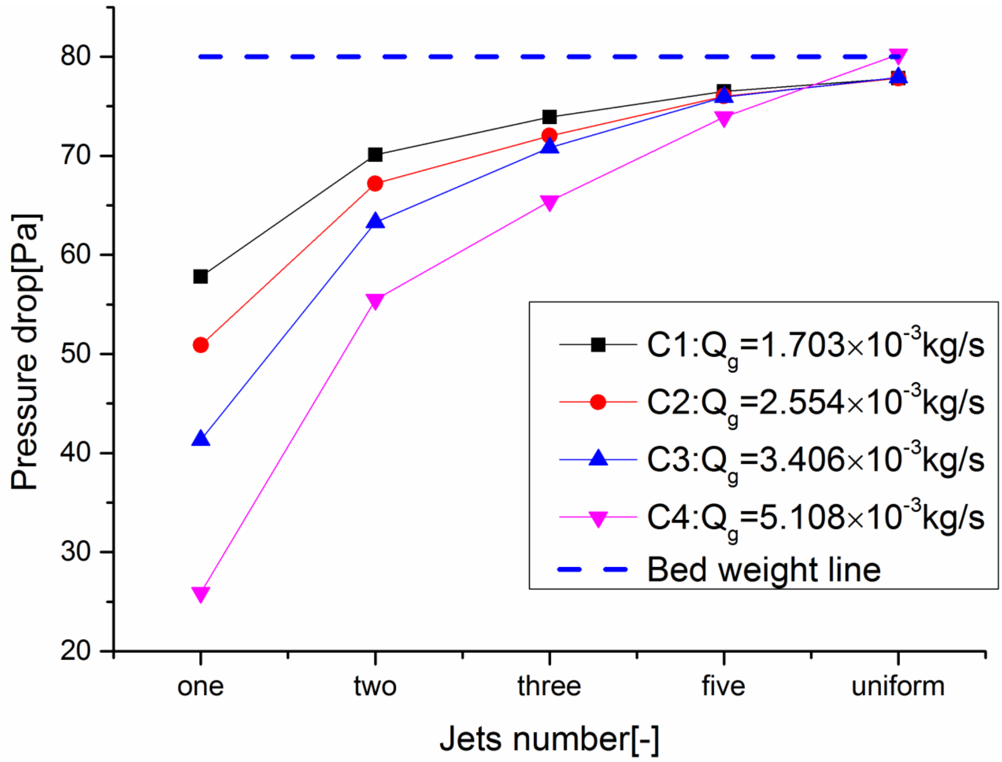

Figure 4.7. Maximum bed pressure drop for different simulation cases (C1, C2, C3, and C4).

Note that theoretically, the maximum bed pressure drop should be fixed, independent of the gas flow rate when the fluidized bed reaches complete fluidization. The maximum bed pressure for uniform gas inlet cases reflects the bed weight as shown in Fig. 4.3 and Fig. 4.7. However, the results from Fig. 4.6 show that the value of maximum bed pressure drop also depends on the jets number. Therefore, based on the averaged maximum bed pressure drop from Fig. 4.6, Fig. 4.7 shows the impact of jets number on maximum bed pressure drop. It can be observed that for the one- or two-jet cases, the maximum bed pressure drop decreases with increasing gas flow rate, which is consistent with that reported by Altzibar et al. (Altzibar et al. 2013b, 2013a). This can be explained in terms of the flow patterns shown in Fig. 4.5. The single jet fluidized bed shows the characteristic of a spout fluidized bed. Bed particles are divided into two regions: the dense phase in the bottom and the dilute phase above. The value of bed pressure drop mainly depends on the size of the dense phase. With gas flow rate increasing, the dense phase region becomes smaller in the single jet case, and correspondingly, the bed pressure drop decreases. This trend becomes less obvious with the increase of the number of jets.

Fig. 4.7 also shows that the pressure drop increases with increasing jets number for each case of C1 to C4. Note that under the condition of the same gas flow rate, the increased jet number means decreased jet gas superficial velocities. The flow patterns tend to be uniform bubbling fluidized bed compared with spout fluidized bed as shown in Fig. 4.5. The dense phase region increases, and more particles become fluidized and moves vigorously. This significantly increases the momentum exchanges between gas and particles, resulting in the increase of the pressure drop.

4.3.3 Bed height

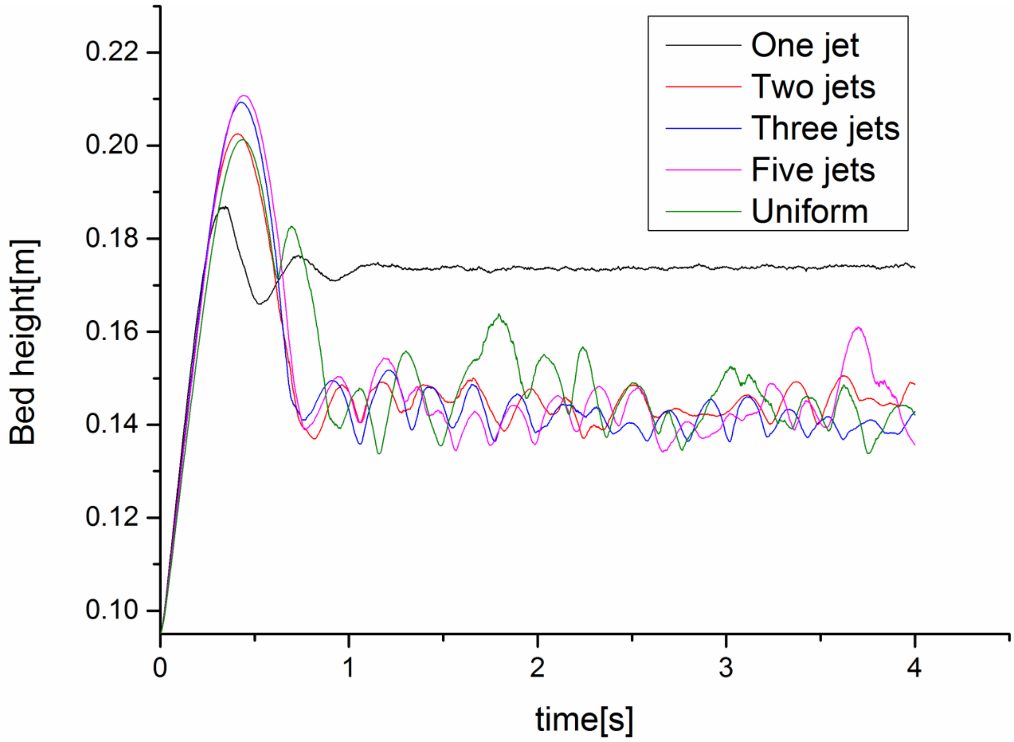

Figure 4.8. Variation of the bed height with time for Case 3 when gas flow rate is 3.406×10^{-3} kg/s.

Fig. 4.8 shows the variation of the bed expansion with time for Case 3 when gas flow rate is 3.406×10^{-3} kg/s. All other cases show the similar trend hence not shown here. It can be observed that each case has a highest peak at the beginning of the fluidization. After the fluidization is stabilized, the bed height in the one-jet case remains unchanged because of the relatively stable "umbrella" region. Furthermore, the bed height is approximately 0.5 times higher than other cases due to the highest jet superficial velocity. For the cases of two, three, five jets and uniform gas inlet, the curves show that the fluctuation is cyclical. The reason is that bubbles will form in those cases and the fluid pattern is relatively stabilized. When a bubble breaks on the top of the bed, it will change the bed height cyclically. Jets number does not affect the height much because none of those cases can form a strong gas flow like one jet case and bring particles out of the bed surface.

4.3.4 Particle velocity distribution

The particle velocities are analyzed in this section for further understanding of the effect of jet numbers on gas-solid flow in jet fluidized beds. Here, the particle velocities in the horizontal (V_x) and the vertical (V_z) directions are examined. Note that particle velocities are time-averaged values after beds reach the steady state. The simulation results from C1, C2 and C3 show the same trend in different jet numbers. For C4, the flow pattern shows the characteristic of turbulent fluidized bed, presenting a more complex structure due to the bubbling, slug flow and fast fluidization flow regimes(Vaccaro, Musmarra, and Petrecca 1997a). Therefore, only C1 (Q_g = 1.703×10^{-3}kg/s) is analyzed here as representative.

4.3.4.1 Radial distribution of the particle vertical velocity V_z

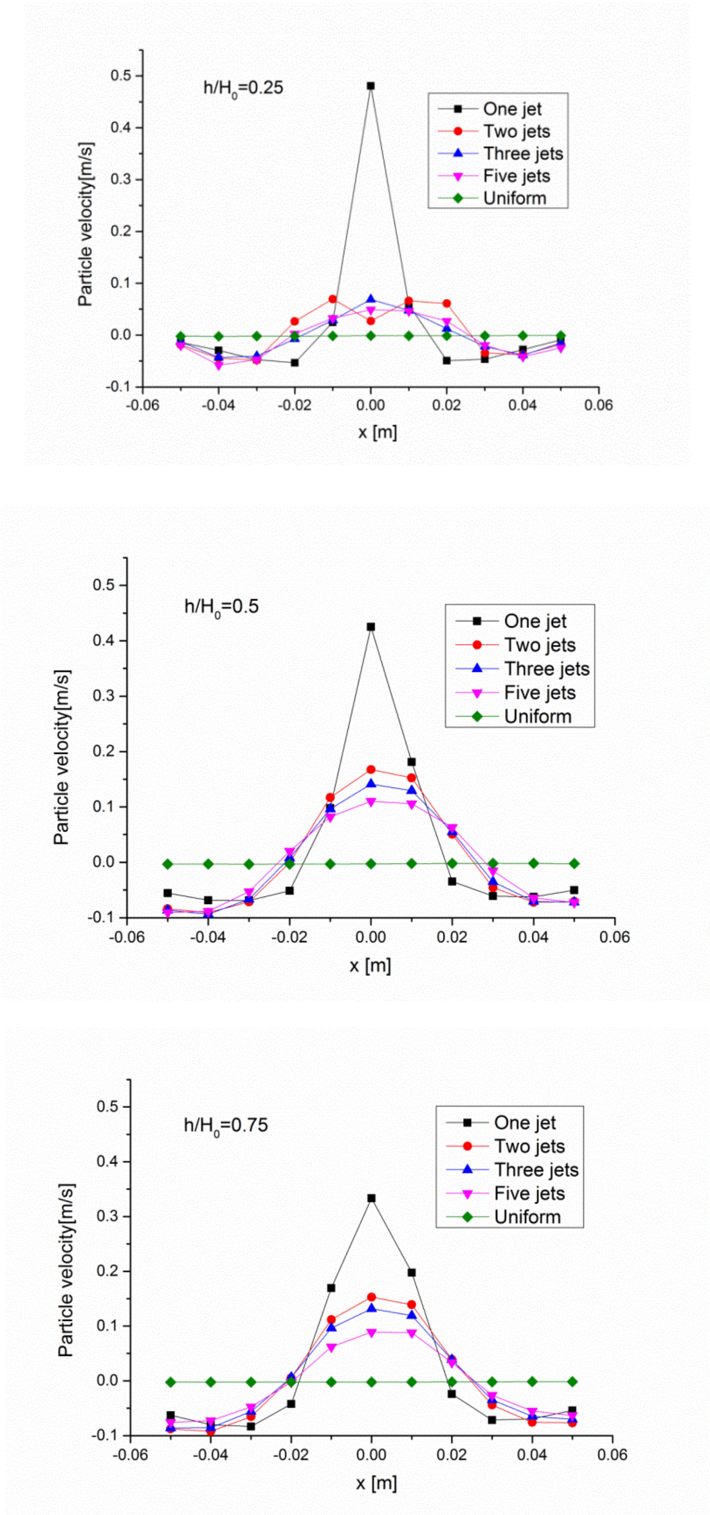

Figure 4.9. Radial distribution of the particle vertical velocity Vz at different bed heights (C1): (a)h/H_0=0.25, (b) h/H_0=0.5, and (c) h/H_0=0.75.

Fig.4.9 shows the radial distribution for V_z at different bed heights. Average velocity of particles in each sampling bin ($10 \times 40 \times 10$mm) is calculated in this study: $\overline{V_i} = \frac{1}{n_i}\sum_{j=1}^{n_i} V_j$ (n_i and V_j is particle number and particle velocity in sampling bin i). Here, H_0 is the height of the initial fixed bed. It can be observed that the fluid pattern for a single jet, multiple jets and uniform gas inlet condition are totally different from one another. For the one-jet condition, the particle velocity distribution shows a typical characteristics of a spout bed. The spouted fluidizing zone particles move upward in the center of the bed, and the velocity decreases with increasing bed height as shown in Fig.4.9. The negative value of velocity in both side of bed shows that particles move downward along the wall, and the velocity increases with bed height increasing.

For the two-jet condition, the curve shows a two peak distribution in the bottom of the bed (h/H_0 = 0.25) (Fig.4.10(a)). Each peak corresponds to one of the jets. With increasing bed height, the two jets merge and one single peak is observed. However, at the high height of h/H_0 = 0.5 and h/H_0 = 0.75 (Figs.4.10(b) and (c)), even when the gases combine together, the particle velocity is still lower compared with the one-jet condition in the center of the bed. Vaccaro et al. (Vaccaro, Musmarra, and Petrecca 1997a) discussed the dispersion of jet momentum in multiple jets fluidized bed. They found that the jet penetration length can be related to the complete dispersion of the jet momentum. In this work, for multiple jets cases, gas flow from different jets may impact with each other because of their close distance, and the momentum of gas flow will dissipate accordingly. The same trend can also be found in the three and five jets conditions. In addition, the lower particle velocity in the center for three and five jets cases shows that the distribution is more uniform with jets number increasing. However, particle velocity is not affected much by the number of jets for the particle near the wall. This is because particles in the center are mainly affected by gas flow rate. Therefore, the velocity of those particles will be changed with jets number changing. The velocity of particles near the wall have little effect by jets number.

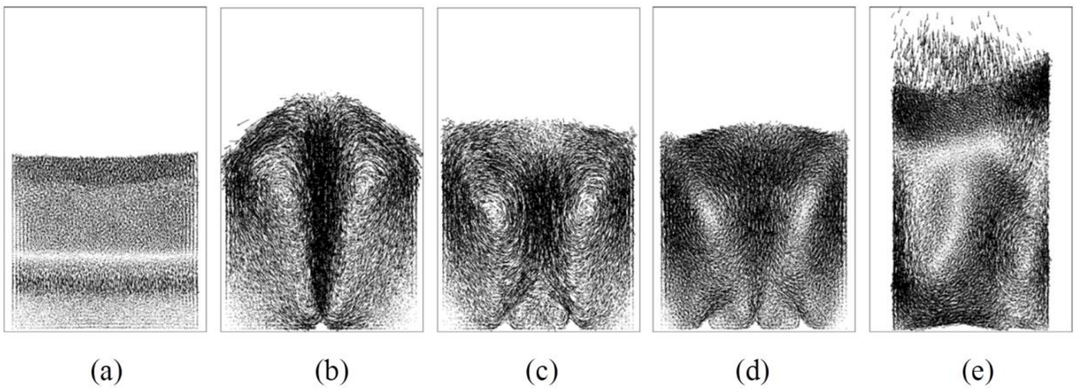

Figure 4.10. Particle velocity vector for simulation cases: (a) C1 - uniform (b) C2-one jet (c) C2-two jets (d) C2-three jets (e) C4-uniform

Fig.4.10 further shows the transient particle velocity field at the steady state. The value of particle velocity is represented by arrows. For the uniform gas inlet condition, the particle velocity distribution is uniform, and there is no difference between the different layers. The value of V_z approximates zero as shown in the figure. This is because the gas superfical velocity for each jet is 0.2727m/s(C1-uniform), particles can not be fluidized and bubbles also do not form in this case. Particles fall when the gap forms by gas. The flow pattern for this case is showed in Fig.4.10(a).

4.3.4.2 Axial distribution for the particle velocity in the x-direction (V_x)

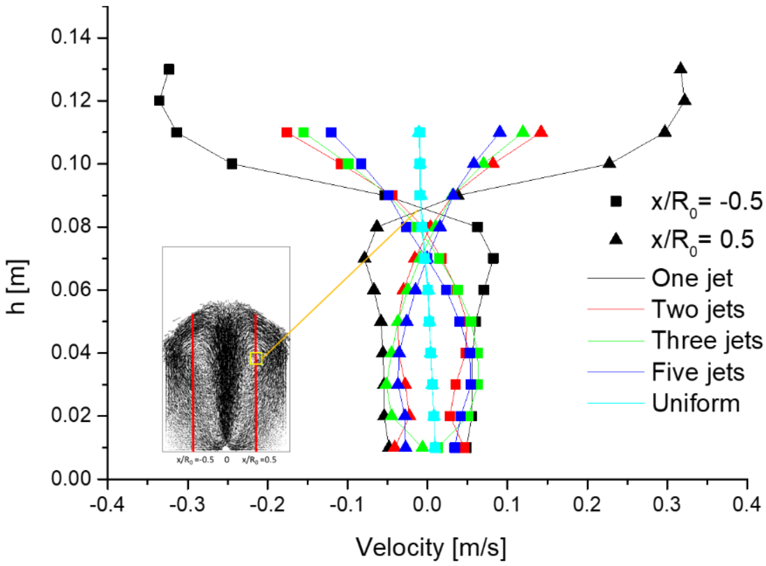

Figure 4.11. Axial distribution for V_x along the bed height (Case 1)

Fig.4.11 shows the axial distribution for the horizontal velocity V_x along the bed height. The results for x/R_0 = -0.5 and x/R_0 = 0.5 are shown. For the one-jet condition, the largest V_x is at the upper part of the bed. Then, the value of V_x drops rapidly with a decrease in the bed height and changes its direction, as marked in Fig.4.11. The same trend can also be found in the two, three and five jet condition cases. However, the value of V_x decreases with increasing jets number. For the uniform gas inlet condition, the vortex is not formed, and the value of V_x approximates zero. Furthermore, the height where V_x is zero also reflects the location of the vortex center.

As shown in Fig.4.11, the height of the vortex center decreases with increasing number of jets.

4.3.5 Mixing index

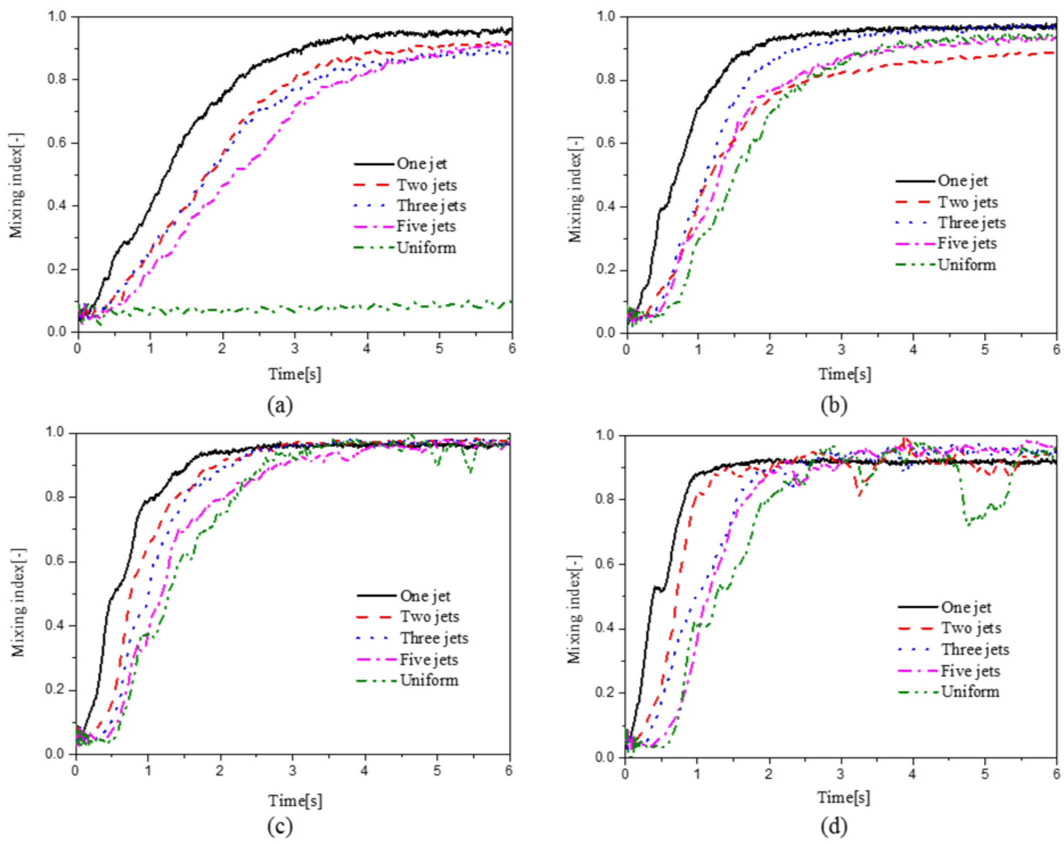

Figure 4.12. Mixing index for simulation cases: (a) C1 , (b) C2 , (c) C3 , and (d) C4 .

Mixing index is one parameter to quantify the degree of mixing in particulate systems. From the practical point of view, mixing rate could play an important role when fluidized beds are used as fluid bed reactors or heat exchangers for temperature control. For example, mixing rate can affect the conversion ratio for some chemical process in fluidized bed. Therefore, mixing rate should be considered for the design of industry fluidized bed such as biomass fluidized bed. The definition of the mixing index used is Lacey mixing index as shown in Section 2.3. The results for each case are presented in Fig.4.12. As observed, mixing index increases as time goes on and the bed reaches the randomly mixed state after several seconds for most of cases. The slope of mixing index curve represents the speed of mixing rate. Obviously, the mixing rate is significantly affected by the number of jets. Mixing rate is fastest for the one-jet condition and slowest for the uniform gas inlet condition in each case. However, three exceptions can be observed and discussed below:

In C1, the bed with the gas uniform inlet condition does not form bubbles because of the low gas superficial velocity which is slightly larger than U_{mf}. Bubbles play an important role in particle mixing in the bubbling fluidized bed (Shen and Zhang 1991). Therefore, particle mixing will not occur in this case, as shown in Fig. 10(a).

In C2 with a higher gas flow rate, the mixing speed for the bed with the two-jets condition is lower than the three or five jets conditions. Figs. 10(b), (c) and (d) show the particle velocity vector for simulation case 2. Particles on the bottom constitute a trailing vortex and rise along with the bubble in the center of the bed. Particles on the top fall along the wall. However, for the case with two jets, because there is no jet in the center, particles on the top may fall not only along the wall but also in the center.

Those particles can change the direction of the jet gas velocities and decrease V_z and then impact the mixing speed.

In C4 there are some fluctuations for uniform case. Fig. 10(e) shows the particle velocity vector for this case. Some particles are raised because of bubbles breaking. Therefore, in some sampling grids, there are only a few particles. According to the definition of the Lacey mixing index in equations (1) and (2), this effect can impact the value of the mixing index if there are not enough particles in a sampling grid. For example, if some sampling grids only have one particle, then the concentration of marked particle C_i will be 1 or 0. This arrangement could affect the variance σ^2 and then the mixing index. Jiang et al.(Jiang et al. 2011) and You et al.(You and Zhao 2018)adopted a weighting scheme to solve this problem, that is, a sample cell containing more particles has a greater weighting. As the inaccuracy of mixing index only appeared in the cases with large quantity of dilute phase (for example, for case 4), we still use the original definition of Lacey mixing index.

4.3.6 Contact Number (CN)

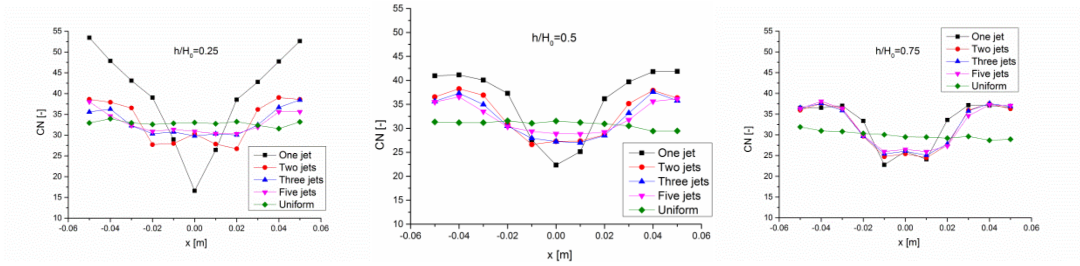

Figure 4.13. Radial distribution for the Contact number (CN) at different bed heights when gas flow rate is 1.703×10-3kg/s (C1): (a) h/H_0=0.25, (b) h/H_0=0.5, and (c) h/H_0=0.75.

Contact Number (CN) is the number of contacts in the sampling grid, and it directly affects the particle-particle heat transfer. This effect can be significant for particles with high thermal conductivity (Zhou, Yu, and Zulli 2009). In this work, the Contact Number (CN) is the number of contacts in a sampling grid. Larger CN means more particle interactions in the grid, and smaller CN means the dilute phase of particles in the grid. The value of CN is just simply counted in each grid at different bed heights (h/H0=0.25, h/H0=0.5, and h/H0=0.75) during the DEM simulation. When two particles contact with each other, their distance should be equal or less than particle diameter. The accumulation of the number of particle contact will be Contact number(CN) in each grid. And the final CN will be the average of each save time step. Fig.4.13 shows the variations in the averaged CN at different bed heights. Except for the particles in the uniform gas inlet condition, the CN with different jet numbers shows the same trend that lower CN in the center and higher CN near the wall, especially for the one-jet condition at h/H_0 = 0.25, the CN neat the wall can reach 54 and 2.6 times higher that in the center. On the other hand, the CN became more uniform with the increase of jets number. However, the difference between each cases with different jets number decreases with the increased bed height. That means that the distinction of particle movement and mixing speed between two, three and five jets cases is obvious at $h/H_0 = 0.25$ and decreases with the increased bed height. In addition, compared with the radial distribution for V_z in Fig.4.9, CN has a relationship with V_z. That means that the gas flow rate may impact the particle-particle contact, and the contact frequency will decrease with gas flow rate increasing.

For the one-jet condition, the difference in the CN between the center and annulus zone reduces at $h/H_0 = 0.5$ and is 0.75 compared with $h/H_0 = 0.25$. The reason can be found in Fig.4.10 (b). There is a dead zone in the annulus region at $h/H_0 = 0.25$ and may significantly increase the CN in this region. In addition, a minor difference between the different layers can be identified for other conditions. This result shows that the CN distribution is heterogeneous for the one-jet condition in the axial direction. This finding may impact the temperature field and the thermal behavior(Zhou et al. 2011).

4.4 Conclusions

The CFD-DEM approach is used in this work to analyze the effect of the number of jets on the particle behavior and mixing index. The pressure drop, bed expansion, particle velocity distribution and contact number are also discussed in this work. The following conclusions can be drawn from the current study:

(1) Jets number impacts flow pattern significantly. Typical spouted bed feature and bubbling fluidized bed feature can be observed from one jet cases and uniform gas inlet cases, respectively. The flow patterns for multiple jets cases are the transition for those two extreme cases.

(2) The maximum bed pressure drop is fixed, and it is independent of the gas flow rate when the fluidized bed completely reaches fluidization for the uniform gas inlet condition. However, for the multiple jets condition, the maximum bed pressure drop deceases with gas flow rate increasing. This trend is obvious with decreased number of jets. Based on the same total gas flow rate, the bed height for the one-jet condition will be significantly higher than other conditions.

(3) Generally, the mixing rate increases with the increase of gas flow rate and decrease of jets number. The analysis of particle velocities shows that the gas from multiple jets is concurrent in the center of the bed and accelerates the particles together. However, gas flow is weakened during the processing of the combination. This circumstance could be the reason for the lower mixing rate for the multiple jets condition compared with the one-jet condition.

(4) Gas flow rate in the fluidized bed affects the CN in jet fluidized beds. The contact frequency decreases with increasing gas flow rate. Furthermore, the CN distribution for the multiple jets condition is more uniform than the one-jet condition, which could impact the temperature field and thermal behavior.

CHAPTER 5 EXPERIMENTAL STUDY OF THE MIXING AND SEGREGATION BEHAVIOR IN BINARY PARTICLE FLUIDIZED BED WITH WIDE SIZE DISTRIBUTIONS

5.1 Introduction

The fluidized bed is widely used in today's industries (such as biomass energy production, pharmaceuticals, chemical engineering, and pollution control) since the first industrial-scale fluidized bed, Winkler's coal gasifier, commenced operation in 1926 (Kunii and Levenspiel, 1991). Over time, the fluidized bed has become increasingly complex and diverse to satisfy industrial needs. For example, the biomass fluidized bed is a binary particle system that includes biomass and inert particles (Fotovat et al., 2015). Thus, the mixing and segregation behavior for two types of particles with different fluidization characteristics has been intensively investigated by many researchers (Fan et al., 1970, Geldart et al., 1981, Chew et al., 2010, Babu et al., 2017).

Initial investigations for mixing and segregation behavior in a binary particle system were summarized by Nienow et al. (1978). They introduced the words flotsam and jetsam to describe segregated solids in a fluidized bed (Rowe et al., 1972), terms that are still widely used in recent research of binary particle systems. Wu and Baeyens (Wu and Baeyens, 1998) investigated the typical segregation patterns for mixtures of different size particles. Some studies of binary particle systems was based on a narrow size distribution (Rice and Jr, 1986, Rasul et al., 1999, Marzocchella et al., 2000, Wirsum et al., 2001). However, it is difficult to guarantee a narrow particle size distribution in a real industrial fluidized bed. Therefore, other researchers focused on binary particle systems with wide size distributions. Hoffmann and Romp (1991) believed that the fluidized powder of a continuous size distribution would segregate into two superimposed layers, which is similar to a binary system to some extent. Wormsbecker et al. (2005) discussed segregation for a wide size distribution in a conical fluidized bed of pharmaceutical granulate. Dahl and Hrenya (2005) used discrete particle model (DPM) to simulate segregation for a wide particle size distribution. Both Gaussian and lognormal distributions were discussed in their study. To sum up, only very limited research has been performed to investigate the mixing and segregation behavior of a binary particle system with wide size distributions. Some concepts, such as the definition of minimum fluidization velocity (Chiba et al., 1979), are still not clear for binary particle systems.

Since the fundamental mixing and segregation behavior of binary systems is still not well understood, especially for wide size distributions, the prediction, design and operation of binary systems are often based on experience rather than on scientific principles (Chew et al., 2010). Therefore, using experimental methods, such as a sampling method, is a basic and important approach to the study of mixing and segregation.

Most experimental methods for exploring mixing and segregation behavior in a fluidized bed can be divided into two categories: sampling methods and image methods. Taking samples from different areas in a fluidized bed is the conventional method for analyzing tracer particle distribution in a fluidized bed. Wormsbecker et al. (2005) used sampling probes to take samples from five different radial positions in the bed. Zhang et al. (Jin et al., 2009, Zhang, et al., 2009a, 2012) used a flashboard-box to take samples from the dense-phase area of a spout-fluid bed. They also developed a novel sampling box to separate sand and biomass. The image method is a method that analyzes the image captured by a high-speed digital CCD camera. Image methods, such as particle image velocimetry (PIV)(Willert and Gharib 1991), have been widely used in particle tracking in fluidized beds and in the study of particle mixing and segregation (Zhang et al., 2009, 2012). Compared with the sampling method, the image method is characterized by real time and accuracy. However, it is well known that images captured by a CCD camera will be dark because of high shutter speed. Thus, an expensive laser light source or halogen lamp (Dijkhuizen et al., 2010) should be used to ensure adequate lighting. A halogen lamp is a thermal light source whose high temperature may impact particle behavior in a fluidized bed (Wu and Baeyens, 1998), and non-uniform temperature distribution may even break the glass of the bed body according to our preliminary experiment.

Therefore, a fluorescent tracer technique combining image processing method will be conducted in this study. Fluidization characteristics and mixing and segregation behavior will be discussed in terms of bed pressure drop, gas velocity and mixing index. Different types of binary particle systems, including the jetsam and the flotsam-rich systems, will be analyzed and compared. The mixing indexes at different minimum fluidization velocities are also analyzed and compared with other work.

5.2 Experimental setup, Materials and Procedure

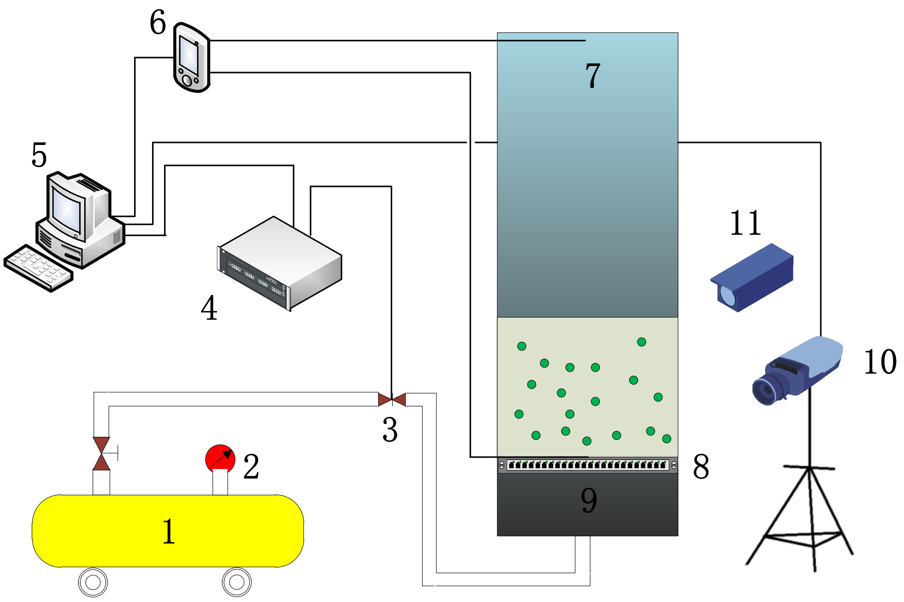

Figure 5.1 Schematic diagram of experimental setup. (1) compressor, (2) pressure gauge, (3) control valve, (4) gas flow gauge, (5) computer, (6) pressure sensor, (7) fluidized bed body, (8) gas distributor, (9) gas chamber, (10) camera, (11) germicidal lamp.

5.2.1 Fluidized bed system

A schematic diagram is shown in Fig.5.1. Fluidized gas is supplied by a compressor and controlled by a mass flow valve. The gas distributor is made of a 5-mm-thick sintered plate. The sintered plate is made by a special manufacturing process and has a 20-μm aperture, which can ensure that gas entering the fluidized bed is relatively evenly distributed. This is very important in the study of fluidized beds(Medlin and Jackson, 1975). The fluidized bed has a cross-section of 110×40 mm and height of 1000 mm. The measuring system includes a gas flow gauge, high-speed camera, germicidal lamp, lamp pressure sensor and computer. The gas mass flow can be shown by the gas flow gauge. A high-speed camera is used to record the mixing and segregation process. The shutter speed of this high-speed camera is approximately 1/1000 s or more to sufficiently freeze the particle action. A germicidal lamp is used to excite the fluorescent labeled tracer particles. The bed pressure drop is measured by two pressure taps located at the bottom and top of the bed. The signals are sent to the pressure sensor and then displayed on the computer.

5.2.2 Particle characterization

Two kinds of bed particles with wide size distributions are used in this study. The particle size distribution is measured by an LS200 laser particle size analyzer. The result is presented in Fig.5.2. The particle size distribution curve showing both kinds of particles indicates a wide size distribution that meets the need of our experiment. Green fluorescent dye is used to trace part of the silica sand. The proportion of tracer particles is 5% to ensure that there were enough tracer particles to reflect the binary particle mixtures. The properties of particles are shown in Table 5.1.

Table 5.1. Properties of particle used

Material	Color	Diameter range, d_p(um)	Bulk density, ρ_b (kg/m^3)	Voidage, ε (-)
silica sand	white	200-2000	1340	0.490
Alumina	white	200-2000	788	0.437
Tracer	green	200-2000	1340	0.490

Nienow et al. (1976) called the component that tends to settle to the bottom in binary systems "jetsam" and that which tends to float "flotsam". They also stated that a jetsam-rich system is a binary system with over 50% volume fraction jetsam, and a flotsam-rich system is a binary system with over 50% volume fraction flotsam. Thus, three types of binary mixture systems with different silica sand and alumina particle volume ratios (1:3, 1:1, 3:1) were set in our experiment.

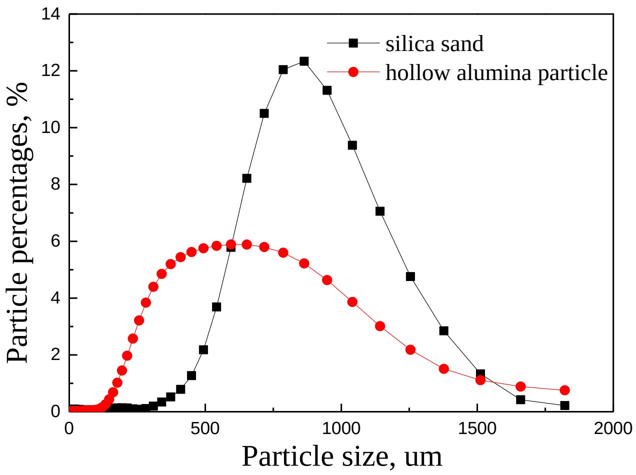

Figure 5.2 Particle size distribution curve

5.2.3 Procedure

Experiments were purposely carried out focusing on a binary particle mixture at a fixed gas velocity. As the first step, tracer and particles were initially packed in the form of good mixture. As the second step, the gas control valves for startup of the bed were turned on, and the gas flow was maintained at the desired operating condition. After the mixing reached steady state, the germicidal lamp was used to excite the fluorescent labeled tracer particles. This step took 5 min to ensure that every tracer particle was excited. The mixing process was then captured by the high-speed camera. Other data, such as gas flow and pressure, were obtained by relevant gauges. Experiments were conducted in a darkroom, and no additional interior lights were used. Therefore, the color of images we captured was dark because of the high shutter speed. The last step was a key step: the fluorescent labeled tracer particles emit light directly instead of reflecting light, so they can be easily distinguished from other particles in a dark room. After adjusting the saturation, sharpness and brightness of the images with professional software, clear images could be obtained for analyzing the binary particle mixture. This method avoided the need for an expensive laser light source.

5.2.4 Particle mixing index

To profile the axial distribution of tracer in the bed, the proportion of the number of tracer particles in each layer to the total number of tracer particles is applied and expressed by

$$C_i = \frac{n_i}{n_t} \tag{5.1}$$

where n_i and n_t are the number of the tracer particles in each layer and the total number of tracer particles contained in the bed, respectively. We also defined

$$P = \frac{C_i}{\overline{C_i}} \tag{5.2}$$

Based on statistical analyses, various mixing indices are employed to describe the particle mixing in many different industrial processes(Fan, Chen, and Watson 1970). The well-known Rowe mixing index(Rowe, Nienow, and Agbim 1972) was used:

$$M_r = \frac{x_i}{\bar{x}_i} \tag{5.3}$$

where x_i represents the mass fraction of particles in layer i. $\overline{x}_i$ indicates the average of x_i. It has been proved that the Rowe mixing index can well profile the axial mixing distribution in the bed (Nienow et al., 1978, Geldart et al., 1981, Wu and Baeyens, 1998, Wormsbecker et al., 2005, Wang and Ching, 2010). Another well-known mixing index is the Lacey (1954) mixing index, defined as

$$M_l = \frac{\sigma_0^2 - \sigma^2}{\sigma_0^2 - \sigma_m^2} \tag{5.4}$$

It should be noticed that in current work, Lacey mixing index was used to evaluate the mixing degree. The value of Lacey mixing index approaches to be zero for a completely segregated mixture and approaches to one for a fully random mixture. According to the definition of those two mixing index, Lacey mixing index can reflect the degree of mixture in whole fluidized bed and Rowe can only reflect regional axial mixing distribution. Therefore, Lacey mixing index was widely used in the process industries (Rhodes et al., 2001). In this study, Lacey mixing index was used to analyze particle mixture.

5.3 Results and discussion

5.3.1 Bed pressure drop

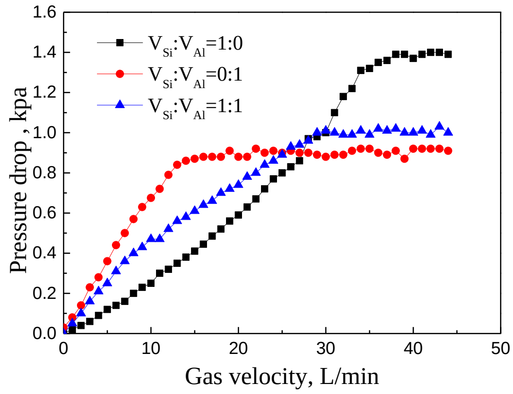

(a)

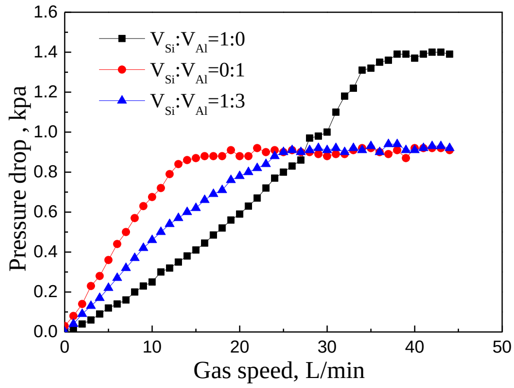

(b)

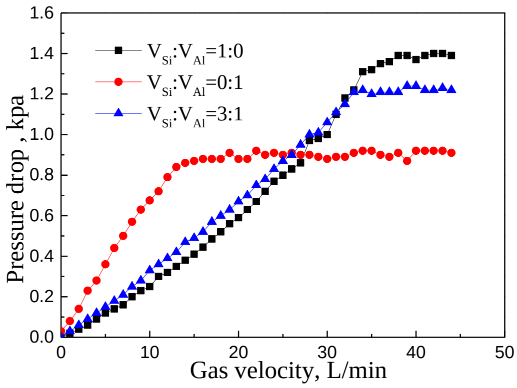

(c)

Figure 5.3 Effect of superficial gas velocity on variation of pressure drop for different binary systems. (a) V_{Si}: V_{Al}=1:1, (b) V_{Si}: V_{Al}=1:3 , (c) V_{Si}: V_{Al}=3:1.

The bed pressure drop curve is widely used to calculate the particle minimum fluidization velocity for any monodispersed particle system. However, the evaluation of the minimum fluidization velocity of binary mixture still a controversial subject (Zhang, Jin, and Zhong 2008). If the particle size is widely distributed, the system will became more complex because a monodispersed wide size distribution system can be regarded as a binary system (Hoffmann and Romp 1991) to some extent, and a binary wide size distribution system will be more complex and unpredictable. Here, a monodispersed wide size distribution particle system for silica sand and hollow alumina particles with the same total volume will also be compared with the binary particle system.

Fig.5.3 shows the profiles of the measured pressure drop of each system. For all systems, the pressure drop curve takes on a similar trend. That is, with increasing gas velocity, the total pressure drops of the bed increase in the fixed bed. Finally, when the gas velocity passes through a turning point, the total pressure drop no longer grows and keeps a constant. The turning point is defined as the minimum fluidization velocity for any monodispersed particle system (Gidaspow 1994).

For a monodispersed particle system, the final pressure drop ΔP_f of silica sand is higher than that of a hollow alumina particle because the density of silica sand is higher than that of a hollow alumina particle. For a binary particle system, the final pressure drop is between the pressure drop of those two monodispersed particle systems because the system average density $\rho_{b,a}$ of a binary particle system is between the density of those two monodispersed particle systems. The same trend can also be reflected on the location of the turning point. The turning point for a binary particle system is between the monodispersed particle systems. The turning point for a monodispersed particle system represents the minimum fluidization velocity, therefore, in this study, the turning point for a binary particle system is defined as the theoretic minimum fluidization velocity, $u_{mf,t}$.

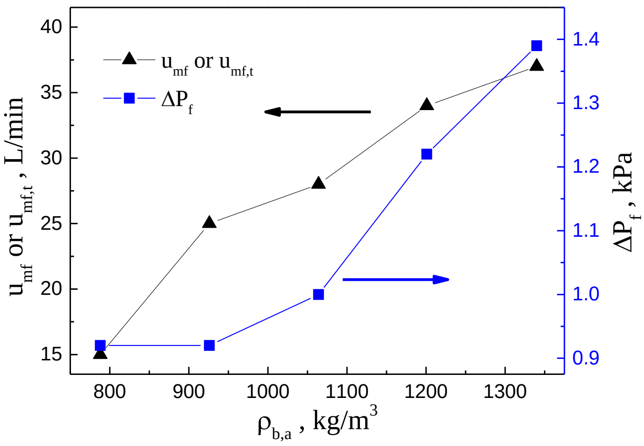

Figure 5.4 Minimum fluidization velocity and final pressure drop as a function of system average density

Fig.5.4 displays the minimum fluidization velocity and final pressure drop as functions of system average density. We can find that both minimum fluidization velocity and final pressure drop show a nonlinear relationship. A similar phenomenon can be found in earlier research. Cheung et al. (Cheung, Nienow, and Rowe 1974) studied the binary particle system of different sized particles. They believed that the minimum fluidization velocity of a binary particle system should be a function of the square of the jetsam mass component x_j:

$$\frac{u_{mf,t}}{u_{mf,f}}=[\frac{u_{mf,j}}{u_{mf,f}}]^{x_j^2} \tag{5.5}$$

where $u_{mf,j}$ and $u_{mf,f}$ are the minimum fluidization velocities of jetsam and flotsam, respectively.

Based on the Ergun equation, S. Chiba et al. (Chiba et al. 1979) presented the minimum fluidization velocity of totally mixed and totally segregated systems: for a totally mixed system,

$$u_{mf,t}=u_{mf,f}\,\frac{\bar{\rho}}{\rho_f}(\frac{\bar{d}}{d_f})^2 \tag{5.6}$$

and for a totally segregated system,

$$u_{mf,t}=\frac{u_{mf,f}}{1-x_j+x_j\,\dfrac{u_{mf,f}}{u_{mf,j}}} \tag{5.7}$$

Where $\bar{\rho}$ and $\bar{d}$ are the average density and average particle diameter, respectively. ρ_f and d_f are the density and diameter for flotsam, respectively.

However, none of the formulas can fit our experimental result. This may be explained by the fact that for a binary particle system with wide particle size distributions, it is difficult to reach completely mixed or segregation state. Moreover, the influence factor for minimum fluidization velocity will be more than just density, particle size and jetsam or flotsam mass component. The result also depends on the particle size distribution curve, the degree of sphericity and the mixing degree in the fluidized bed. Those variables are polytropic, and some of them can be analyzed only by empirical formula. Therefore, previous theoretical research can only be used for reference in the study of a wide particle size distribution to a limited extent.

5.3.2 Fluidization phenomenon at different gas velocities

By using the experimental method introduced above, the phenomena of fluidization and mixing of a binary particle system can be observed clearly. A tremendous number of snapshots were acquired for different operating conditions during the experimental process, and the disciplines for all three binary particle systems are the same. Therefore, only a few snapshots for the system in the case of V_{Si}: V_{Al}=1:1 will be shown here.

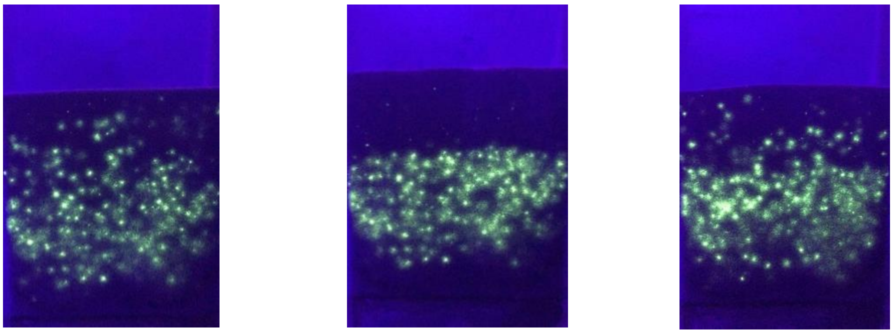

(a) (b) (c)

Figure 5.5 Mixing patterns observed in the experiment when V_{Si}: V_{Al}=1:1. (a) $u_g = u_{mf,f}$, (b) $u_g = u_{mf,t}$, (c) $u_g = u_{mf,j}$

Fig.5.5 presents snapshots of particle mixing at different gas velocities for the system when V_{Si}: V_{Al}=1:1. The experiment starts from a well-mixed packing state. When the gas velocity reached the minimum fluidization velocity of flotsam (alumina particle) $u_{mf,f}$, only a few alumina particles on the top of the bed were fluidized. In the meanwhile, small bubbles can be observed on the surface of the bed. Most of the particles did not move. When the gas velocity reached the theoretic minimum fluidization velocity $u_{mf,t}$ calculated by the pressure drop curve in the above section, the whole bed was still partially fluidized. It can be observed that most of the alumina particles were segregated from silica sand and fluidized on the upper layer. The silica sand moved slowly. When the gas velocity reached the minimum fluidization velocity of jetsam (silica sand) $u_{mf,j}$, almost all bed particles were fluidized. The mixing began to appear on the upper layer and became more obvious with increasing gas velocity.

It should be noted that during the whole experimental process, there was a “dead region” on the bottom layer of the bed. As shown in Fig.5.5, those particles form the dark region on the bottom layer of the bed, which was not marked by fluorescent labeled tracer particles. Those particles represented the larger and lower degree of spherical silica sand. The particle distribution curve in Fig.5.2 shows that only a lower proportion of larger silica sand would be marked from the total marked particles. Therefore, when the larger silica sand flocks to the bottom layer, this region will become dark. The particles in the dead region are extraordinarily difficult to become fluidized. Even if the gas velocity reaches $u_{mf,j}$, the particles in the dead region still cannot be fluidized.

5.3.3 The axial distribution of tracer particles

For quantity analysis of the mixing degree, the mixing index should be calculated. It should be noted that the distribution of tracer particles we obtained from the image may not be the real distribution because of the wall effect. Therefore, we took a few samples from the inside of each layer and counted the number of tracer particles. The results showed that the wall effect in this study can be ignored. Thus, the mixing index calculated from the image can reflect the real distribution in the bed.

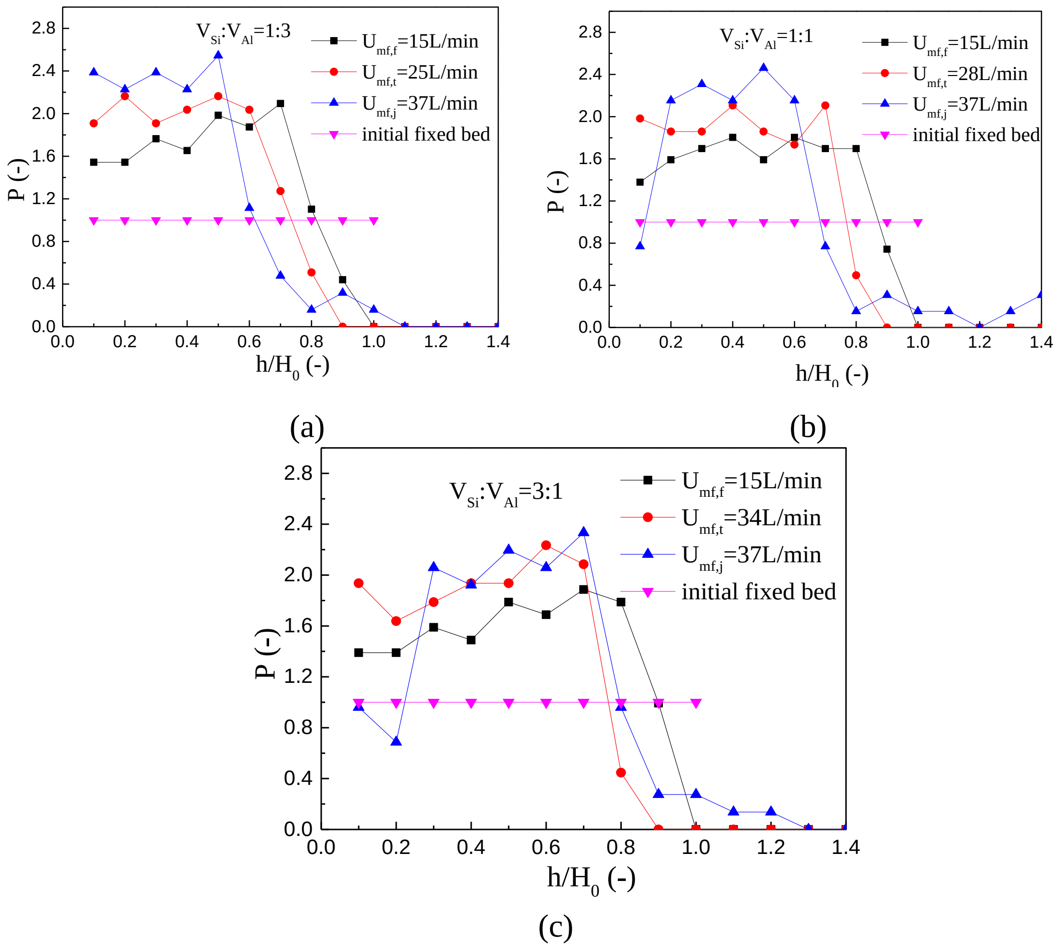

Figure 5.6 Axial profile of tracer particles proportion at various minimum fluidization velocities. (a) V_{Si}: V_{Al}=1:3, (b) V_{Si}: V_{Al}=1:1, (c) V_{Si}: V_{Al} =3:1.

Fig.5.6. shows the axial distribution of tracer proportions at various minimum fluidization velocities. Here, H_0 is the height of the initial fixed bed. At the initial fixed bed when tracer particles are well mixed with other particles, the p value is equal to 1, and the tracer particles still hold at the stagnant state. Meanwhile, it can be found that at $u_{mf,f}$, only a few alumina particles on the top of the bed are fluidized. Therefore, tracer particles that represent the silica sand in the top region will move to the lower layer. This trend will be maximized at $u_{mf,t}$ when silica sand and alumina

particles are separated completely. With the increase of the gas velocity, a few silica sand particles then begin to fluidize and mix with alumina particles in the top regions.

The impact of the dead region on tracer particles depends on the volume ratio of silica sand and alumina particles. At V_{Si}: V_{Al}=1:3, the effect of the dead region is not obvious. At V_{Si}: V_{Al}=1:1, it can be found that the dead region cannot be ignored when the gas velocities are in the range of $u_{mf,t}$-$u_{mf,j}$. The size of the dead region also depends on the volume ratio. At V_{Si}: V_{Al}=3:1, the dead region at $u_{mf,j}$ will be double that of the system V_{Si}: V_{Al}=1:1 at the same gas velocity.

5.3.4 Mixing index at different minimum fluidization velocities

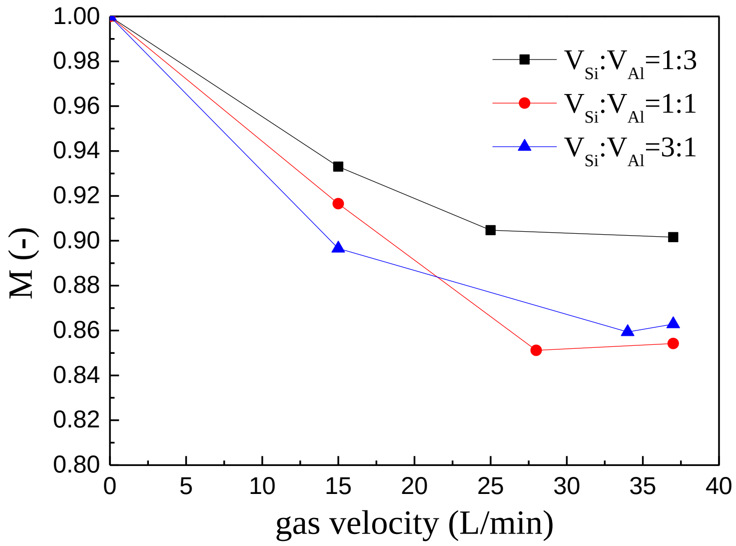

Figure 5.7 Effect of different minimum fluidization velocities on the mixing index

The mixing index is used to quantify the mixing and segregation effect. Fig.5.7 reports the mixing index calculated by equation (4) at different minimum fluidization velocities. The index decreased with increasing gas velocity before $u_{mf,t}$. This is because of separation in the binary system. The same trend can also be found in the work of Zhang et al. (Zhang, Jin, and Zhong 2009b). After $u_{mf,t}$, the impact of the binary system separation effect will not increase with increasing gas velocity. Instead, there are two main effects on the system. On the one hand, the dead region will form, which will decrease the mixing index. On the other hand, the jetsam (silica sand) becomes fluidized, and a few particles will mix with flotsam (alumina particles), thus, the mixing index may be unchanged or even increased slightly.

The study of the dead region is very important because most binary systems designed for a biomass fluidized bed (Zhang, Jin, and Zhong 2009b) are jetsam-rich systems. According to our study, the impact of the dead region will be obvious in a jetsam-rich system (V_{Si}: V_{Al}=3:1). In addition, in the industry applications of binary fluidized systems, the particles used have a wide size distribution and low degree of sphericity. Therefore, it is easy to form a dead region in the bottom layer of the fluidized bed. The dead region not only will affect the fluidization and particle mixing but also may impact mass and heat transfer between particles in the fluidized bed. This region should be considered for the design of a biomass fluidized bed.

5.4 Conclusions

An experimental investigation on a wide size distribution binary system has been conducted in a fluidized bed. A fluorescent tracer technique combining image processing method has been used to analyze particle distribution. Three types of binary mixture systems with different silica sand and alumina particle volume ratios (1:3, 1:1, 3:1) were used for the experiments. The fluidization and mixing behavior is analyzed in terms of bed pressure drop, particle concentration profile, and mixing index. The mixing indexes at different minimum fluidization velocities are also analyzed and compared with other work. The following conclusion can be drawn from this work.

(1) The theoretic minimum fluidization velocity, $u_{mf,t}$, calculated from the bed gas pressure drop cannot represent the whole fluidization in the bed because the particles will separate, and the jetsam (silica sand) will not be fluidized at this gas velocity.

(2) For a wide size distribution particle binary system, there is a dead region in the bottom layer. The impact of the dead region depends on the gas velocity and volume ratio for a binary system. It is extraordinarily difficult to fluidize for the particles in the dead region.

(3) When the gas velocity reaches $u_{mf,j}$, except for the particles in the dead region, most of the jetsam particles are fluidized, and a few of them will mix with flotsam particles.

CHAPTER 6 ANALYSIS OF PARTICLE ROTATION IN FLUIDIZED BED BY USE OF DISCRETE ELEMENT MODEL

6.1 Introduction

Recent years have seen a rapid growth of interests in detailed particles motion in a wide variety of natural and industrial processes. Particle motion possesses significant influence on the hydrodynamics in these processes. For example, in industrial fluidized beds such as circulating fluidized bed (CFB) risers, the particles experience not only translational but also rotational motion due to the frequent particle-particle collisions and the relative velocity between solids and the surrounding airflow (Yuan et al., 2001). Particle rotation appears to have effect on the linearity of the motion and may play a part in the mechanism of particle entrainment in conveyed solid-gas system (Torobin and Gauvin, 1960).

Some experimental methods was used to track particle rotation and analyzed relevant influence factors such as particle size, average particle collision velocity, particle collision rate and particle number density (Wu et al., 2008b). Other researchers tried to obtain the angular velocity by use of the digital imaging method. For example, with a high-speed digital camera system, Wu et al. (2008a, 2008b)measured the averaged particles rotational velocity in a cold CFB riser. They found the mean rotational velocity for particles with a density of 2400-2600kg/m^3 and size of 0.5 mm was about 300 rev/s whilst the highest rotational velocity could be up to 2000 rev/s. The study on particle rotation, however, still presents a big challenge since the direct measurement of particle angular velocity is, if not impossible, extremely hard.

Relatively more contributions have been made to numerical study of particle in solid-gas two-phase flows (Garoosi et al., 2015). In the interesting work by Kajishima et al. (2004), they found that, due to the reverse direction of lift force in the shear flows, the irrotational particles could be easily absorbed into clusters but rotational ones might escape. Similar conclusion can be found by Wang et al. (2008)who argue that particle rotation reduce the cluster size. Sun et al. (2006)found that the multi-fluid model taking the particle rotation into account could better capture the bubble dynamics and time-averaged bed behavior in fluidized bed. Despite the significance of particle rotation in solid-gas two-phase flows found in the aforementioned studies, much are yet to be understood on how the particle rotation affects hydrodynamics.

It is widely accepted that the rotational particles experience a Magnus lift force, which is perpendicular to the plane constituted by particle translational and rotating velocities. The Magnus lift force was first discovered by Newton in 1671(1971), and the Magnus effect in particle systems has since been a subject to many investigations(Oliver, 1962, Ning and Xiaojing, 2001, Lukerchenko, 2001, White and Schulz, 1977). Oliver(1962)attempted to explain some phenomena and behaviour of particle in tubes by using Magnus effect. White and Schulz (1977)studied the motion of spherical glass microbeads (of diameter 350 um and density 2.5 g/cm^3) in a wind tunnel, and found that their results could be well explained by the Magnus effect. Lukerchenko (2001) found the existence of Magnus effect in solid particle saltation over rough bed in a numerical study, and Huang et al. (2001) further demonstrated the trajectories of saltating grains could be influenced by the Magnus effects. Dandy and Dwyer (1990) compared the Magnus lift force and drag force acting on a particle over a wide range of Reynolds number, and showed the magnitude of the Magnus lift force was far less than that of drag force. You et al. (2003) also think that for a small size particle, even if the speed reaches 10^6 rev/min, the lift force can be neglected as compared with the drag force. However, in a very recent work Zhou and Fan (2015a) studied the solid-fluid interaction by use of an immersed boundary lattice Boltzmann simulations, and their results suggest that the Magnus force might become even larger than the drag force in case of high Reynolds number and low solid volume fraction in particulate flows.

A natural question thus is whether the influence of particle rotation, especially the Magnus lift force, can be ignored or not in fluidized bed reactors. In this work, we aim at the study of Magnus lift force on the hydrodynamics of fluidized beds by use of discrete particle model. The underlying inspiration is that the discrete particle model can be used as an efficient learning tool for solid-gas interaction at particle level. According to Zhou and Fan (2015a), the Magnus effect is more pronounced for high Re and low solid volume fractions. Therefore in this research we will focus on the particle rotation and Magnus effect in circulating fluidized bed (CFB) risers. Our results show that the influence of Magnus lift force is enhanced with a higher Re_r .

Magnus lift force affects the movement of particles in both radial and axial directions while Re_r is high. However, in low Re_r case it can be neglected in computational simulation model. This indicates the introduction of Magnus lift force may improve the discrete particle model only in high Re_r case and Magnus effect should be considered in real gas-solid two phase system when the particle rotational speed is high.

6.2 Mathematical model

The DEM-code was originally developed by Kuipers et al. and has been validated and extensively applied in various solid-gas two-phase systems (Ye et al., 2004, Ye, Hoef, and Kuipers, 2005a, 2005b).

6.2.1 Gas phase

The gas flow is described by the volume-averaged Navier-Stokes equation (Kuipers et al. 1992):

$$\frac{\partial(\varepsilon\rho_g)}{\partial t} + (\nabla \cdot \varepsilon\rho_g \mathbf{u}) = 0 \tag{6.1}$$

$$\frac{\partial(\varepsilon\rho_g \mathbf{u})}{\partial t} + (\nabla \cdot \varepsilon\rho_g \mathbf{uu}) = -\varepsilon\nabla p - S_p - \nabla \cdot (\varepsilon\bar{\tau}) + \varepsilon\rho_g g \tag{6.2}$$

Where ε presents the porosity, g the gravity acceleration, ρ_g the gas density, u the gas velocity, $\bar{\tau}$ the viscous stress tensor, and p the pressure of the gas phase. Based on the Newton's third law, the equivalent of that force must be acting on the mesh cell that the particle resides in. So the Magnus effect on gas phase should have been considered in equation 2. The solution in our study is to correct source term S_p . The source term S_p is:

$$S_p = \frac{1}{V}\int \sum_{a=0}^{N_{part}} [\mathbf{F_{dra,a}} + \mathbf{F_{mag,a}}]\delta(\mathbf{r} - \mathbf{r_a})dV \tag{6.3}$$

where V is the volume of fluid cell, V_a the volume of particle, υ_a the particle velocity, and N_{part} the number of particles. The δ - function is to ensure the reaction force acts as a point force at the position of the particle (Bokkers et al., 2004). $F_{dra,a}$ and $F_{mag,a}$ are drag force and Magnus lift force which will be discussed in 2.2.3. To solve the pressure linked equation, the SIMPLE algorithm is used in this research (Ferziger and Perić, 1996).

6.2.2 Particle phase

In the DEM, the Newton's second law is used to track the velocity and position of each particle:

$$m_a \frac{d^2\mathbf{r_a}}{dt^2} = \mathbf{F_{cont,a}} + \mathbf{F_{mag,a}} + \mathbf{F_{dra,a}} - V_a \nabla p + m_a g \tag{6.4}$$

$$I_a \frac{d^2\Theta_a}{dt^2} = \mathbf{T_a} \tag{6.5}$$

where m_a is the mass of particle, I_a the moment of inertia, Θ_a the angular displacement, and T_a the torque of particle. In this research we consider three types of force acting on the particles: the contact force $F_{cont,a}$, the drag force $F_{dra,a}$ and the Magnus lift force $F_{mag,a}$.

6.2.2.1 Contact force

The contact force $F_{cont,a}$ includes both normal and tangential component,

$$\mathbf{F_{cont,a}} = \sum_{contactlist} (\mathbf{F_{ab,n}} + \mathbf{F_{ab,t}}) \tag{6.6}$$

In this research the linear-spring/dashpot soft-sphere model (Cundall and Strack, 1979) is used to calculate the contact force. The normal and tangential component are respectively given by:

$$\mathbf{F_{ab,n}} = -k_n \delta_n \mathbf{n_{ab}} - \eta_n \boldsymbol{\upsilon}_{\mathbf{ab,n}} \tag{6.7}$$

and

$$\mathbf{F_{ab,t}} = \begin{cases} -k_t \delta_t - \eta_t \boldsymbol{\upsilon}_{\mathbf{ab,t}},\ for |\mathbf{F_{ab,t}}| \le \mu_f |\mathbf{F_{ab,n}}| \\ -\mu_f |\mathbf{F_{ab,n}}| t_{ab},\ for |\mathbf{F_{ab,t}}| > \mu_f\ |\mathbf{F_{ab,n}}| \end{cases} \tag{6.8}$$

Here k is the spring stiffness, η the damping coefficient, n_{ab} the normal unit vector, δ_n the overlap, δ_t the tangential displacement, μ_f the friction coefficient and υ_{ab} the relative velocity between two particles.

6.2.2.2 Drag force

The traditional drag model, which is a combination of Ergun equation for dense regime and Wen-Yu correlation for dilute regime, is used in this research (Ergun and Orning, 1949, Wen and Yu, 1966):

$$\mathbf{F}_{\mathbf{dra,a}} = 3\pi\mu_g \varepsilon^2 d_p (\mathbf{u} - \boldsymbol{\upsilon}_\mathbf{a}) f(\varepsilon) \tag{6.9}$$

$$f(\varepsilon) = \begin{cases} \dfrac{150(1-\varepsilon)}{18\varepsilon^3} + \dfrac{1.75}{18}\dfrac{Re_p}{\varepsilon^3}, \varepsilon < 0.8 \\ \dfrac{C_d}{24} Re_p \varepsilon^{-4.65}, \varepsilon \geq 0.8 \end{cases} \tag{6.10}$$

Here the particle Reynolds number $Re_p = \dfrac{\varepsilon d_p (\mathbf{u} - \boldsymbol{\upsilon})\rho_g}{\mu_g}$, where ε is the void fraction, d_p the diameter of particle, and μ_g the dynamic viscosity. The drag coefficient $C_d = \dfrac{24}{Re_p}(1 + \dfrac{3}{16} Re_p)$ follows Oseen (Oseen 1911).

6.2.2.3 Magnus lift force

The calculation of the Magnus lift force follows Zhou & Fan (Zhou and Fan 2015b):

$$\mathbf{F_L} = \frac{3\pi\mu_g d_p \mathbf{u} Re_r}{\varepsilon^2}[-0.0398(1-\varepsilon)+0.0317] \quad (6.11)$$

Here the rotational Reynolds number $Re_r = \frac{\rho_g \vec{\omega} d_p^2}{\mu_g}$, where ω is the particle rotational velocity, and u the velocity of fluid. In their study, Zhou and Fan introduced a coordinate frame with the origin fixed at the center of particle, and thus the translational motion of particle can be ignored in the calculations. In this research, we used a coordinate frame with the origin fixed at the wall of reactor, and thus the Magnus force is calculated as:

$$\begin{aligned} F_{mag,a} &= \frac{3\pi[-0.0398(1-\varepsilon)+0.0317]\rho_g d_p^3}{\varepsilon^2}\boldsymbol{\omega}\times(\boldsymbol{\upsilon}_\mathbf{a}-\mathbf{u}) \\ &= \frac{3\pi[-0.0398(1-\varepsilon)+0.0317]\rho_g d_p^3}{\varepsilon^2}\begin{vmatrix} i & j & k \\ \omega_x & \omega_y & \omega_z \\ \upsilon_{x,a}-u_x & \upsilon_{y,a}-u_y & \upsilon_{z,a}-u_z \end{vmatrix} \end{aligned} \quad (6.12)$$

And the three components of the Magnus force are:

$$\begin{cases} F_{xmag,a} = \frac{3\pi[-0.0398(1-\varepsilon)+0.0317]\rho_g d_p^3}{\varepsilon^2}\left[\omega_y(\upsilon_{z,a}-u_z)-\omega_z(\upsilon_{y,a}-u_y)\right] \\ F_{ymag,a} = \frac{3\pi[-0.0398(1-\varepsilon)+0.0317]\rho_g d_p^3}{\varepsilon^2}\left[\omega_z(\upsilon_{x,a}-u_x)-\omega_x(\upsilon_{z,a}-u_z)\right] \\ F_{zmag,a} = \frac{3\pi[-0.0398(1-\varepsilon)+0.0317]\rho_g d_p^3}{\varepsilon^2}\left[\omega_x(\upsilon_{y,a}-u_y)-\omega_y(\upsilon_{x,a}-u_x)\right] \end{cases} \quad (6.13)$$

6.2.3 Numerical simulations

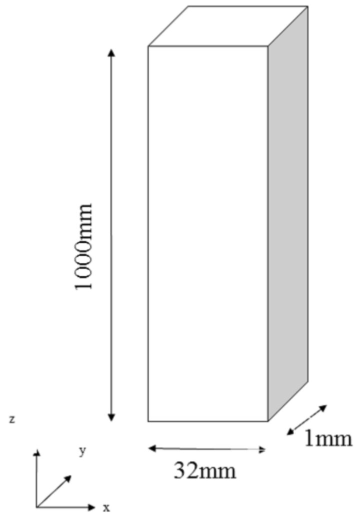

Figure 6.1 Schematic diagram of the geometry of the pseudo-2D bed

The schematic diagram of the pseudo-2D gas-fluidized bed is shown in Fig.6.1. The depth of the bed is the diameter of a single particle. In total $25 \times 1 \times 300$ fluid grid cells are used in this research. The simulation parameters are listed in Table 6.1. Most parameters follows the experiments and simulations by Mathiesen et al. (2000). A mixture of two kinds of particles is considered. The time step is estimated by the method of Tsuji et al. (1993):

$$\Delta t < \frac{2}{5}\pi\sqrt{\frac{m_a}{k}} \tag{6.14}$$

Before the formal simulation experiment, particle-wall contact should be discussed, which occurs frequently in a reactor or channel (Hu et al., 2017, Dritselis, 2017, Cheikh et al., 2017). And particle-wall contact may cause erosion on the pipe. Salaei et al. (2014) discussed particle erosion in a 90° pipe bend. They found particle erosion happened on the bend area. In this study, a cuboid model was built to simulate fluidized bed. Therefore, No-slip boundary is used for the four sidewalls, the fluid phase influx cell (gas inlet boundary) is set at the bottom of the bed where the gas is injected, and the prescribed cell (pressure outlet boundary) is set at the top of the bed. Particles are settled in the bottom of the bed at the beginning. When a particle reaches the top boundary a new one will be introduced to enter the bottom, so the number of particles in bed will be a constant. The turbulence is not consider in this study.

Table 6.1 Simulation parameters

Parameter	Value	Unit
Gas temperature, T	293	(K)
Shear viscosity of gas, μ_g	1.8×10^{-5}	(Pas)
Molar mass of gas, M	2.9×10^{-2}	(kg/mol)
Number of particles, N_{part}	40500	(-)
Number of particles1, N_{part1}	20250	(-)
Number of particles2, N_{part2}	20250	(-)
Diameter of particle1, d_{a1}	1.2×10^{-1}	(mm)
Diameter of particle2, d_{a2}	1.85×10^{-1}	(mm)
Density of particle, ρ_s	2400	(kg/m3)
Inlet gas velocity, U_g	1.0	(m/s)
Normal restitution coefficient, e_n	0.97	(-)
Normal restitution coefficient wall, $e_{n,w}$	0.97	(-)
Tangential restitution coefficient, e_t	0.33	(-)
Tangential restitution coefficient, $e_{t,w}$	0.33	(-)
Friction coefficient, μ	0.1	(-)
Normal spring stiffness, k_n	7.0	(-)
Tangential spring stiffness, k_t	2.0	(-)
Time step, dt	2.0×10^{-5}	(s)

Table 6.2 Case parameters

Case number	Without Magnus	With Magnus
1	$Re_r\sim10^0$	$Re_r\sim10^0$
2	$Re_r\sim10^1$	$Re_r\sim10^1$
3	$Re_r\sim10^2$	$Re_r\sim10^2$

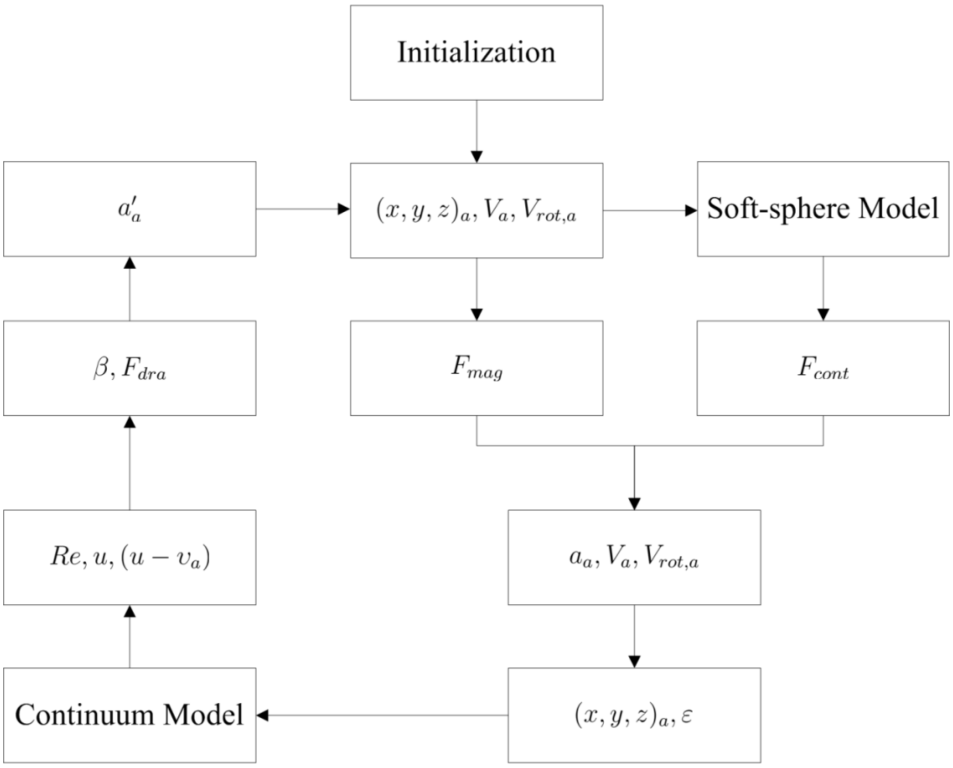

Figure 6.2 The flow diagram of numerical simulations.

The case parameters can be shown in Table 6.2. The flow diagram of numerical simulations is shown in Fig.6.2. After initialization, the new position and velocity of particles as well as local porosity are updated by use of the soft-sphere model described in Section 6.2.2. Then the governing equations in Section 6.2.1. will be solved, and the fluid field and particle position and velocity at this time step are calculated and saved.

6.3 Results

According to Ibsen et al. (2004), the discrete particle simulation should run sufficiently long time to ensure the whole system reaches the steady state. In this research, we simulated 16 seconds physical time and the time step is 2.0×10^{-5} s. Only the results in the last 5 seconds were used for data analysis. The results of force, particle velocity and particle velocity fluctuation which present in this work is averaged for the last 5 seconds.

For analyzing the influence of Magnus effect, firstly, Magnus lift force for every standalone particle in each case is counted and compared with drag force. Secondly, particle velocity distribution in two models are calculated. Subsequently, regional particle velocities is discussed in each case. Finally, the particle velocity fluctuation curves are used to analyze different rotational Reynolds number cases.

The results and analysis will mainly focus on the z-component of the particle velocity. Because in pseudo-2D system , the particle velocity in y-component can be neglected. Particle velocity on x-component will also be discussed for assistant analysis.

The Re_r plays an important role in the Magnus effect according to the definition of the Magnus lift force in section 6.2.2.3 and will be set as an independent variable in this study. In this work, three Re_r values are considered: 1, 10, and 100. According to the definition of the Re_r, the value of the Re_r can be changed through modification of any of three parameters. The first option is modification of a gas parameter such as dynamic viscosity or gas velocity. The second option is modification of particle size. The third option is to change the rotation speed. If we set the first two parameters as independent variables, the drag force will be changed accordingly. Thus, in formal simulation experiments, we change the rotation speed artificially to ensure that only the Magnus lift force is different in different three case. We believe this approach can highlight the effect of the Magnus lift force instead of the combined effect of the Magnus lift force and the drag force.

6.3.1 Particle positions

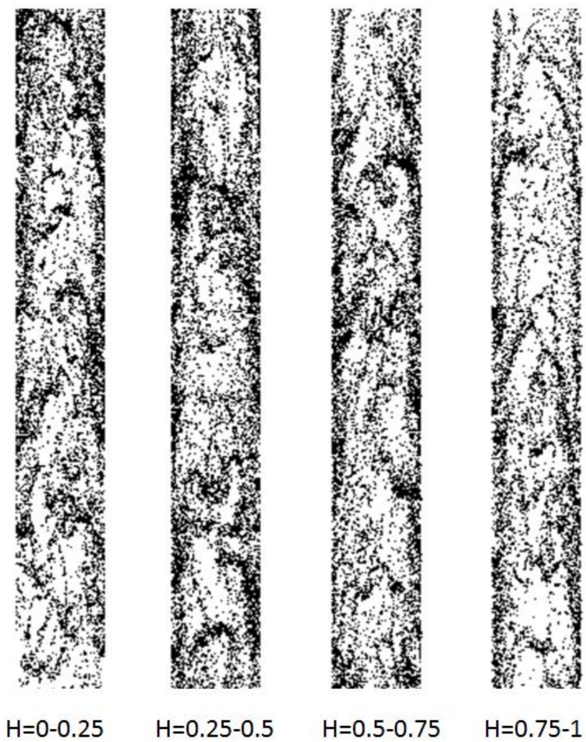

Figure 6.3 The snapshots of the instantaneous position of particles in the riser.

Instantaneous particle positions for different values of Re_r were simulated in the CFB riser. Fig.6.3 shows the typical results at t = 13 s. The particles are dilute in the core region and dense in the wall region, consistent with the results of Mathiesen et al. (2000). The shape of particle cluster in some region is parabolic, which indicates the particles move upward at a faster speed near the central of the riser and downward at a slower speed near the sidewalls.

6.3.2 Effect of the Magnus lift force

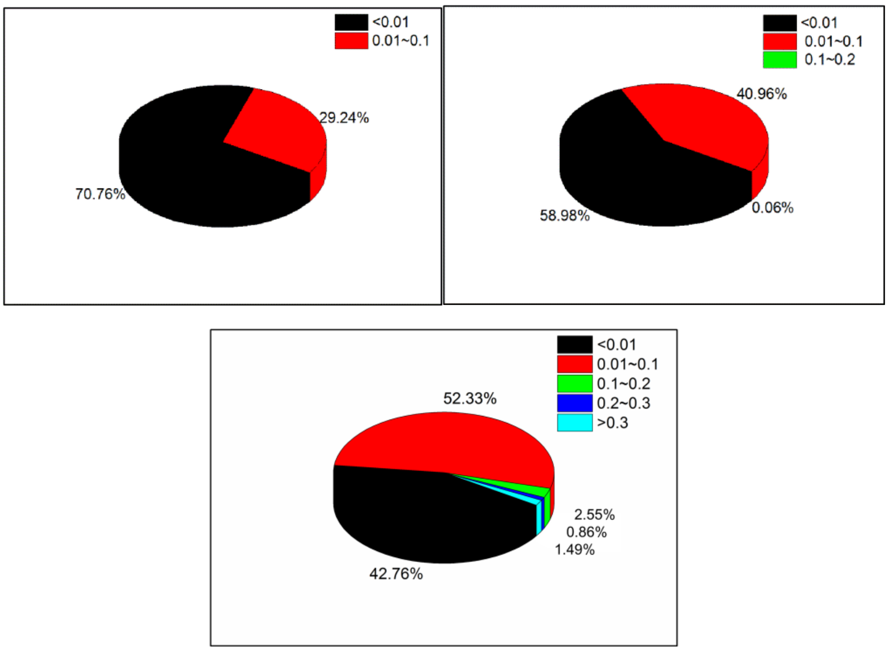

Figure 6.4 The percentage of particles classified by $F_{zmag,a} / F_{zdra,a}$: (a) case 1, (b) case 2, (c) case 3.

Drag force is considered as the major force which impact particle movement in fluidized bed. Therefore, the ratio among Magnus lift force and drag force is important for analyzing the impact of Magnus lift force in fluidized bed. Fig. 6.4 show the percentage of particles classified by $F_{zmag,a} / F_{zdra,a}$ in different case. As can be seen in Fig.6.4(a), the $F_{zmag,a} / F_{zdra,a}$ for most particles is smaller than 0.01, which is exclusively smaller than 0.1, which means the Magnus lift force is negligible compared to the drag force when $Re_r \sim 10^0$. This can also be evidenced by Zhou and Fan(2015a), the lower the Reynolds number, the weaker the Magnus effect. In Fig.6.4(b), the percentage of particles with $F_{zmag,a} / F_{zdra,a}$ in the range of 0.01~ 0.1 is higher, which suggests the Magnus lift force at $Re_r = 10$ would affect the particle motion. For even higher Re_r as showed in Fig.6.4(c), the magnitude of Magnus lift force, though less than that of drag force, becomes more pronounced. For some particles, these two forces are even in the same magnitude. Therefore, Magnus lift force might have an apparent influence on the movement of particles.

6.3.3 Particle velocity distribution

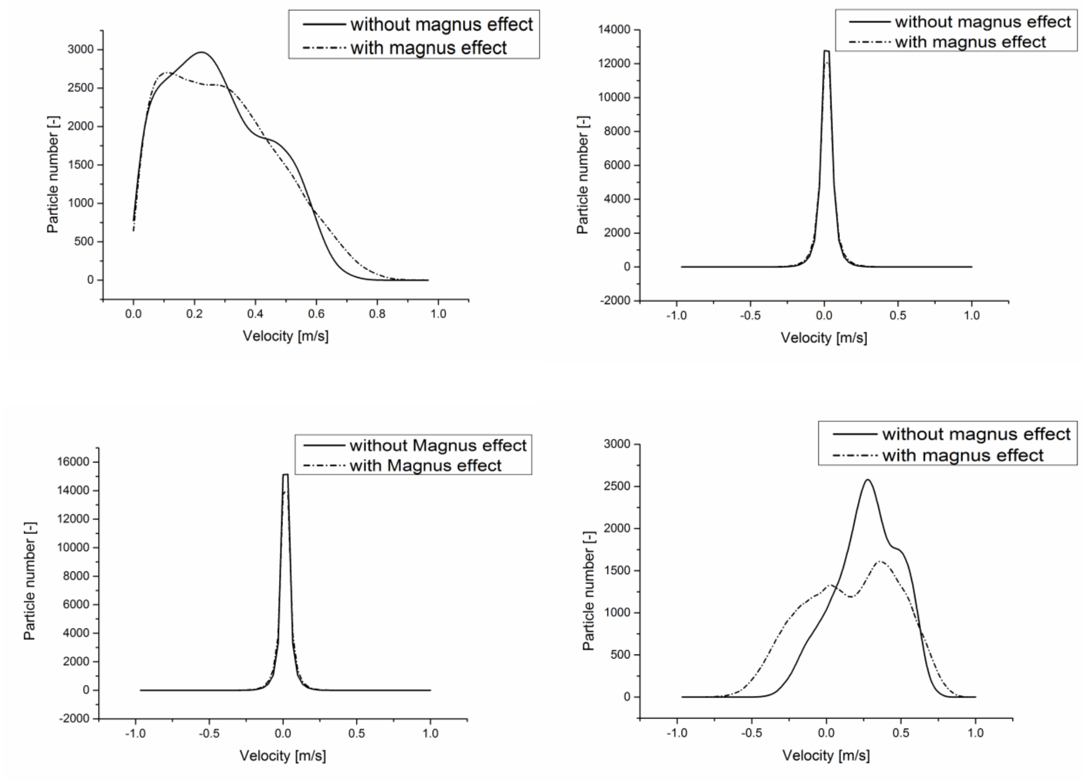

Figure 6.5 Particle normal velocity distribution in case 3: (a) normal velocity distribution, (b) X-direction velocity distribution, (c) Y-direction velocity distribution, (d) Z-direction velocity distribution.

We analyze the particle velocity distribution for explaining the impact of Magnus lift force. The low Re_r case cannot reflect the effect of Magnus lift force according to the result in section 6.3.2. Therefore, we discuss the particle velocity distribution for high Re_r case. Particle normal velocity distribution is showed in Fig.6.5(a). The particle velocities in three directions were considered separately in Figs.6.5(b),(c),(d). At X and Y-direction, particle velocity distribution is Maxwell distribution which indicate the homogeneity of particle velocity distribution in this two directions. The gas velocity at Z-direction is much higher than other two directions. On one hand this lead to higher drag force at Z-direction. On the other hand according to Eq. 6.13, the influence of Magnus lift force at Z-direction will be much lower than other two directions if u_z is far larger than u_x and u_y. The difference between two curves: with or without Magnus lift force in Fig.6.5(d) proved the existence of this Magnus effect at Z-direction. For high Re_r case, Magnus lift force may change the trajectory of particles.

6.3.4 Regional Particle velocity

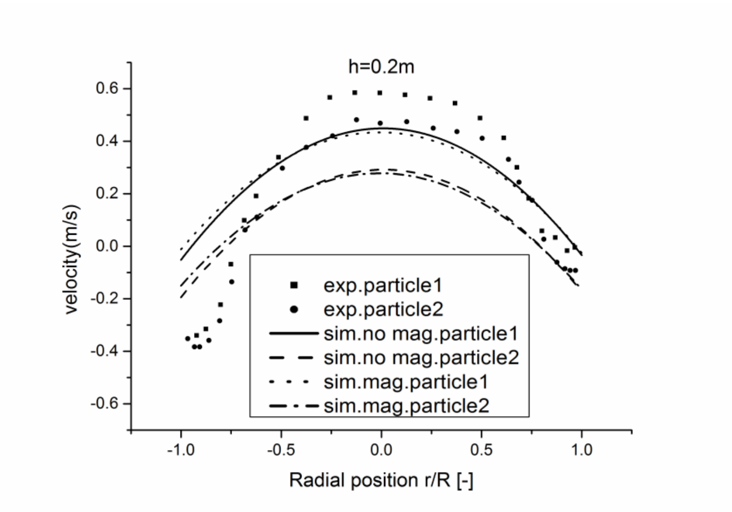

Figure 6.6 Radial profiles of Z-direction velocity at different height in case 1, h=0.2m

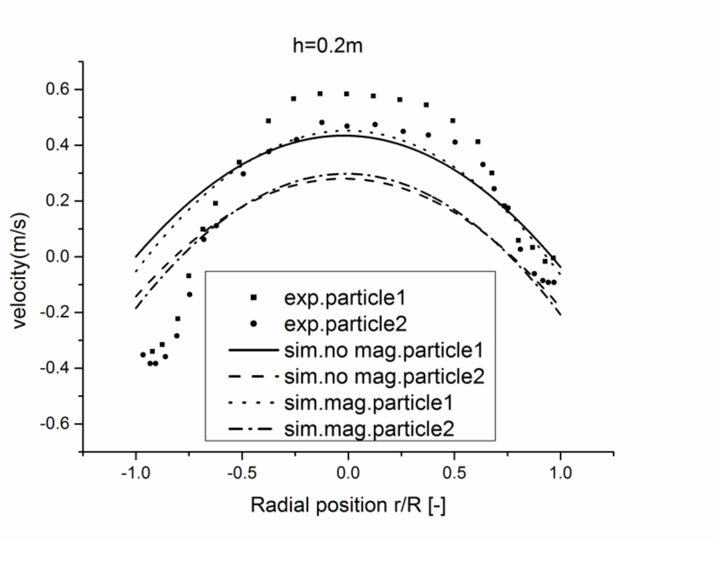

Figure 6.7 Radial profiles of Z-direction velocity at different height in case 2, h=0.2m

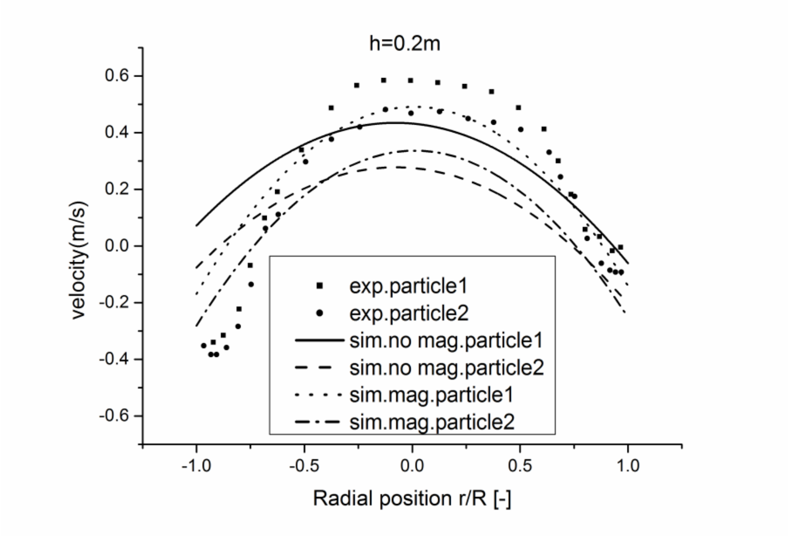

Figure 6.8 Radial profiles of Z-direction velocity at different height in case 3, h=0.2m.

Regional particle velocity is another important standard to reflect the effect of Magnus lift force. According to the result in section 6.3.3, even in high Re_r case the impact of Magnus lift force on particle velocity on X- direction and Y- direction can be neglected. Therefore in this section we discuss Regional particle velocity on Z-direction. Figs.6.6 to 6.8 plot the radial profiles of particles vertical velocity. The results are compared with the experimental data by Mathiesen et al (2000). There are some differences between experiment and simulation results. In the wall regions, simulation results are high than experimental results. Besides, at h=0.2m, the velocities are not correctly predicted very well. The velocities in core regions are lower than experiment while in wall regions are higher than experiment. The probably reasons are as follows: Firstly, particles at h=0.2m suffer from more fierce collision in real fluidized bed which result in the expansion of different velocities between wall regions and core regions. Secondly, this might well be related to the boundary conditions for fluid and particles which has been set in simulation model, leading to an artificial entry length in the flow. Finally, the different methods on how to deal with data might be another reason. The experiment results based on the mean values of 3000 accept simples, but simulation results are averaged for the last 5 seconds which make the curve become more smooth.

In case 1 and case 2 there is little difference between two models: with or without Magnus effect. Because drag force is the primary factor influencing particle movement. Fig.6.8 shows the results for Re_r=100. In high Re_r case, little difference between the model with Magnus lift force and without Magnus lift force can be observed.

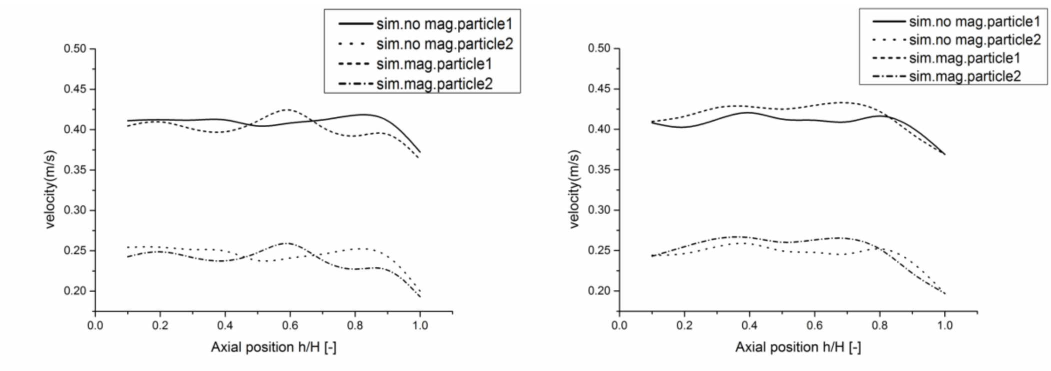

(a) (b)

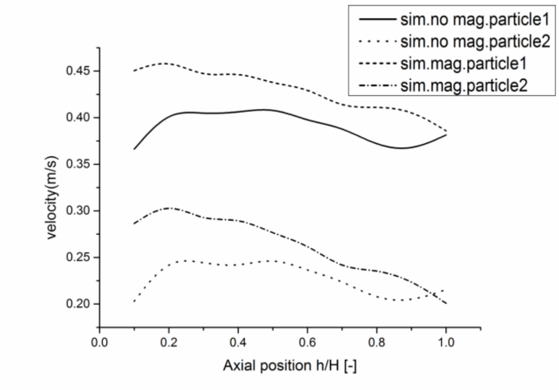

(c)

Figure 6.9 Axial centerline profiles of Z-direction velocity: (a) case 1, (b) case 2, (c) case 3.

Fig.6.9 show the axial centerline profiles of particle vertical velocity. For lower rotational Reynolds number (1 and 10), the Magnus force has a minor effect. However, for higher rotational Reynolds number (100), similar to radial profile, the Magnus lift force has a pronounced effect on particle velocity, which can even influence the translational motion of particles.

In a large quantity of previous research, Empirical formula is used to revise drag model if the simulation is not in good agreement with experiment and Magnus effect is neglect. However, drag force may not be the only element which can impact particle movement according to section 6.3.1. Magnus lift force equally plays a pivotal role in fluidization while Re_r is high for a few particles in extreme cases. So the introduction of Magnus effect in DEM may be another way to fix discrete element method(DEM), especially for the high rotational Reynolds number case.

6.3.5 Particle velocity fluctuation

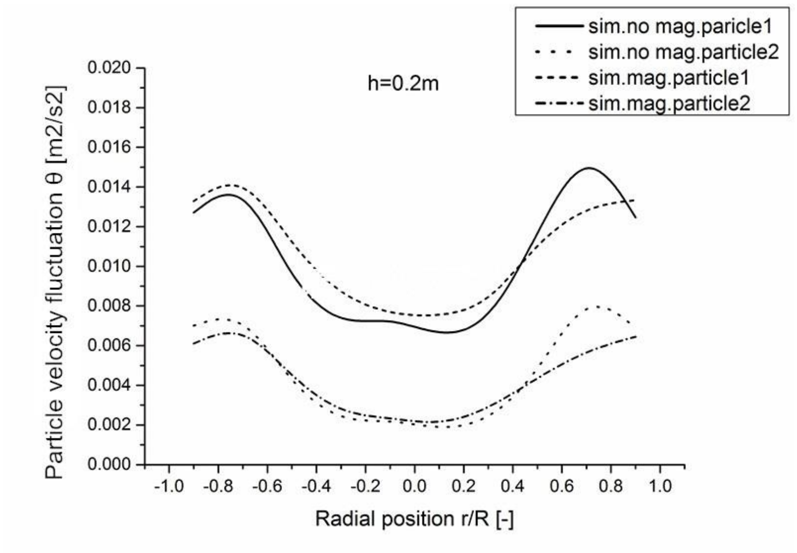

Figure 6.10 Radial profiles of particle velocity fluctuation at different height in case 1

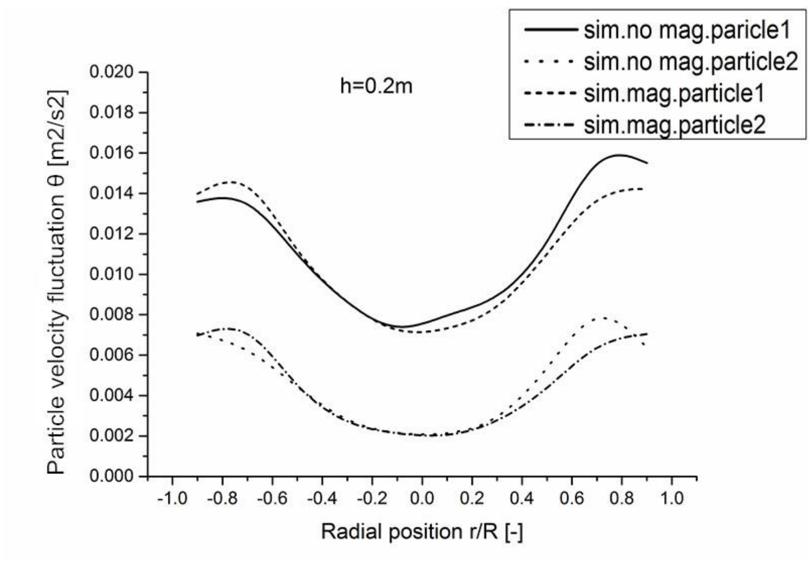

Figure 6.11 Radial profiles of particle velocity fluctuation at different height in case 2

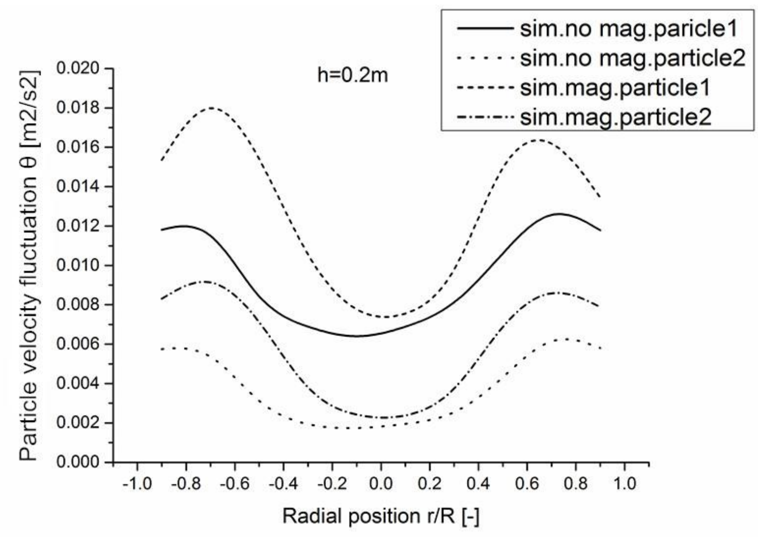

Figure 6.12 Radial profiles of particle velocity fluctuation at different height in case 3

Figs.6.10 to 6.12 show the particle velocity fluctuation. The fluctuation of particle velocity in Z direction is calculated:

$$\theta = \theta_z = \frac{1}{n}\sum_{k=1}^{n}(\upsilon_{z,k}^2 - \overline{\upsilon_z}^2) \tag{6.15}$$

Here n is the number of particles, $\bar{\upsilon}_z$ is the average velocity in Z direction:

$$\overline{\upsilon_z} = \frac{1}{n}\sum_{k=1}^{n}\upsilon_{z,k} \tag{6.16}$$

All the curves in Figs. 6.10 to 12 show the same trend that particles fluctuate strongly near the wall and more placid in the center of riser. This may result from the effect of wall surface. According to Figs. 6.10 and 6.11 in low Re_r case, Magnus lift force is no significant effect on particles because of limited difference between two curves. Fig. 12 depicts the particle velocity for higher Re_r (~100). Compared to that for lower Re_r (1 and 10), the influence of Magnus lift force increased observably. This suggests that Magnus lift force could prompt the particle velocity fluctuation at Z-direction while Re_r is high and this mainly happened in the low part of riser.

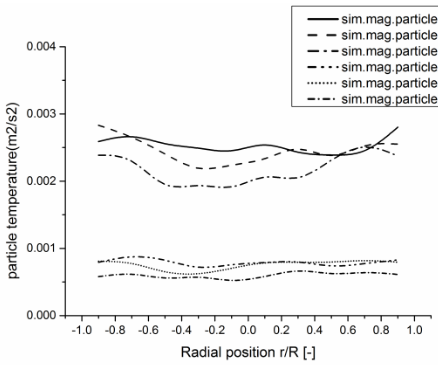

(a)

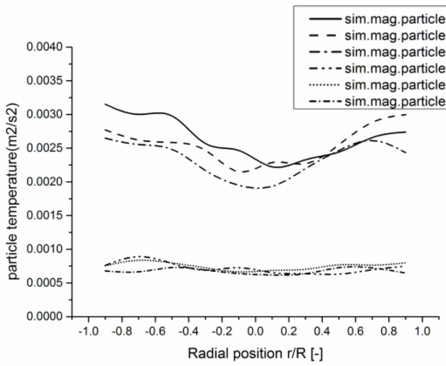

(b)

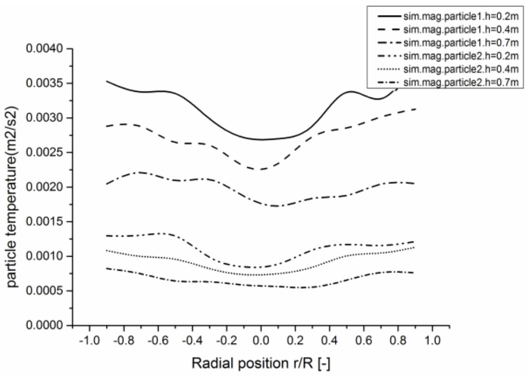

(c)

Figure 6.13 Radial profiles of X-direction granular temperature : (a) case 1, (b) case 2, (c) case 3.

Similar to particle velocity fluctuation at Z-direction, particle velocity fluctuation at X-direction is discussed for analyzing Radial movement. Fig.6.13 show the particle velocity fluctuation at X-direction for different bed height. The influence of wall surface may be indistinctive in X-direction, and therefore the curves are smoother than that in Figs.6.10 to 12. The particle velocity fluctuation at X-direction increases with increasing Re_r, indicating that the Magnus lift force may promote particle velocity fluctuation at X-direction only in some specific situations. The reason may be that Magnus lift force caused by particle rotation, in high Re_r case, particle rotation result in increasing instability of gas-solid system. Therefore, particle velocity fluctuation was also influenced by particle rotation. The result from this section also demonstrates that Magnus lift force may promote the radial movement of particles comparing with axial direction. Therefore, not only at Z-direction, Magnus lift force also prompts the particle velocity fluctuation at X and Y-direction.

6.4 Conclusions

A modified DEM code incorporated with Magnus force was used to simulation particle motion in circulating fluidized bed (CFB) risers. The results with or without Magnus lift force were compared for different Re_r numbers. The radial and axial profiles of X-direction velocity, granular temperature and radial profiles of X-direction velocity were discussed in details. Our simulations show:

1. Particles move upward with a higher speed near the central of the riser and downward with a lower speed near the walls, and the typical core-annular flow structure can be demonstrated.

2. The influence of Magnus lift force is enhanced with a higher Re_r (especially for $Re_r \sim 10^2$), and might be in the same magnitude as the drag force.

3. Magnus lift force affects the movement of particles in both radial and axial directions while Re_r is high. In low Re_r case it can be neglected in computational simulation model.

The introduction of Magnus force can improve the discrete particle model and capture the radial movement of particles in high Re_r case when used in the dilute phase region. On the other hand, in real gas-solid two phase system, high particle rotational speed might cause more prominent Magnus effect and impact particle movement. The influence of Magnus lift force still needs to be considered and evaluated in the fluidized bed when the particle rotational speed is high.

CHAPTER 7 CONCLUSIONS AND RECOMMENDATIONS FOR FUTURE WORK

7.1 Conclusions of research

This thesis systemactically investigated the flow dynamics and particle mixing in gas-solid two phase fluidized bed, including three scales: the microscopic particle scale, the mesoscopic structure scale, and the macroscopic reactor scale.

For microscopic scale, particle rotation and Magnus effect was discussed in Chapter 6. In this Chapter, a pseudo two-dimensional discrete element model (DEM) was used to investigate the influence of Magnus lift force in fluidized bed. The rotational Reynolds number (Re_r) bases on the angular velocity and the diameter of the spheres is used to characterize the rotational movement of particles. We studied the influence of Magnus lift force for particles with rotational Reynolds number in the range of 1~100. Our results show that the influence of Magnus lift force is enhanced with a higher Rer. Magnus lift force affects the movement of particles in both radial and axial directions while Rer is high. However, in low Rer case it can be neglected in computational simulation model. This indicates the introduction of Magnus lift force may improve the discrete particle model only in high Rer case and Magnus effect should be considered in real gas-solid two phase system when the particle rotational speed is high.

For mesoscopic structure scale, particle image velocimetry (PIV) is employed in this work to measure particle flow field in a two-dimensional fluidized bed to obtain particle velocity distribution function around a single bubble. Discrete element method (DEM) is also used to investigate particle velocity distribution at the individual particle scale. The results show that the speed distribution of particles with heterogeneous structures is a linear superposition of multiple Maxwellian distributions. A tri-peak model based on the fluid and particle control mechanism is theoretically derived. Three kinds of models: a tri-peak model, a bi-peak model and a single-peak model are proposed to fit the experimental data. The error analysis shows that compared with other models the tri-peak model can profile particle speed distribution more accurately.

For macroscopic scale, on one hand, discrete particle model is used to simulate fluidized beds with different jet numbers, and the results are validated by physical experiments. Cases with different jet numbers (varying from one to five) but the same gas flow rates are compared in terms of the maximum bed pressure drop, bed height, mixing index, particle velocities and contact number. The results show that different jet numbers result in different flow patterns, which severely affect the mixing efficiency. The mixing efficiency in the one-jet case (spouted-bed) is 1.5~3 times higher than other cases due to a higher jet velocity and umbrella-type flow pattern. For the multiple jets, bubbles and vortex can form and promote particle mixing but not as efficient as the case of one jet. However, particle contacts in multiple jet cases are more uniform than the one-jet case. This implies that from the perspective of particle heat transfer, multiple jets can behave better than one jet.

On the other hand, a novel fluorescent tracer technique combining image processing method has been used to investigate the mixing and segregation behavior in a binary fluidized bed with wide size distributions. The particle number percentage in each layer for different gas velocities is obtained by an image processing method. The results show that the theoretical minimal fluidization velocity calculated from the bed pressure drop cannot represent the whole fluidization for a wide size distribution binary particle system. The effect of a wide size distribution is an inflection point in the mixing index curve. There is also a dead region in the bottom of the bed that consists of particles with large size and a low degree of sphericity. The particles in the dead region are extraordinarily difficult to fluidize and should be considered in the design of fluidized beds in industrial applications.

7.2 Recommendations for future work

7.2.1 Different forces for microscopic scale

For microscopic scale, not only Magnus lift force, the particles are subjected to a drag force, buoyancy force, gravity, contact forces (collisions and friction) between particles and between the particles and the walls, and pressure gradient forces. In some special circumstances additional force terms also apply. For example, the Basset force is caused by a deviation from the steady-state motion in a viscous fluid, the Saffman lift force is generated in a flow field with a velocity gradient, an in-depth study of the forces on particles and the conditions for force generation is of great significance for investigating particle motion, developing numerical simulation methods, and optimizing the reactor’s structural parameters. Therefore, the study of different forces for microscopic scale research still needs to be discussed further.

7.2.2 Particle cluster for mesoscopic structure scale

Mesoscopic structures include not only single bubble, but also particle cluster in same kinds of gas-solid systems such as circulating fluidized bed (CFB) riser. The analysis of cluster is more complicated than single bubble because cluster is amorphous. The study of particle cluster in gas-solid systems still need to be discussed further.

7.2.3 How to improve particle mixing for macroscopic scale

Mixing and segregation behaviour in a binary fluidized bed for particles with wide size distributions is discussed in this study. Results show that for a wide size distribution particle binary system, there is a dead region in the bottom layer. The impact of the dead region depends on the gas velocity and volume ratio for a binary system. It is extraordinarily difficult to fluidize for the particles in the dead region. Therefore, how to improve fluidization and particle mixing for macroscopic scale fluidized bed designing still need to be discussed further.

References

Ali, S. S., Al-Ghurabi, E. H., Ibrahim, A. A., and Asif, M. 2018. 'Effect of adding geldart group a particles on the collapse of fluidized bed of hydrophilic nanoparticles', *Powder Technology*, 330: 50-57.

Altzibar, H., Lopez, G., Bilbao, J., and Olazar, M. 2013a. 'Minimum spouting velocity of conical spouted beds equipped with draft tubes of different configuration', *Industrial & engineering chemistry research*, 52: 2995-3006.

Altzibar, H., Lopez, G., Bilbao, J., and Olazar, M. 2013b. 'Operating and peak pressure drops in conical spouted beds equipped with draft tubes of different configuration', *Industrial & engineering chemistry research*, 53: 415-427.

Ambler, P. A., Milne, B. J., Berruti, F., and Scott, D. S. 1990. 'Residence time distribution of solids in a circulating fluidized bed: experimental and modelling studies', *Chemical Engineering Science*, 45: 2179-2186.

Amiri, Z., Salman, M., and Mansour, S. 2016. 'Particles mixing induced by bubbles in a gas‐solid fluidized bed', *AIChE Journal*, 62: 1430-1438.

Avidan, A., and Joseph, Y. 1985. 'Solids mixing in an expanded top fluid bed', *AIChE Journal*, 31: 835-841.

Babu, M. P., Sai, P. S. T., and Krishnaiah, K. 2017. 'Continuous segregation of binary heterogeneous solids in a fast-fluidized bed', *Particuology*, 35: 101-107.

Barkla, H. M., and Auchterlonie, L. J. 1971. 'The Magnus or Robins effect on Rotating Spheres', *Journal of Fluid Mechanics*, 47: 437-447.

Boemer, A., Qi, H., and Renz, U. 1997. 'Eulerian simulation of bubble formation at a jet in a two-dimensional fluidized bed', *International Journal of Multiphase Flow*, 23: 927-944.

Bokkers, G. A., Annaland, M. V. S., and Kuipers, J. A. M. 2004. 'Mixing and segregation in a bidisperse gas–solid fluidised bed: a numerical and experimental study', *Powder Technology*, 140: 176-186.

Boyer, C., Anne Marie Duquenne, and Gabriel Wild. 2003. 'Measuring techniques in gas–liquid and gas–liquid–solid reactors', *Chemical Engineering Science*, 34: 3185-3215.

Brachi, P., Riccardo Chirone, Francesco Miccio, Michele Miccio, and Giovanna Ruoppolo. 2017. 'Segregation and Fluidization Behavior of Poly-disperse Mixtures of Biomass and Inert Particles', *Chemical Engineering Transactions*, 57: 811-816.

Brilliantov, N. V., and Thorsten Pöschel. 2000. 'Deviation from Maxwell distribution in granular gases with constant restitution coefficient', *Physical Review E*, 61: 2809.

Carlos, C. R., and J. F. Richardson. 1967. 'Particle speed distribution in a fluidised system', *Chemical Engineering Science*, 22: 705.

Carlos, C. R., and J. F. Richardson. 1968. 'Solids movement in liquid fluidised beds—I Particle velocity distribution', *Chemical Engineering Science*, 23: 813-824.

Changfu, Y., Qi H., and Xu, X. 2003. 'Lift force on rotating sphere at low Reynolds numbers and high rotational speeds', *Acta Mechanica Sinica*, 19: 300-307.

Cheikh, K. E., Chafika Djelal, Yannick Vanhove, Patrick Pizette, and Sébastien Remond. 2017. 'Experimental and numerical study of granular medium-rough wall interface friction', *Advanced Powder Technology*, 29: 130-141.

Chen, JL-P. 1981. 'A theoretical model for particle segregation in a fluidized bed due to size difference', *Chemical Engineering Communications*, 9: 303-320.

Chen, J., Yin, W., Wang, S., Yu, G., Li, J., Hu, T., and Lin, F. 2017. 'Modelling of coal/biomass co-gasification in internal circulating fluidized bed using kinetic theory of granular mixture', *Energy Conversion & Management*, 148: 506-516.

Chen, L. P., and Keairns, D. L. 1975. 'Particle segregation in a fluidized bed', *Canadian Journal of Chemical Engineering*, 53: 395-402.

Cheung, L., Nienow, A. W., and Rowe, P. N. 1974. 'Minimum fluidisation velocity of a binary mixture of different sized particles', *Chemical Engineering Science*, 29: 1301-1303.

Chew, J. W., Jeffrey, R. W., and Christine, M. H. 2010. 'Axial segregation in bubbling gas‐fluidized beds with Gaussian and lognormal distributions of Geldart Group B particles', *AIChE Journal*, 56: 3049-3061.

Chiba, S., Chiba, T., Nienow, A. W., and Kobayashi, H. 1979. 'The Minimum Fluidization Velocity, Bed Expansion and Pressure-Drop Profile of Binary Particle Mixture', *Powder Technology*, 22: 255-269.

Clarke, D. A., Sederman, A. J., Gladden, L. F., and Holland, D. J. 2018. 'Investigation of void fraction schemes for use with cfd-dem simulations of fluidized beds', *Industrial & Engineering Chemistry Research*, 57(8): 3002-3013.

Collins, R. 1982. 'Cloud patterns around a bubble growing in a gas-fluidized bed', *Journal of Fluid Mechanics*, 122: 155-167.

Cundall, P. A., and Strack, O. D. L. 1979. 'A discrete numerical model for granular assemblies', *Géotechnique*, 29: 47-65.

Dahl, S. R., and Hrenya, C. M. 2005. 'Size segregation in gas–solid fluidized beds with continuous size distributions', *Chemical Engineering Science*, 60: 6658-6673.

Dandy, D. S., and Harry, A. D. 1990. 'A sphere in shear flow at finite Reynolds number: effect of shear on particle lift, drag, and heat transfer', *Journal of Fluid Mechanics*, 216: 381-410.

Davidson, J. F., and Harrison, D. 1963. 'Fluidized Particles', *Cambridge University Press*.

Deb, S., and Danesh, K. T. 2014. 'Two and three dimensional modeling of fluidized bed with multiple jets in a DEM–CFD framework', *Particuology*, 16: 19-28.

Dijkhuizen, W., Bokkers, G. A., Deen, N. G., Annaland, M. V. S., and Kuipers, J. A. M. 2010. 'Extension of PIV for measuring granular temperature field in dense fluidized beds', *AIChE Journal*, 53: 108-118.

Dritselis, C. D. 2017. 'On the enhancement of particle deposition in turbulent channel airflow by a ribbed wall', *Advanced Powder Technology*, 28.

Duursma, G. R, D. H Glass, S. J. L Rix, and M. I Yorquez-Ramirez. 2001. 'PIV investigations of flow structures in the fluidised bed freeboard region', *Powder Technology*, 120: 2-11.

Eames, I., and Gilbertson, M. A. 2005. 'Mixing and drift in gas-fluidised beds', *Powder technology*, 154: 185-193.

El-Sayed, S., and Mostafa, M. E. 2019. 'Combustion and emission characteristics of egyptian sugarcane bagasse and cotton stalks powders in a bubbling fluidized bed combustor', *Waste and Biomass Valorization,* 10: 2015-2035.

Ergun, S., and Orning, A. A. 1949. 'Fluid flow through randomly packed columns and fluidized beds', *Industrial and Engineering Chemistry*, 41: 1179-1184.

Estejab, B., Guevara, C. N., Foster, A., and Francine, B. 2017. 'Coal-biomass mixing characteristics in a bubbling fluidized bed of Geldart A particles', *Chemical Engineering Research & Design*, 120: 1-14.

Fan, L. T., and Chang, Y. 1979. 'Mixing of large particles in two‐dimensional gas fluidized beds', *Canadian Journal of Chemical Engineering*, 57: 88-97.

Fan, L. T., Chen, S. J., and Watson, C. A. 1970. 'Solids mixing: annual review', *Industrial & Engineering Chemistry*, 62.

Fei, W., Jin, Y., Yu, Z., Can, J., and Wang, Z. 1994. 'Application Of Phosphor Tracer Technique To The Measurement Of Solids Rtd In Circulating Fluidized Bed', *CIESC Journal*, 45: 230-235.

Ferziger, J. H., and Milovan Perić. 1996. 'Computational Methods for Fluid Dynamics', *Physics Today*, 50: 80-84.

Formisani, B., G De Cristofaro, and R Girimonte. 2001. 'A fundamental approach to the phenomenology of fluidization of size segregating binary mixtures of solids', *Chemical Engineering Science*, 56: 109-119.

Fotovat, F., Renaud, A., Mehrdji, H., Olivier, S., and Jamal, C. 2015. 'Sand-assisted Fluidization of Large Cylindrical and Spherical Biomass Particles: Experiments and Simulation', *Chemical Engineering Science*, 126: 543-559.

Garoosi, F., Safaei, M. R., Dahari, M., and Hooman, K. 2015. 'Eulerian–Lagrangian analysis of solid particle distribution in an internally heated and cooled air-filled cavity', *Applied Mathematics & Computation*, 250: 28-46.

Geldart, D., and Baeyens, J. 1985. 'The design of distributors for gas-fluidized beds', *Powder technology*, 42: 67-78.

Geldart, D., Baeyens J., Pope, D. J., and P. Van De Wijer. 1981. 'Segregation in beds of large particles at high velocities', *Powder Technology*, 30: 195-205.

Gibilaro, L. G., and Rowe, P. N. 1974. 'A Model for Segregating Gas Fluidized Bed', *Chemical Engineering Science*, 29: 1403-12.

Gidaspow, D. 1994. 'Multiphase Flow and Fluidization', *Multiphase Flow & Fluidization*: 1–29.

Gidaspow, D., and Marcelo, S. B. 2018. 'Kinetic theory based multiphase flow with experimental verification', *Reviews in Chemical Engineering*, 34: 299-318.

Goldschmidt, M. J. V., Beetstra, R., and Kuipers, J. A. M. 2002. 'Hydrodynamic modelling of dense gas-fluidised beds: Comparison of the kinetic theory of granular flow with 3D hard-sphere discrete particle simulations', *Chemical Engineering Science*, 57: 2059-2075.

Goldschmidt, M. J. V., Beetstra, R. and Kuipers, J. A. M. 2004. 'Hydrodynamic modelling of dense gas-fluidised beds: comparison and validation of 3D discrete particle and continuum models', *Powder Technology*, 142: 23–47.

Halidan, M., Ganga, R. C., Kejun D., and Yu, A. 2016. 'The effect of interparticle cohesion on powder mixing in a ribbon mixer', *AIChE journal*, 62: 1023-37.

Harrison, D., and Davidson, J. F. 1963. *Fluidised Particles*.

Helmrich, H. K. S., and Janssen, K. 1986. 'Decomposition of NaHCO3 in laboratory and bench scale circulating fluidized bed reactors', *Circulating fluidized bed technology*, 1: 161-166.

Heping, C., Mostoufi N., and Chaouki J. 2001. 'Gas and solids between dynamic bubble and emulsion in gas-fluidized beds', *Powder Technology*, 120: 12-20.

Hoffmann, A. C., Janssen, L. P. B. M., and Prins, J. 1993. 'Particle Segregation in Fluidized Binary-Mixture', *Chemical Engineering Science*, 48: 1583-1592.

Hoffmann, A. C., and Romp, E. J. 1991. 'Segregation in a fluidised powder of a continuous size distribution', *Powder Technology*, 66: 119-126.

Hong, R. Y., Guo, Q. J., Luo, G. H., Zhang, J. Y., and Ding, J. 2003. 'On the jet penetration height in fluidized beds with two vertical jets', *Powder technology*, 133: 216-227.

Hoomans, Bob Petrus Bernardus. 2000. 'Granular dynamics of gas-solid two-phase flows', *Universiteit Twente*.

Hoomans, B. P. B., Kuipers, J. A. M., Briels, W. J., and Swaaij, W. P. M. 1996. 'Discrete particle simulation of bubble and slug formation in a two-dimensional gas-fluidised bed: a hard-sphere approach', *Chemical Engineering Science*, 51: 99-118.

Hu, D., Han, G., Lungu, M., Huang, Z., Liao, Z., Wang, J., and Yang, Y. 2017. 'Experimental investigation of bubble and particle motion behaviors in a gas-solid fluidized bed with side wall liquid spray', *Advanced Powder Technology*, 28: 2306-2316.

Huang, J., and Lu, Y. 2018. 'Characteristics of bubble, cloud and wake in jetting fluidised bed determined using a capacitance probe', *Chemical Engineering Research Design*, 136: 687-697.

Huang, Z., Huang, Z., Odeleye, A., Ye, H., Cui, Z., and Yang, A. 2018. 'Fluid dynamic characterization of a fluidized-bed perfusion bioreactor with cfd-dem simulation', *Journal of Chemical Technology & Biotechnology*, 93: 2316-2330.

Huang, N., and Zheng, X. 2001. 'Magnus Effect in Wind-blown Sand Saltation', *Journal of Lanzhou University*.

Ibsen, C.H., Helland, E., Hjertager, B. H., Solberg, T., Tadrist, L., and Occelli, R. 2004. 'Comparison of multifluid and discrete particle modelling in numerical predictions of gas particle flow in circulating fluidised beds', *Powder Technology*, 149: 29-41.

Ishida, M., Shirai, T., and Nishiwaki, A. 1980. 'Measurement of the velocity and direction of flow of solid particles in a fluidized bed', *Powder Technology*, 27: 1-6.

Jiang, M., Zhao, Y., Liu, G., and Zheng, J. 2011. 'Enhancing mixing of particles by baffles in a rotating drum mixer', *Particuology*, 9: 270-278.

Jin, B., Zhang Y., Zhong, W., and Xiao R. 2009. 'Experimental Study of the Effect of Particle Density on Mixing Behavior in a Spout-Fluid Bed', *Ind.eng.chem.res*, 48: 10055-10064.

Kajishima, Takeo. 2004. 'Influence of particle rotation on the interaction between particle clusters and particle-induced turbulence', *International Journal of Heat & Fluid Flow*, 25: 721-728.

Ke, Q., Henrik T., and Leckner Bo. 2017. 'Mass transfer under segregation conditions in fluidized beds', *Fuel*, 195: 105-112.

Kong, W., Wang, B., Baeyens, J., Li, S., and Zhang, H. 2018. 'Solids mixing in a shallow cross-flow bubbling fluidized bed', *Chemical Engineering Science*, 187: 213-222.

Kojima, T., Ken-ichi I., and Yang G. 1989. 'Measurement of solids behaviour in a fast fluidized bed', *Journal of Chemical Engineering of Japan*, 22: 341-346.

Kuipers, J. A. M., Van Duin K. J., Van Beckum, F. P. H., and Van Swaaij, W. P. M. 1992. 'A numerical model of gas-fluidized beds', *Chemical Engineering Science*, 47: 1913-1924.

Kumaran, V. 2009. 'Dynamics of dense sheared granular flows. Part II. The relative velocity distributions', *Journal of Fluid Mechanics*, 632: 145-98.

Kunii, D., and Octave L. 1991. *Fluidization engineering* (Elsevier).

Kwauk, M., and Li, H. Z. 2007. "Handbook of fluidization." In.: Beijing: Chemical Industry Press.

Lacey, P. M. C. 2010. 'Developments in the theory of particle mixing', *Journal of Chemical Technology & Biotechnology*, 4: 257-68.

Le Lee, Jian, and Eldin Wee Chuan Lim. 2017. 'Comparisons of Eulerian-Eulerian and CFD-DEM simulations of mixing behaviors in bubbling fluidized beds', *Powder technology*, 318: 193-205.

Leszczynski, J. S., Zbigniew, B., and Wladyslaw G. 2002. 'Evaluation of structure and particle velocity distribution in circulating fluidised beds', *Powder Technology*, 128: 22-35.

Li, J., Ge, W., Zhang, J., and Kwauk, M. 2005. 'Multi-Scale Compromise and Multi-Level Correlation in Complex Systems', *Chemical Engineering Research & Design*, 83: 574-582.

Li, J., and Kwauk, M. 2003. 'Particle-fluid two-phase flow', *China Particuology*, 1: 42.

Link, J., Christiaan, Z., Niels, D., and Kuipers, H. 2010. 'Validation of a Discrete Particle Model in a 2D Spout-Fluid Bed Using Non-Intrusive Optical Measuring Techniques', *Canadian Journal of Chemical Engineering*, 82: 30-36.

Liu, R., Xiao R., Ye, M., and Liu, Z. 2018. 'Analysis of particle rotation in fluidized bed by use of discrete particle model', *Advanced Powder Technology*, 29: 1655-1663.

Liu, X., Wang, L., and Ge, W. 2016. 'Meso-scale statistical properties of gas-solid flow a direct numerical simulation (DNS) study', *AIChE Journal*, 63: 3-14.

Lu, H., Wang, S., Zhao, Y, Yang, L., Gidaspow, D., and Ding, J. 2005. 'Prediction of particle motion in a two-dimensional bubbling fluidized bed using discrete hard-sphere model', *Chemical Engineering Science*, 60: 3217-3231.

Lukerchenko, N. 2001. "Collision with bed and magnus effect in numerical simulation of solid particle saltation over rough bed." In *International conference on computational mechanics and modern applied software systems*. Moskva

Lun, C. K. K., Savage, S. B., Jeffrey, D. J., and Chepurniy, N. 1984. 'Kinetic theories for granular flow: inelastic particles in Couette flow and slightly inelastic particles in a general flowfield', *Journal of Fluid Mechanics*, 140: 223-256.

Marsheck, R. M., and Albert, G. 1965. 'Particle flow patterns in a fluidized bed', *AIChE Journal*, 11: 167-173.

Marzocchella, A., P. Salatino, V. Di Pastena, and L. Lirer. 2000. 'Transient fluidization and segregation of binary mixtures of particles', *AIChE Journal*, 46: 2175-2182.

Masson, H. 1978. 'Solid circulation studies in a gas solid fluid bed ag', *Chemical Engineering Science*, 33: 621-623.

Mathiesen, V., T. Solberg, and B.H. Hjertager. 2000. 'An experimental and computational study of multiphase flow behavior in a circulating fluidized bed', *International Journal of Multiphase Flow*, 26: 387-419.

Maurer, S., Gschwend, D., Wagner, E. C., Schildhauer, T. J., J. and Mudde, R. F. 2016. 'Correlating bubble size and velocity distribution in bubbling fluidized bed based on X-ray tomography', *Chemical Engineering Journal*, 298: 17-25.

Medlin, J., and Jackson, R. 1975. 'Fluid Mechanical Description of Fluidized Beds. The Effect of Distributor Thickness on Convective Instabilities', *Industrial & Engineering Chemistry Fundamentals*, 14: 315-321.

Mikhailov, M. D., and Freire, A. P. S. 2013. 'The drag coefficient of a sphere: An approximation using Shanks transform', *Powder Technology*, 237: 432-435.

Mingyan, Liu., Yang, Y., Xue J., and Hu Z. 2005. 'Measuring Techniques for Gas Liquid Solid Three-phase Fluidized Bed Reactors', *The Chinese Journal of Process Engineering*, 5: 217-222.

Muller, C. R., Davidson, J. F., Dennis, J. S., and Hayhurst, A. N. 2007. 'A Study of the Motion and Eruption of a Bubble at the Surface of a Two-Dimensional Fluidized Bed Using Particle Image Velocimetry (PIV)', *Industrial & Engineering Chemistry Research*, 46: 1642-1652.

Nguyen, H. V., Whitehead, A. B., and Potter, O. E. 1977. 'Gas backmixing, solids movement, and bubble activities in large scale fluidized beds', *AIChE Journal*, 23: 913-922.

Nienow, A. W., and Naimer, N. S. 1980. 'Continuous Mixing Of Two Particulate Species Of Different Density In A Gas Fluidised Bed', *Tran. IChemE*, 58: 181-186.

Nienow, A. W., Rowe, P. N., and Cheung, Y. L. 1978. 'A quantitative analysis of the mixing of two segregating powders of different density in a gas-fluidised bed', *Powder Technology*, 20: 89-97.

Huang, N., and Zheng, X. 2001. 'Magnus effect in wind-blown sand saltation', *journal-lanzhou university natural sciences* 37: 19-25.

Nosrati, K., Movahedirad, S., Mohammad Amin Sobati, and Ali Akbar Sarbanha. 2017. 'Experimental study on the pressure wave attenuation across gas-solid fluidized bed by single bubble injection', *Powder Technology*, 305: 620-624.

Oki, K., Walawender, W. P., and Fan, L. T. 1977. 'The measurement of local velocity of solid particles', *Powder Technology*, 18: 171-178.

Olaofe, O. O., MA Van der Hoef, and Kuipers, J. A. M. 2011. 'Bubble formation at a single orifice in a 2D gas-fluidized bed', *Chemical engineering science*, 66: 2764-2773.

Oliver, D. R. 1962. 'Influence of Particle Rotation on Radial Migration in the Poiseuille Flow of Suspensions', *Nature*, 194: 1269-71.

Olivieri, G., Marzocchella, A., and Salatino, P. 2004. 'Segregation of fluidized binary mixtures of granular solids', *AIChE Journal*, 50: 3095-3106.

Oseen, Carl Wilhelm. 1911. *Über die stoke'sche formel und über eine verwandte aufgabe in der hydrodynamik* (Almqvist & Wiksell).

Peng, Z., Alghamdi, Y. A., Moghtaderi, B., and Doroodchi, E. 2016. 'CFD-DEM investigation of transition from segregation to mixing of binary solids in gas fluidised beds', *Advanced Powder Technology*, 27: 2342-2353.

Qureshi, A. E., and Creasy, D. E. 1979. 'Fluidised bed gas distributors', *Powder Technology*, 22: 113-119.

Rangarajan, D., Tomo Shiozawa, Shen, Y., Curtis, J. S., and Yu, A. 2013. 'Influence of operating parameters on raceway properties in a model blast furnace using a two-fluid model', *Industrial & engineering chemistry research*, 53: 4983-4990.

Rasul, M. G., Rudolph, V., and Carsky, M. 1999. 'Segregation potential in binary gas fluidized beds', *Powder Technology*, 103: 175-181.

Rhodes, M. J., Wang, X, Nguyen, M., Stewart, P., and Liffman, K. 2001. 'Study of mixing in gas-fluidized beds using a DEM model', *Chemical Engineering Science*, 56: 2859-2866.

Rice, R. W., and Brainovich, J. F. 1986. 'Mixing/segregation in two‐ and three‐dimensional fluidized beds: Binary systems of equidensity spherical particles', *AIChE Journal*, 32: 7-16.

Rong, L., Zhan, J., and Wu, C. 2012. 'Effect of various parameters on bubble formation due to a single jet pulse in two-dimensional coarse-particle fluidized beds', *Advanced Powder Technology*, 23: 398-405.

Rowe, P. N., and Nienow, A. W. 1976. 'Particle mixing and segregation in gas fluidised beds. A review ', *Powder Technology*, 15: 141-147.

Rowe, P. N., Partridge, B. A., and Lyall, E. 1964. 'Cloud formation around bubbles in gas fluidized beds', *Chemical Engineering Science*, 19: 973-985.

Rowe, P. N., Partridge. B. A., Cheney, A. G., Henwood, G. A., and Lyall, E. 1965. 'Mechanisms of solids mixing in fluidised beds', *Transactions of the Institution of Chemical Engineers and the Chemical Engineer*, 43: T271.

Rowe, P. N., Nienow, A. W., and Agbim, A. J. 1972. 'Preliminary quantitative study of particle segregation in gas fluidized-beds-binary-systems of near spherical particles', *Transactions of the institution of chemical engineers and the chemical engineer*, 50: 324.

Safaei, M. R., O Mahian, F. G., Hooman, K, Karimipour, A, Kazi, S. N., and Gharehkhani, S. 2014. 'Investigation of micro- and nanosized particle erosion in a 90° pipe bend using a two-phase discrete phase model', *The Scientific World Journal,2014,(2014-10-14)*, 2014: 740578.

Sanchez-Delgado, S., Marugan-Cruz, C., Serrano, D., and Briongos, J. V. 2019. 'Distributor performance in a bubbling fluidized bed: Effects of multiple gas inlet jet and bubble generation', *Chemical Engineering Science*, 195: 367-380.

Sanchez-Prieto, J., Hernandez-Jimenez, F., Garcia-Gutierrez, L. M., and Soria-Verdugo, A. 2017. 'Experimental study on the characteristic mixing time of solids and its link with the lateral dispersion coefficient in bubbling fluidized beds', *Chemical Engineering Journal*, 307: 113-121.

Sathiyamoorthy, D., and Masayuki, H. 2003. 'On the influence of aspect ratio and distributor in gas fluidized beds', *Chemical Engineering Journal*, 93: 151-161.

Saxena, S. C., Chatterjee, A., and Patel, R. C. 1979. 'Effect of distributors on gas—solid fluidization', *Powder Technology*, 22: 191-198.

Shen, L., and Zhang, M. 1991. 'Effect of particle size on solids mixing in bubbling fluidized beds', *Powder Technology*, 97: 170-177.

Shrestha, S., Kuang, S., Yu, A., and Zhou, Z. 2019. 'Particle Shape Effect on Bubble dynamics in Central Air Jet Pseudo-2D Fluidized Beds: A CFD-DEM Study', *Chemical Engineering Science*, 201: 448-466.

Sun, J., and Battaglia, F. 2006. 'Hydrodynamic modeling of particle rotation for segregation in bubbling gas-fluidized beds', *Chemical Engineering Science*, 61: 1470–1479.

Tanimoto, H., Chiba, T., and Kobayashi, H. 1983. 'effects of segregation on fine elutriation from gas-fluidised beds of binary solid mixture', *Journal of Chemical Engineering of Japan*, 16: 149-152.

Toomey, R. D., and Johnstone, H. F. 1952. 'Gaseous fluidization of solid particles', *Chemical Engineering Progress*, 48: 220-226.

Torobin, L. B., and Gauvin, W. H. 1960. 'Fundamental aspects of solids-gas flow: Part IV: The effects of particle rotation, roughness and shape', *The Canadian Journal of Chemical Engineering*, 38: 142-153.

Tsuji, Y., Kawaguchi, T., and Tanaka, T. 1993. 'Discrete particle simulation of two-dim ensional fluidized bed', *Powder Technology*, 77: 79-87.

Vaccaro, S., Musmarra, D., and Petrecca, M. 1997a. 'Evaluation of the jet penetration depth in gas-fluidized beds by pressure signal analysis', *International Journal of Multiphase Flow*, 23: 683-698.

Vaccaro, S., Musmarra, D., and Petrecca, M. 1997b. 'A technique for measurement of the jet penetration height in fluidized beds by pressure signal analysis', *Powder technology*, 92: 223-231.

Van Zoonen, D. 1962. "Measurements of diffusional phenomena and velocity profiles in a vertical riser." In *Proc. Symp. on The Interaction between Fluids and Particles, 1962*, 64-71.

Walker, B. V. 1975. 'The effect of distributor type on conversion in a bubbling fluidised bed', *Chemical Engineering Journal*, 9: 49-61.

Wang, J., Van der Hoef, M. A., and Kuipers, J. A. M. 2010. 'Coarse grid simulation of bed expansion characteristics of industrial-scale gas–solid bubbling fluidized beds', *Chemical Engineering Science*, 65: 2125-2131.

Wang, J., Zhao, B., and Li, J. 2016. 'Towards a mesoscale-structure-based kinetic theory for heterogeneous gas-solid flow: Particle velocity distribution function', *AIChE Journal*, 62: 2649-2657.

Wang, R., and Chang, C. 2010. 'Particle mixing/segregation in gas - solid fluidized bed of ternary mixtures', *Canadian Journal of Chemical Engineering*, 73: 793-799.

Wang, S., Shao, B., Li, X., Zhao, J., Liu, L., Liu, Y., Liu, Y., and Dong, Q. 2017. 'Simulations of vertical jet penetration using a filtered two-fluid model in a gas–solid fluidized bed', *Particuology*, 31: 95-104.

Wang, S., Shen, Z., Lu, H., Yu, L., Liu, W., and Ding, Y. 2008. 'Numerical predictions of flow behavior and cluster size of particles in riser with particle rotation model and cluster-based approach', *Chemical Engineering Science*, 63: 4116-4125.

Wang, X., Zhong, Z., Wang, H., and Wang, Z. 2015. 'Application of Hilbert-Huang transformation in fluidized bed with two-component (biomass particles and quartz sands) mixing flow', *Korean Journal of Chemical Engineering*, 32: 43-50.

Wen, C. Y., and Yu, Y. H. 1966. 'Mechanics of Fluidization', *Chem.engng Prog.symp.ser*, 62: 100-11.

Westerweel, Jerry. 1997. 'Fundamentals of digital particle image velocimetry', *Measurement science and technology*, 8: 1379.

White, B. R., and Schulz, J. C. 1977. 'Magnus effect in saltation', *Journal of Fluid Mechanics*, 81: 497-512.

Willert, C. E., and Gharib, M. 1991. 'Digital particle image velocimetry', *Experiments in Fluids*, 10: 181-193.

Wirsum, M, F., Iwanowa, N., and Lukjanow, G. 2001. 'Particle mixing in bubbling fluidized beds of binary particle systems', *Powder Technology*, 120: 63-69.

Wormsbecker, M., Adams, A., Pugsley, T., and Winters, C. 2005. 'Segregation by size difference in a conical fluidized bed of pharmaceutical granulate', *Powder Technology*, 153: 72-80.

Wu, S. Y., and Baeyens, J. 1998. 'Segregation by size difference in gas fluidized beds', *Powder Technology*, 98: 139-150.

Wu, X., Wang, Q., Luo, Z., Fang, M., and Cen, K. 2008a. 'Experimental study of particle rotation characteristics with high-speed digital imaging system', *Powder Technology*, 181: 21-30.

Wu, X., Wang, Q., Luo, Z., Fang, M., and Cen, K. 2008b. 'Theoretical and experimental investigations on particle rotation speed in CFB riser', *Chemical Engineering Science*, 63: 3979-3987.

Yang, G. Q., Du, B., and Fan, L. S. 2007. 'Bubble formation and dynamics in gas–liquid–solid fluidization—A review', *Chemical Engineering Science*, 62: 2-27.

Yang, W. 1986. 'Particle segregation in gas-fluidized beds', *Encyclopedia of Fluid Mechanics*, 4: 817-852.

Ye, M., Van Der Hoef, M. A., and Kuipers, J. A. M. 2004. 'A numerical study of fluidization behavior of Geldart A particles using a discrete particle model', *Powder Technology*, 139: 129-139.

Ye, M., Van Der Hoef, M. A., and Kuipers, J. A. M. 2005a. 'The effects of particle and gas properties on the fluidization of Geldart A particles', *Chemical Engineering Science*, 60: 4567-4580.

Ye, M., Van Der Hoef, M. A., and Kuipers, J. A. M. 2005b. 'From Discrete Particle Model to a Continuous Model of Geldart A Particles', *Chemical Engineering Research & Design*, 83: 833-843.

Ye, Mao. 2005. 'Multi-level modeling of dense gas-solid two-phase flows'.

You, C., Qi, H., and Xu, X. 2003. 'Lift force on rotating sphere at low reynolds numbers and high rotational speeds', *Acta Mechanica Sinica*, 19: 300-307.

You, Y., and Zhao, Y. 2018. 'Discrete element modelling of ellipsoidal particles using super-ellipsoids and multi-spheres: a comparative study', *Powder Technology*, 331: 179-191.

Yuan, Z. L., Ma, M., and Xu, Y. Q. 2001. 'Study on effect of particle rotation on fluidizing behavior by discrete numerical simulation method', *Journal of Combustion Science & Technology*, 7: 238-41.

Yuan, Z., Ming, M. A., and Xu, Y. 2001. 'Study on Effect of Particle Rotation on Fluidizing Behavior Using Discrete Numerical Simulation Method', *Journal of Combustion Science & Technology*.

Zhao, Y., Xu, L., and Zheng, J. 2017. 'Cfd-dem simulation of tube erosion in a fluidized bed', *AIChE Journal*, 63: 418-437.

Zhang, K., Zhang, H., Lovick, J., Zhang, J., and Zhang, B. 2002. 'Numerical computation and experimental verification of the jet region in a fluidized bed', *Industrial & engineering chemistry research*, 41: 3696-3704.

Zhang, Y. 2010. 'Experimental Investigation and 3D DEM simulation on Particle Mixing Characteristic in Gas-Solid Fluidized Bed'.

Zhang, Y., Jin, B., and Zhong, W. 2008. 'Experimental Investigations on the Effect of the Tracer Location on Mixing in a Spout-Fluid Bed', *International Journal of Chemical Reactor Engineering*, 6: 77-90.

Zhang, Y., Jin, B., and Zhong, W. 2009a. 'Experiment on particle mixing in flat-bottom spout–fluid bed', *Chemical Engineering & Processing Process Intensification*, 48: 126-134.

Zhang, Y., Jin, B., and Zhong, W. 2009b. 'Experimental investigation on mixing and segregation behavior of biomass particle in fluidized bed', *Chemical Engineering & Processing Process Intensification*, 48: 745-754.

Zhang, Y., Jin, B., Zhong, W., Bing Ren, and Rui Xiao. 2009. 'Characterization of Fluidization and Segregation of Biomass Particles by Combining Image Processing and Pressure Fluctuations Analysis', *International Journal of Chemical Reactor Engineering*, 7: 862-868.

Zhang, Y., Zhong, W., and Jin, B. 2011. 'Experimental and Theoretical Study on Fluidization of Stalk-Shaped Biomass Particle in a Fluidized Bed', *International Journal of Chemical Reactor Engineering*, 9: 1979-1981.

Zhang, Y., Zhong, W., Jin, B., and Xiao, R. 2012. 'Mixing and segregation behavior in a spout-fluid bed: effect of particle size', *Industrial & Engineering Chemistry Research*, 51: 14247-14257.

Zhang, Y., Zhong, W., Jin, B., and Xiao, R. 2013. 'Experimental Investigation on Segregation Characteristic of Non-Spherical Particles in Fluidized Bed Based on Virtual Particle Concentration', *Journal of Engineering Thermophysics*, 34: 1079-1083.

Zhang, Y., Mao, Y., Zhao, Y., Tong, G., Xiao, R., and Liu, Z. 2015. 'Emulsion phase expansion of Geldart a particles in bubbling fluidized bed methanation reactors: A CFD–DEM study', *Powder Technology*, 275: 199-210.

Zhijie, Q., and Kwauk, M. 1985. "Visualization of Particle Movement by Photolumines cence." In *Fluidization '85, Conference Papers, Second China-Japan Symposiu m*, 477.

Zhong, W., Yu, A., Zhou, G., Xie, J., and Zhang, H. 2016. 'CFD simulation of dense particulate reaction system: Approaches, recent advances and applications', *Chemical Engineering Science*, 140: 16-43.

Zhong, W., Zhang, M., Jin, B., Zhang, Y., Xiao, R., and Huang, Y. 2007. 'Experimental investigation of particle mixing behavior in a large spout–fluid bed', *Chemical Engineering Processing-Process Intensification*, 46: 990-995.

Zhou, J., Grace, J. R., Lim, C. J., and Brereton, C. M. H. 1995. 'Particle velocity profiles in a circulating fluidized bed riser of square cross-section', *Chemical Engineering Science*, 50: 237-244.

Zhou, Q., and Fan, L. 2015a. 'Direct numerical simulation of low-Reynolds-number flow past arrays of rotating spheres', *Journal of Fluid Mechanics*, 765: 396-423.

Zhou, Z., Pinson, D., Zou, R. P., and Yu, A. 2011. 'Discrete particle simulation of gas fluidization of ellipsoidal particles', *Chemical Engineering Science*, 66: 6128-6145.

Zhou, Z., Yu, A., and Zulli, P. 2009. 'Particle scale study of heat transfer in packed and bubbling fluidized beds', *AIChE journal*, 55: 868-884.

Zhu, H. P., Zhou, Z., Yang, R., and Yu, A. 2007. 'Discrete particle simulation of particulate systems: theoretical developments', *Chemical Engineering Science*, 62: 3378-3396.